CHARLES UNIVERSITY PRAGUE

faculty of mathematics and physics

High-Frequency Quasi-Periodic Oscillations and their Modulation by Relativistic Effects

Thesis submitted for the degree of Philosophiae Doctor

Michal Bursa

Supervisor: doc. RNDr. Vladimír Karas, DrSc.

Prague, January 2006

If we had the chance to look at the night sky through X-ray-sensitive eyes, from the ground we would not be able to see anything, since the atmosphere absorbs X-rays already at high altitudes. In that way, besides other things, it protects the life that has developed under its coat over the past milliards of years. We would have to fly higher than the birds, up above the clouds and mountains, as high as the orbit - then we could see the sky spangled by X-ray stars. But it would be an altogether different view to the one we are used to. The optically brightest stars would shine only a little and those we normally do not even see would glare as bright lighthouses. We would recognize different constellations and the north would no longer be pointed by the North Star. We would see hundreds of bright sources in the haze of the Milky Way. Most of them would just whisper, but some of them would play a fifth.

Contents

Preface

In many active galactic nuclei as well as in cataclysmic variables and X-ray binaries, there are observed rapid temporal changes of the flux and of individual spectral features. These sources contain a compact object surrounded by an accretion flow in the form of a disc or a torus. The strong gravity near these objects introduces distinctive deviations from Newtonian physics including bending of light rays, gravitational redshift and existence of the inner-most stable circular orbit. All these effects alter profiles of observed light curves and have impact on power spectra, which may be in principle used to test predictions of general relativity.

Low-mass X-ray binaries show variability in X-ray flux on a wide range of time scales. The most prominent phenomenon of the last decade is the discovery of aperiodic changes in flux, known as high-frequency quasi-periodic oscillations (HFQPOs). They are observed both in neutron-star and black-hole sources and feature two related peaks in the power spectrum (therefore they are also known as twin-peak QPOs). These oscillations are extensively studied, because their characteristic periods are close to dynamical time-scales for any motion under the influence of gravity within a few gravitational radii off a compact object.

This thesis concentrates on the phenomenon of high-frequency quasi-periodic oscillations from two perspectives: how are the frequencies of the two HFQPO peaks related to each other and what can be deduced from the correlation; and is it possible to modulate the outgoing radiation by effects of strong gravity only, or do intrinsic local variations of the accreting medium play a major role?

In Chapter 1, the twin-peak quasi-periodic oscillations are first introduced and their properties are summarised separately for neutron-star and black-hole sources, including the new evidence for an inverse-mass scaling of their frequencies. Then the focus is kept on neutron stars, where the observed frequencies vary in time. It is found that the frequencies are approximately linearly correlated and implications of this fact are discussed. Chapter 2 concentrates on the epicyclic resonance model of HFQPOs and compares its predictions for the angular momentum of the Galactic microquasar GRO J1655−40 with a recent estimate made by fitting of the X-ray continuum. It is shown that none of the present resonance models is consistent with the measured value of the spin. Instead, a resonance between the vertical epicyclic and the precession frequency is proposed as an alternative to satisfy the current observational evidence. In Chapter 3, the attention moves to black-hole QPOs. A simple model of a luminous torus filled with an optically thin gas is constructed in order

to explore possible strong gravity effects on a modulation of an emergent flux. Finally in Chapter 4 it is shown, by using a numerical ray-tracing, how basic global oscillation modes of a gaseous torus affect the outgoing radiation received by a distant observer and how the flux modulation depends on the geometry and various other parameters of the torus. The results of the model are then compared with outputs from a three-dimensional magneto-hydrodynamical simulation of an accretion flow.

Results of Chapter 1 are published in Abramowicz, Bulik, Bursa & Kluźniak (2003), Abramowicz *et al.* (2005a,b) and in a paper in preparation (Abramowicz *et al.* 2006). Ideas of Chapter 2 will be published in Bursa (2006). The construction of the oscillating torus model and the three-dimensional ray-tracing code have been described in Bursa (2004). Results of Chapter 5 are presented briefly in Bursa *et al.* (2004) and in an extended version in Bursa (2005).

I am thankful to Marek Abramowicz and Włodek Kluźniak, who suggested the idea of torus oscillations to me; to Jiří Horák, with whom I discussed a lot of details; to Ladislav Šubr, who helped me to improve the text; and my greatest thanks belong to Vladimír Karas, who supervised all my work and who gave me a lot of useful advice and incentive comments. I am also thankful to an innominate reader for his last-minute remarks upon the text layout. During years, my work was supported by the Czech Science Foundation grant 205/03/H144, by grant 299/2004 of the Charles University and by grant IAA 300030510 of the Academy of Sciences.

Chapter 1

High-frequency quasi-periodic oscillations

Instead of expected clearly periodic pulsations similar to those seen in Her X−1 (Alpar *et al.* 1982), a new unique kind of X-ray signal modulation – so called quasi-periodic oscillations, QPOs – was detected in 1980s by the *EXOSAT* satellite during observations of X-ray emissions from several low-mass X-ray binary sources (van der Klis & Jansen 1985; van der Klis *et al.* 1985). Fourier analysis of detected lightcurves revealed broad peaks in the power density spectrum at different frequencies in the $1 - 50$ Hz range (the sensitivity of *EXOSAT* was below 200 Hz).

During the time different types of QPOs were found in many sources in the Galactic bulge. They are characterised by a specific shape and frequency range (see Table 2.2 in van der Klis 2005 for the classification). In some cases we already know what causes their excitation, but others are still puzzling. The most striking, the most interesting and undoubtedly the most mysterious type of QPOs are so-called high-frequency quasi-periodic oscillations (HFQPOs), which appear in the range of frequencies that Keplerian orbits very close to compact stars would have.

In the first three sections of this Chapter we briefly review current observational evidence for the high-frequency quasi-periodic oscillation seen in neutron-star and black-hole sources, including the evidence and theoretical suggestions for an inverse-mass scaling of frequencies of these oscillations. In following sections we focus on neutron-star sources and discover a rather exciting global correlation between the two kHz QPO frequencies; we look at the properties of this correlation in individual objects and make linear fits to the data, which we find to have anti-correlated parameters of the slope and the intercept. The anti-correlation will point out a possible connection of the neutron-star and black-hole HFQPOs. This Chapter is based on work published in Abramowicz, Bulik, Bursa & Kluźniak (2003), Abramowicz *et al.* (2005a) and Abramowicz *et al.* (2005b).

1.1 HFQPOs in neutron-star sources

In 1996, the initial observation by the newly launched *RXTE* mission showed two new simultaneous QPOs at frequencies in the kilohertz range. Sco X−1 and 4U 1728−34 were the first sources to display these oscillations and nowadays, after a decade of observations, we know by up to three tens of neutron star sources with kHz QPOs (see reviews in van der Klis 1997a, van der Klis 2000, Swank 2004 and van der Klis 2005).

The two peaks usually come in a pair, but sometimes one of them may become undetectable, especially at high count rates. The frequencies ν_U observed for the upper peak range from approximately 300 Hz to 1200 Hz, in some sources they can occasionally exceed 1300 Hz. Lower peak frequencies ν_L are observed between 150 and 1000 Hz. In LMXBs, regimes with essentially identical QPO frequency and energy spectrum can exist at very different fluxes or mass accretion rates.

The positions of the peaks are not strictly fixed in time. As the count rate varies, the centroid frequencies change significantly compared to the widths of the peaks. It is common that the difference between the lowest and highest observed frequency is several hundred of Hertz (see *e.g.* van der Klis 2000, Belloni *et al.* 2005 for a list of frequency ranges in individual sources). The correlation between the peak position and the count rate forms a series of parallel tracks (Zhang *et al.* 1998; Méndez *et al.* 1999). On timescales of hours, the QPO frequency is typically well correlated with luminosity, but on longer timescales of days or weeks the correlation is lost and apparently different levels of luminosity can give the same frequency. When the frequency is the same, the rms amplitude is nearly the same too (Méndez *et al.* 2001). This suggests that there is an extra source of X-ray luminosity, which does not participate in the oscillations and is variable on day to week timescales (van der Klis 2001). Because no sudden and discontinuous jump has ever been

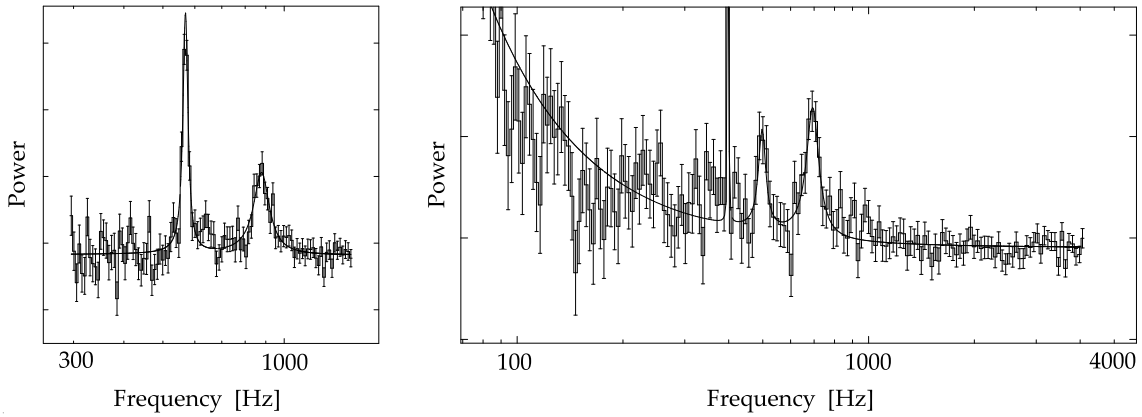

FIGURE 1.1: Twin kHz QPOs in *left*: 4U 1608−52 (Mendez et al. 1998); and *right*: the accreting pulsar SAX J1808.4−3658 (Wijnands et al. 2003) with the 401 Hz pulsar spike. (Adopted from van der Klis 2005.)

observed in the QPO frequency as the count rate decreases, the mechanism is probably such that at some point the kHz QPOs cease, being unobservable for some time, and then become observable again at a some higher frequency (Zhang *et al.* 1998). Variations of the kHz QPO frequencies are observed also on sub-second timescales. In Z sources (see a definition below) occurs a $\sim$6 Hz QPO with amplitude of $1-3\,\%$ rms in the normal branch of the Z track. In Sco X−1 amplitudes and frequencies of the kHz QPO were observed to systematically vary in phase with this 6 Hz oscillation (Yu *et al.* 2001).

The distance between the peaks changes as well. They get closer to each other by several tens of Hertz when they move from low to high frequencies within their range. The separation frequency $\Delta\nu \equiv \nu_U - \nu_L$ is approximately commensurate with the spin frequency $\nu_{\rm spin}$ of the neutron star or half of that. In the eight sources, where both the spin and the separation frequency were measured, $\Delta\nu$ was $0.7-1.3$ times the spin frequency for slow rotators ($\nu_{\rm spin} < 400$ Hz), and $0.36-0.57$ times the spin frequency for fast rotators ($\nu_{\rm spin} > 400$ Hz; van der Klis 2005). The spin frequency of neutron stars can be measured either directly if the source is an X-ray pulsar, or induced from the frequency of burst oscillations (Strohmayer *et al.* 1997), which likely occur very near $\nu_{\rm spin}$, as verified in the case of millisecond pulsars SAX J1808.4−3658 and XTE J1807−294 (in't Zand *et al.* 2001; Linares *et al.* 2005). In these two pulsars, where pulsations, burst oscillations and kHz QPOs are observed simultaneously, the ratios are 0.49 (SAX J1808; $\nu_{\rm spin} = 401$ Hz) and 0.99 (XTE J1807; $\nu_{\rm spin} = 191$ Hz).

The measurements of delays between photons of different energy bands brought initially surprising results. In the case of the black hole Cyg X−1, hard photons are delayed behind soft photons, which has been understood in terms of a coronal model, where low energy photons from the disc are Compton-scattered in the hot corona (Crary *et al.* 1998; Nowak *et al.* 1999). However, the sign of time lags for the QPOs in several sources is the opposite (Vaughan *et al.* 1997; Lee *et al.* 2001), *i.e.* the hard photons arrive ahead of the soft ones. The delay corresponds to the distance of $\sim$20 km, which is consistent with emission from the neutron star surface and from the inner edge of the disc. Indeed, Gilfanov *et al.* (2003) has shown that the millisecond X-ray flux modulations originate on the surface of the neutron star, although they may still be driven by the the disc or by the disc–star interaction.

Low-mass X-ray binaries containing weakly magnetised neutron stars may be divided into two classes, Z and atoll sources, based upon correlations between their spectral colours and Fourier timing properties at X-ray wavelengths (Hasinger & van der Klis 1989). Plots of a 'hard' colour against a 'soft' colour from Z sources usually form a Z shape track that is traced on time scales of hours to days. Plots from atoll sources often resemble a band of points at constant hard colour, and 'islands' appearing on time scales of weeks and months. Power spectra from both types of sources may be described with similar broad-band noise components, but Z sources exhibit strong (up to 10% rms) low-frequency QPOs in the range $1-60$ Hz, while atoll sources do not. The exact cause of the spectral and timing variability is still unknown, but it is thought that the differences between the two classes result from a higher rate of mass transfer in Z sources than atoll sources (but see Muno *et al.* 2002 for a possible unification scheme).

1.2 HFQPOs in black-hole sources

QPOs are also observed in black-hole sources. There are at present seven known Galactic black hole candidates that exhibit HFQPOs in the hectohertz range ($40 - 450$ Hz), and for four of them there is an evidence that the HFQPO peaks occur in pairs with central frequencies in the $3 : 2$ ratio (see a comprehensive review by McClintock & Remillard 2005).

HFQPOs in black-hole sources are much more transient and weaker phenomenon than the kHz QPOs in neutron stars. They occur occasionally, during outbursts and only when the source is in the steep power law (SPL) or in a hard–SPL intermediate spectral state. They have never been seen in the pure hard or in the thermal dominant state[1] (see *e.g.* Remillard 2005 for definitions of black-hole spectral states). In the SPL state, the energy spectrum is characterised by the presence of some black-body component and a very steep, dominant power-law component with index $\Gamma > 2.4$ and no apparent cut-off in energies (Grove *et al.* 1998). The state is thought to be associated with a compact non-thermal corona with some presence of the disc.

Oscillations are much more subtle than the ones observed from neutron stars. Their rms amplitudes are typically only $\sim 1\%$ ($0.5\,\% < \mathrm{rms} < 5\,\%$) of the mean count rate, which pushes the detections to the instrumentational limits. Sometimes several observations with similar spectral and timing characteristics have to be grouped together in order to get a statistically significant evidence.

[1] That does not necessarily mean that in the hard or thermal state HFQPOs are not produced. They may be too faint to be detected.

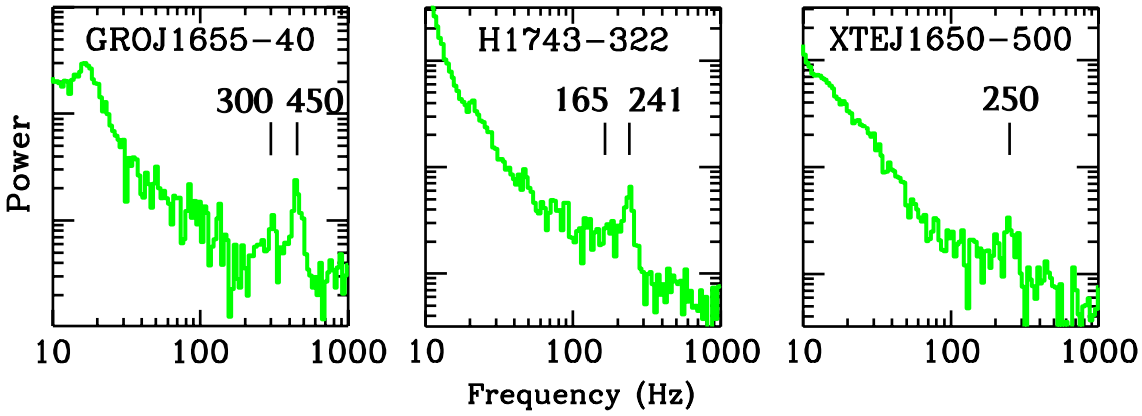

FIGURE 1.2: Examples of high-frequency QPOs (40-450 Hz) seen in black-hole binary systems. Sometimes both oscillations of the $3 : 2$ pair are detected, but more often only one peak can be seen. (Adopted from Remillard 2005.)

Microquasar	ν_U [Hz]	ν_L [Hz]	discrepancy	mass [$M_\odot$]
XTE 1550−564	276 ± 3	184 ± 5	0.0 %	8.4−10.8
GRO 1655−40	450 ± 3	300 ± 5	0.0 %	6.0−6.6
GRS 1915+105	168 ± 3	113 ± 5	0.9 %	10.0−18.0
H 1743−322	240 ± 3	160 ± 8	0.0 %	—

TABLE 1.1: The list of all microquasars, where twin HFQPOs have so far been detected. Mass estimates from optical measurements are listed as well. The discrepancy indicates how much the ratio of the two frequencies differs from the exact value of 1.5.

Frequencies of the two peaks are quite stable, reproducible and form the 3 : 2 ratio with accuracy better than 1 % (Table 1.1). There are two observations, with a faint detections however, which violate the exact ratio by ∼15 %. It is plausible that the peaks change their positions similarly to the kHz neutron-star QPOs, but the variations are very little and so far have been reported from one source only (Miller *et al.* 2001), where the ν_L frequency varied by ∼5 % clearly correlated with the total count rate.

Both peaks can sometimes be detectable at the same time, but more often only one can be seen. The selection depends on the ratio of the thermal disc flux to the power-law flux. When it is high, a very coherent ν_U oscillation appears, while a broader ν_L oscillation can be seen if disc does not contribute significantly. The rms amplitudes of oscillations are anti-correlated with the disc to total X-ray flux ratio. There is a clear trend, in which the lower ν_L oscillation is seen when the source has high overall X-ray luminosity, while the higher ν_U oscillation is seen at lower luminosities. Likewise the ν_L peak is broader and is seen mainly in the low energy band ($6 - 30$ keV), while the ν_U peak is narrower and likes high energies ($10 - 30$ keV and probably even higher, but the range is limited by low count rates).

1.3 Inverse mass scaling

The HFQPO frequencies in black hole candidates appear to be uniquely prescribed by nature for each individual source. They always stay fixed and in the 3 : 2 ratio, but differ from source to source. This suggests that they reflect some very fundamental property of the system. According to the 'no-hair' theorem, every black hole is entirely characterised by three externally observable parameters: mass, angular momentum and electrical charge. Ignoring charge[2], there are two parameters only to describe a black hole, the mass and the spin, which completely determine the structure of the surrounding spacetime and drive the particle motion in the gravitational field.

[2] All matter we observe in the universe appears to be on average electrically neutral, therefore black holes formed from such matter are believed to have no or a very small charge.

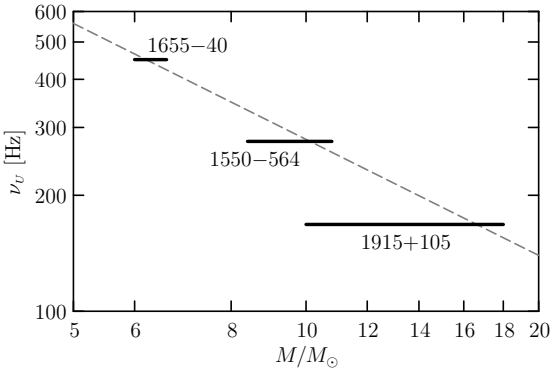

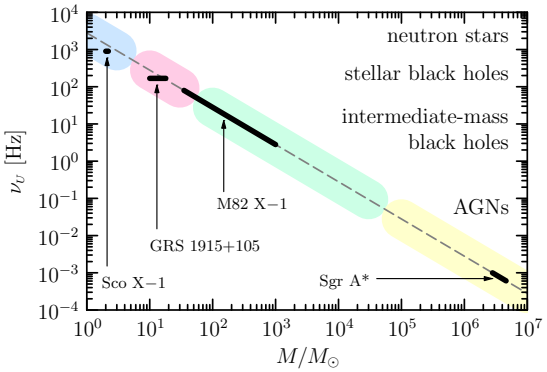

FIGURE 1.3a: The frequency–mass scaling for XTE J1550−564, GRO J1655−40, and GRS 1915+105. The upper frequencies of 3 : 2 pairs are plotted vs. measured masses. The dashed line shows the best fit relation, $\nu_U = 2.8$ kHz $(M/M_\odot)^{-1}$. (Adopted from McClintock & Remillard 2005.)

FIGURE 1.3b: The global frequency–mass scaling across the range of masses. This illustration shows the microquasar 'best fit' relation (1.1), *dashed line*, extended to the range of masses going from 1 up to 10^7 $M_\odot$. Colour bars represent different classes of objects and thick black lines show some individual objects including the neutron star Sco X−1, the microquasar GRS 1915+105, the speculative intermediate-mass black hole M 82 X−1 and the Galactic super-massive black hole Sgr A*. The line lengths indicate the uncertainties in the mass and/or frequency estimates for the objects. (Idea from Török 2005a.)

In strong gravity, the typical length-scale is the gravitational radius, $r_\mathrm{g} \sim M$, and the typical velocity is the speed of light, $c = 1$. Thus, the typical frequency is $\nu \sim c/r_\mathrm{g} \sim 1/M$ and scales inversely proportional with mass. This is also the case for the Keplerian orbital frequency and for all other frequencies of a test particle motion in a gravitational field (Appendix A). If HFQPOs originate in the fluid motion in the accretion flow, their frequencies should also scale as $1/M$, assuming that they stay around a same place.

Indeed, initially Remillard *et al.* (2002) and later McClintock & Remillard (2005) reported that for three microquasars showing the 3 : 2 QPO frequency pairs, where the mass is known independently from optical measurements, the relationship between the HFQPO frequencies and BH masses scale as $1/M$ (Figure 1.3a) and can be well fitted by a formula

$$\nu_U = 2.8 \text{ kHz} \left(\frac{M}{M_\odot}\right)^{-1} . \tag{1.1}$$

It is a very interesting finding, because there is an ambiguity in the angular momentum of black holes, which affects orbital frequencies and can destroy the $1/M$ scaling. Hence, the fact that within uncertainties in mass measurements the formula (1.1) can fit all three sources suggests that they all may have a similar spin and moreover that QPOs are produced by the same type of mechanism in every source.

A confirmation of the scaling law has the crucial importance for possible explanations of HFQPOs. It strongly supports models that identify the oscillations with some type of orbital motion in the accretion disc. If the origin of oscillations is the same in neutron stars and black holes, it should be possible (with respect to differences in spin, spacetime structure and magnetic fields) to roughly rescale the basic QPO properties between the two classes of sources.

$1/M$ scaling across the range of masses

It is interesting to find out that this inverse-mass-scaling law can be extended over a wide range of masses (Figure 1.3b). Having stellar-mass black holes at one end of the spectrum of masses, we can apply the Mirabel & Rodriguez (1998) general analogy between microquasars and quasars to the properties of accretion disc oscillations as well and we expect frequencies in the millihertz–microhertz range in the case of active galactic nuclei at the opposite end of the mass spectrum. If ultra-luminous X-ray sources contained intermediate-mass black holes, which is still a speculation (*e.g.* King *et al.* 2001), they would lie in between, in the decihertz–millihertz range.

Sgr A* is the closest super massive black hole, sitting right in the centre of our Galaxy. From the analysis of orbits of proximate stars within $10-1000$ light hours off Sgr A*, the current best estimate of the central mass is $(3.7\pm0.2)\times10^6\,(R_*/8\,\mathrm{kpc})^3\,M_\odot$ (Ghez *et al.* 2005), where the uncertainty in the Galactic centre distance adds an additional 19% error. This gives the mass of the black hole in Sgr A* most likely to be in the interval $2.8-4.6\times10^6\,M_\odot$. Genzel *et al.* (2003) measured a 17-minute (1020 s) quasi-periodic variability in an infrared emission originating from within several tens of Schwarzschild radii from the black hole during flaring events. More recently, Aschenbach *et al.* (2004) have reported three other QPO periods, 700 s, 1150 s, 2250 s, in the two brightest X-ray flares from the Galactic centre. Although the quality of the used light curves is very low and the resuts have not been so far independently confirmed, the ratio of reported periodicities is $3.21:1.96:1$, *i.e.* the possible 'Keplerian' frequencies found in Sgr A* are close to form a commensurable sequence $3:2:1$ (Aschenbach 2004).

Mucciarelli *et al.* (2005) have recently published an observation of a variable QPO at frequencies from 50 to 166 mHz in the ULX source M 82 X−1, which appears to be an analog of the type-C low frequency QPO (see McClintock & Remillard 2005) known from microquasars. Although this QPO is not a part of a HFQPO pair, if the inverse-mass-scaling law is applied to its observed frequency range, one gets a black hole mass anywhere in the interval few tens to 1000 $M_\odot$. Then the expected frequency for the detection of HFQPO in this source would be between 3 and 90 Hz.

1.4 The Bursa line

Immediately after the discovery of kHz QPOs in neutron-star sources it was realised that flux variations at frequencies in this range could arise from the orbital motion of accreting matter very near the compact object or from a beat between the orbital motion and the spin of the neutron star (van der Klis *et al.* 1996; Strohmayer *et al.* 1996c).

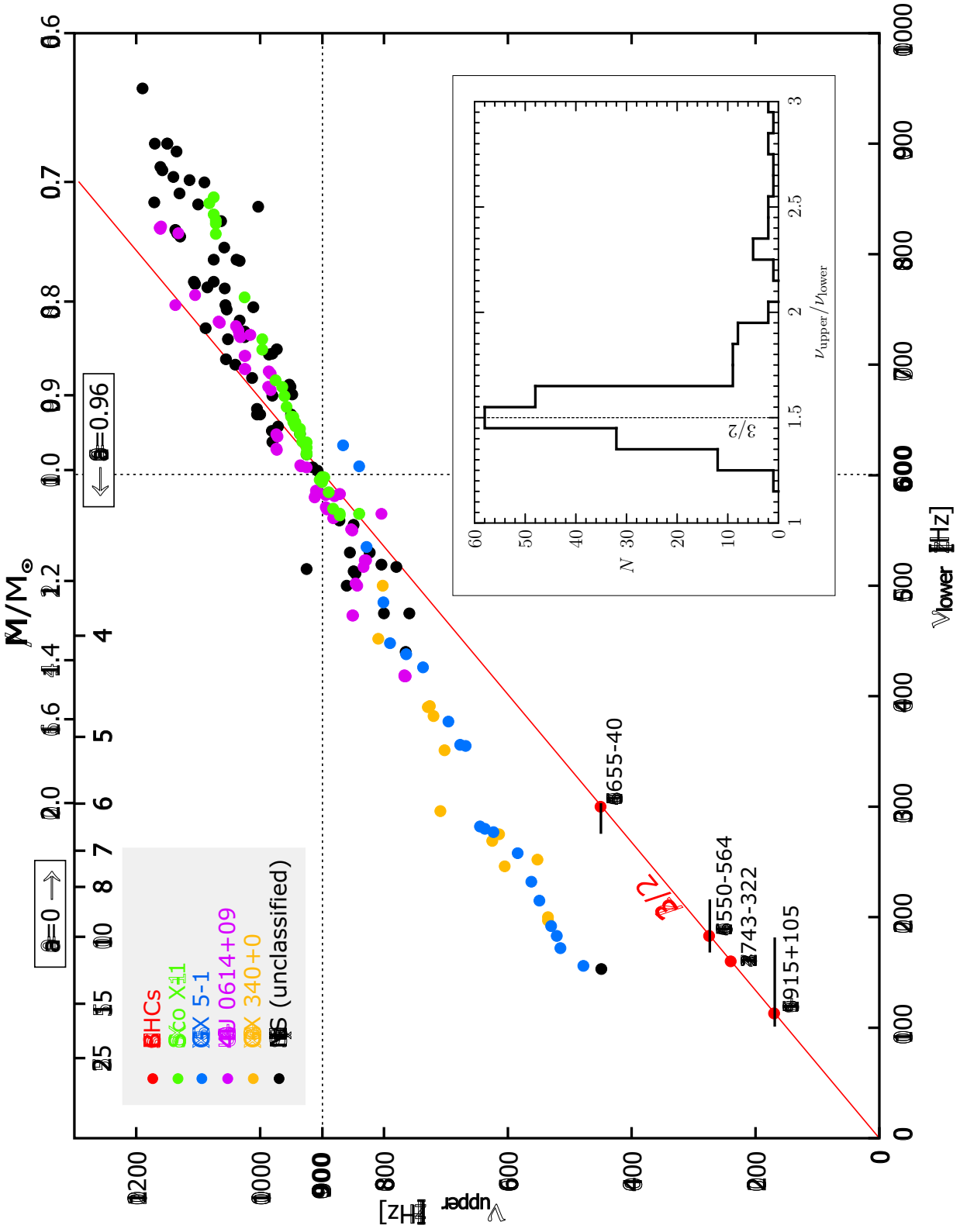
a=0
a=0.96
M/M⊙
ν_upper [Hz]
ν_lower [Hz]
HCs
Sco X-1
4U 0614+09
XTE J1650-500
GX 5-1
GX 340+0
NS (unclassified)
GRO J1655-40
XTE J1550-564
GRS 1915+105
2:1
3/2
N
ν_upper/ν_lower

FIGURE 1.3: The Bursa plot. The figure shows HFQPO observations from all Galactic microquasars, where both QPO peaks have been detected, as well as a large subset of HFQPO detections from neutron-star sources published between 1996−2002. It summarizes all relevant features and prominent properties of the high-frequency QPO phenomenon like the frequency−frequency correlation, the frequency ratio distribution and the mass scaling.

Black-hole sources: Each microquasar is represented by exactly one point (*red*), as their frequencies are fixed and do not change in time. The ratio between the upper and lower QPO frequency is always sharply 3 : 2. Thus, the four sources lie narrowly on one line with the slope 3/2 (*red line*). McClintock & Remillard (2005) noted that the observed frequencies scale inversely with mass. The black horizontal bars show the mass estimates for the central black holes inferred from optical measurements of radial curves. The masses can be read against the mass axis see the description bellow.

Neutron-star sources: The twin QPO frequencies are known to wander significantly in NS sources. Therefore, there are numerous frequency pairs for each source in the plot. Individual HFQPO observations of four neutron stars (4U 0614+09, Sco X−1, GX 5−1, GX 340+0) are indicated by colour-coded points. Other sources, where less data points were available, are jointly ploted with black points. It is clearly visible that all points cluster along a single line (the so called *'Bursa line'*), although they come from observations of different sources with different properties. This universality together with the mass scaling suggest that the origin of QPOs may be connected to strong gravity (see text). The Bursa line intersects the 3/2 line of black holes at about $[600, 900]$ Hz.

Histogram: The inset histogram shows the combined distribution of the HFQPO frequency ratios for sources: 4U 0614+09, 4U 1908−52, 4U 1636−53, 4U 1702−43, 4U 1705−34, 4U 1728−34, 4U 1735−44, 4U 1820−30, 4U 1915−05, Cyg X−2, GX 17+2, GX 340+0, GX 349+2, KS 1731−26 and XTE J2123−058. The distribution clusters prominently around the ratio 3 : 2 (Abramowicz, Bulik, Bursa & Kluźniak 2003; see also Section 1.6), which however may not reflect the true distribution of frequency ratios, as data were not collected from observation intervals of an equal duration. The clustering was confirmed by a detailed study of Belloni *et al.* (2005), though.

Mass axis: The secondary x-axis on the top of the figure gives expected masses of objects with given frequencies. The masses are calculated in the framework of the resonance model under the assumption that the two HFQPO frequencies correspond to the frequencies of the vertical and radial epicyclic motion of a test particle orbiting at a particular radius, where these frequencies are in the exact 3 : 2 ratio (the parametric resonance; see Chapter 2 for a discussion of the resonance models). Therefore it works only for points lying on the red 3/2 line. The axis has two sets of values: one for the spin parameter $a=0$, which gives lower masses and applies to neutron-star sources; second for spin parameter $a=0.96$, which gives higher masses and is appropriate to black-hole sources.

Two main competing interpretations existed, which made explicit predictions for the separation frequency $\Delta\nu$. The relativistic precession model (Stella & Vietri 1998, 1999; Stella *et al.* 1999) assumed eccentric orbits of test particles around a compact object and identified the upper kHz QPO with the Keplerian orbital frequency in the inner disc and the lower QPO with the periastron precession of the orbit. The model predicted that the distance between QPO peaks should decrease both when the kHz QPO frequencies increase and when they sufficiently decrease. In the concurrent sonic-point beat frequency model (Miller, Lamb & Psaltis 1998), the production of the upper QPO peak was identified with the orbital motion of a gaseous clump at the inner edge of the disc and the beat between this clump and the neutron star spin frequency produced the lower QPO peak. Here, $\Delta\nu$ was in principle expected to be equal to the neutron star spin, but should decrease when the upper QPO frequency increases due to the radial inward motion of the clump. Therefore, a strong observational effort was devoted to measure the peak separation in order to test predictions of the two models.

From early observations it seemed that the distance of the the two peaks in HFQPOs was constant (Strohmayer *et al.* 1996a,b) while the peaks changed their frequency. In the source 4U 1728−34 the separation frequency was in addition consistent with the spin frequency of the neutron star inferred from simultaneous observations of burst oscillations (Strohmayer *et al.* 1997). This fact was originally the main motivation for the beat-frequency model. But it was soon recognised that the distance of the peaks varies (van der Klis *et al.* 1997; Méndez *et al.* 1997). In Sco X−1 the peaks were observed to move closer together by ∼80 Hz, while they both moved up in frequencies by ∼200 Hz. Similar behaviour was at the same time reported from the atoll source 4U 1608−52 (Méndez *et al.* 1998) and later also from other sources. In a few cases a positive correlation between the position and distance of the peaks was observed at the lowest detectable frequencies.

Psaltis *et al.* (1998) tested the possibility that the peak separation was varying in all sources in a similar way as it had been seen in Sco X−1. They found available data for other sources insufficient when used individually, but they showed that the frequencies of the lower and upper kHz QPOs in the combined data set of nine sources are correlated and fairly closely follow a power-law fit for Sco X−1 data, $\nu_U \propto \nu_L^{0.53}$. Based on this correlation they concluded that the peak separation may be varying in all sources in a similar way.

While concentrating on the relationship of $\Delta\nu$ to other frequencies, the fact that the two frequencies are remarkably tightly correlated among sources did not get much publicity. Later, after available observational data published until February 2002 had been collected for as many sources as possible, this correlation was reproduced and an important fact was pointed out (Bursa 2002, unpublished) that the frequency correlations of individual sources can be well described by linear functions, parameters of which slightly differ from source to source (examples are given in Figure 1.4; see also Appendix D).

The strong linear correlation between the two kHz QPO frequencies (shown and commented in Figure 1.3) spans a wide range of frequencies from 150 to 950 Hz in ν_L and covers all NS sources. It can be fitted by a linear relation (the *'Bursa line'*)

$$\nu_U = A_0\,\nu_L + B_0\ , \tag{1.2}$$

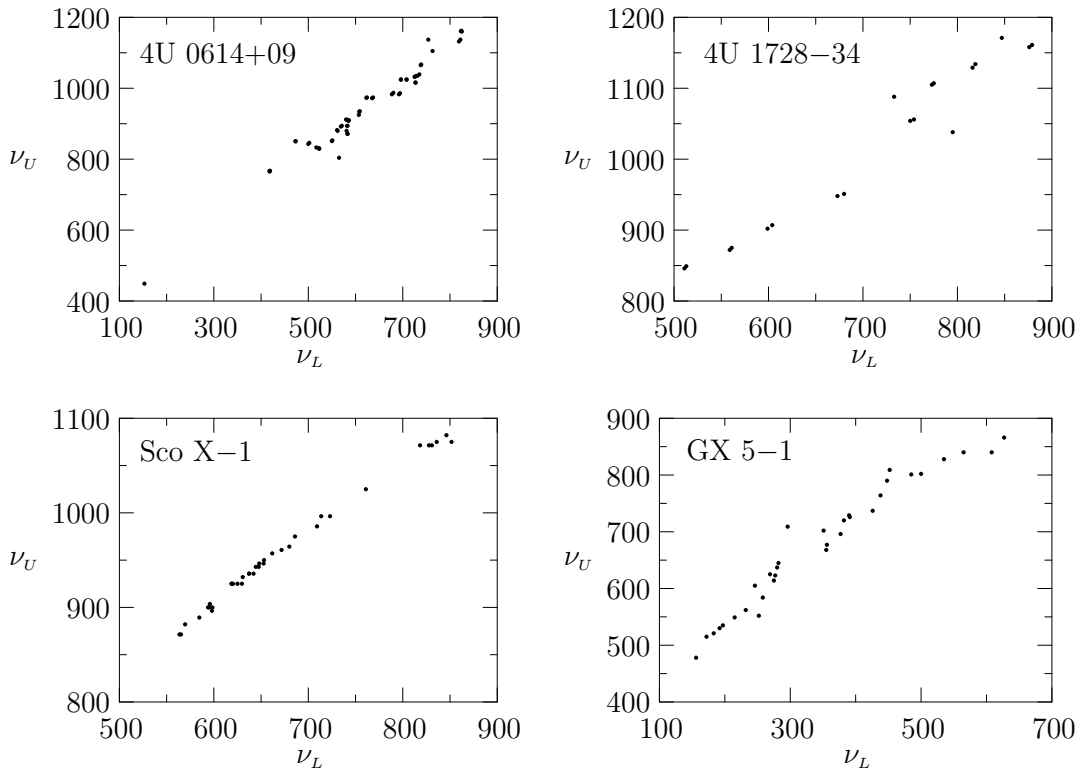

FIGURE 1.4: The linear correlation between the two HFQPO frequencies in 4U 0614+09 (*top, left*) and 4U 1728−34 (*top, right*), Sco X−1 (*bottom, left*) and GX 5−1 (*bottom, right*). Points represent individual detections of the HFQPO pairs.

with coefficients $A_0 = 0.90 \pm 0.01$ and $B_0 = 371 \pm 8$ Hz. Despite that different NS sources can have different properties and conditions, the fact that HFQPO frequencies cluster along a common line has a special importance. It suggests that the mechanism of kHz QPOs is the same in every source and moreover that it is driven by parameters, which do not largely differ among sources. The line itself crosses the 3/2 line, which brings to a relevance high-frequency QPOs in black holes. We will see in Section 1.6, how it may be related to the mass scaling.

1.5 Linear fits to the frequency–frequency correlation

The correlation between the upper and the lower kHz QPO frequencies across different sources or for a particular source can be well fitted by a power law function, as it was initially shown by Psaltis *et al.* (1998), as well as by a linear function (Bursa; see also Belloni *et al.* 2005). Using the non-linear least-squares method we compare these two functional relations together with some other possibilities.

The production mechanism of kHz QPOs is still an open issue and numerous models have been proposed to explain the observational evidence. The key issue is to reproduce the correlation between the two frequencies and explain the relation to the spin frequency of the neutron star. We use the following six functions to fit the frequency–frequency correlation and we will test goodness of each of them by the non-linear least-squares method. The functions we consider are:

$$\text{LIN}: \quad \nu_U = A\,\nu_L + B\,, \tag{1.3a}$$

$$\text{PWL}: \quad \nu_U = A\left(\frac{\nu_L}{600\ \text{Hz}}\right)^B\,, \tag{1.3b}$$

$$\text{SQR}: \quad \nu_U = A\,\nu_L^2 + B\,, \tag{1.3c}$$

$$\text{SQR+L}: \quad \nu_U = A\,\nu_L^2 + B\,\nu_L + C\,, \tag{1.3d}$$

$$\text{SQRT}: \quad \nu_U = A\,\sqrt{\nu_L} + B\,, \tag{1.3e}$$

$$\text{SQRT-0}: \quad \nu_U = A\,\sqrt{\nu_L}\,. \tag{1.3f}$$

The selection is based on conjectures of the frequency relation given by proposed models of QPOs. Several of the models (*e.g.* the epicyclic resonance model, ...) predict a linear correlation of frequencies in the first order approximation, but higher orders give additional non-linear terms. Other models (*e.g.* relativistic precession model, ...) predict a rather complicated behaviour with fractional powers of ν_L. Alfvén wave model gives approximately a square-root relation $\nu_U(\nu_L)$. Therefore, we consider a linear fit (LIN), a power law (PWL), quadratic fits with or without a linear term (SQRT+L, SQRT), and fits with the square root of ν_L (SQRT, SQRT-0). The last two options are also sustained by the fact that the power-law best fits give values of the exponent typically close to 0.5 for most sources.

For the least-squares analysis we use the frequency data extracted from the literature published between 1996 – 2002. From this set, four atoll and four Z sources are selected for which at least 10 frequency pairs are available. The sources and references to the literature are listed in Table 1.2. For each function 1.3a – 1.3f we make the best fits to the QPO frequency pairs of the selected sources. Unfortunately, errors of frequency measurements cannot be determined from all references, therefore we consider all points with an equal weight. Typical errors are, however, a few Hertz. From the best fits we compute the sum of squared residuals reduced to the number of degrees of freedom (RSSR). The resulting sums for individual sources as well as total sums over all eight sources are summarized in Table 1.2.

By eye-inspection of the frequency–frequency correlations, we see that the relation between frequencies is close to linear, with some small deviations. It is then not surprising that it can be best fitted (*i.e.* with the minimal value of RSSR) by the most general quadratic function with a linear and a constant term. However, this function has three free parameters, one more than other functions, and it is thereby expected to give the best

		$\sum$(residuals)^2/d.o.f.						
Source	type	LIN	PWL	SQR	SQR+L	SQRT	SQRT-0	References
4U 0614+09	A	614	734	1179	626	831	1139	[9,10,11]
4U 1608−52	A	281	200	1269	176	195	287	[5,9,12]
4U 1636−53	A	127	134	3152	145	134	130	[5,6,9]
4U 1728−34	A	730	760	1079	767	779	1350	[1,5,11]
GX 5−1	Z	717	442	3867	402	461	770	[4,7]
GX 17+2	Z	288	221	638	152	207	487	[3]
GX 340+0	Z	991	713	3539	645	737	936	[4,9]
Sco X−1	Z	26	16	984	12	16	22	[8]
Atoll		1752	1828	6679	1714	1939	2906	
Z		2022	1392	9028	1211	1421	2215	
TOTAL		3774	3220	15707	2925	3360	5121	

TABLE 1.2: Goodness of different functional fits to the frequency data of selected atoll and Z sources. The table lists sums of squared residuals per degrees of freedom from the best fits given by different functions. The last row gives the total sum of residuals over all eight sources and partial sums over atoll and Z classes are given on the two precedent lines.
References: [1] Di Salvo *et al.* (2001), [3] Homan *et al.* (2002), [4] Jonker *et al.* (2000a), [5] Jonker *et al.* (2000b), [6] Jonker *et al.* (2002a), [7] Jonker *et al.* (2002b), [8] van der Klis *et al.* (1997), [9] van der Klis (2000), [10] van Straaten *et al.* (2000), [11] van Straaten *et al.* (2002), [12] van Straaten *et al.* (2003).

results. Giving a 100% goodness mark to SQR+L model, PWL and LIN fits follow with 91% and 77% of goodness, respectively. Surprisingly good fits, 87%, can by obtained by SQRT. SQRT-0 (57%) and SQR (19%) functions do not fit the data sufficiently well.

Figures 1.5 − 1.10 show the ν_U–ν_L and the $\Delta\nu$–ν_L relations for the eight sources with their best LIN, PWL and SQRT fits. In Figures 1.11 − 1.12 these three fits are plotted together for a comparison. We can see from these plots and also from Table 1.2 that Z sources clearly diverge from the simple linear trend, although the deviations are very small and a linear function can still make a good fit. Atoll sources, on the other hand, are much better fitted by straight lines than by power laws and not even quadratic fits (SQR+L) can improve significantly over the linear ones. That reflects the known fact that atoll and Z sources are different (Hasinger & van der Klis 1989; van der Klis 2000), showing certain distinctions in their spectra and time variability.

Conclusions can be made that linear fits to the frequency–frequency correlations are sufficiently good to reflect the basic characteristics of the relation. In Z sources, where there are small deviations from the linear trend, they still describe the correlations with an accuracy better than ∼5%. In atoll sources, linear fits are equally good to fit the data as are PWL or SQRT models.

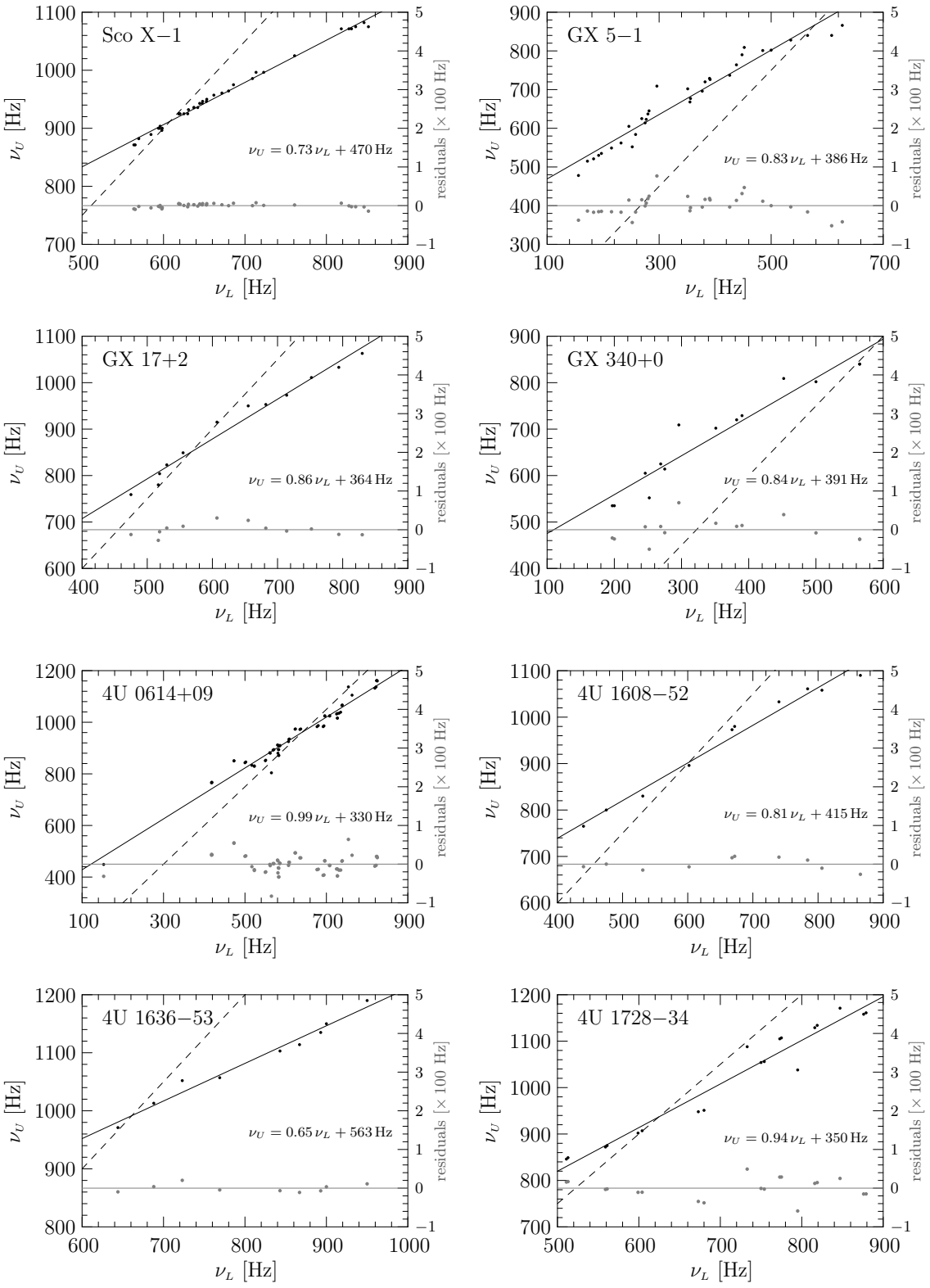

FIGURE 1.5: Correlations between the individual observations of the ν_U and ν_L frequencies in selected neutron-star sources. Measured pairs of HFQPO frequencies (*black dots*), the best LIN fit through the data (*solid black line*), its coefficients and the residuals (*gray dots*) are indicated. Also ploted is the 3/2 black-hole line (*dashed line*). Error bars are not shown, as they are not known for all data points, otherwise they are typically a few Hertz.

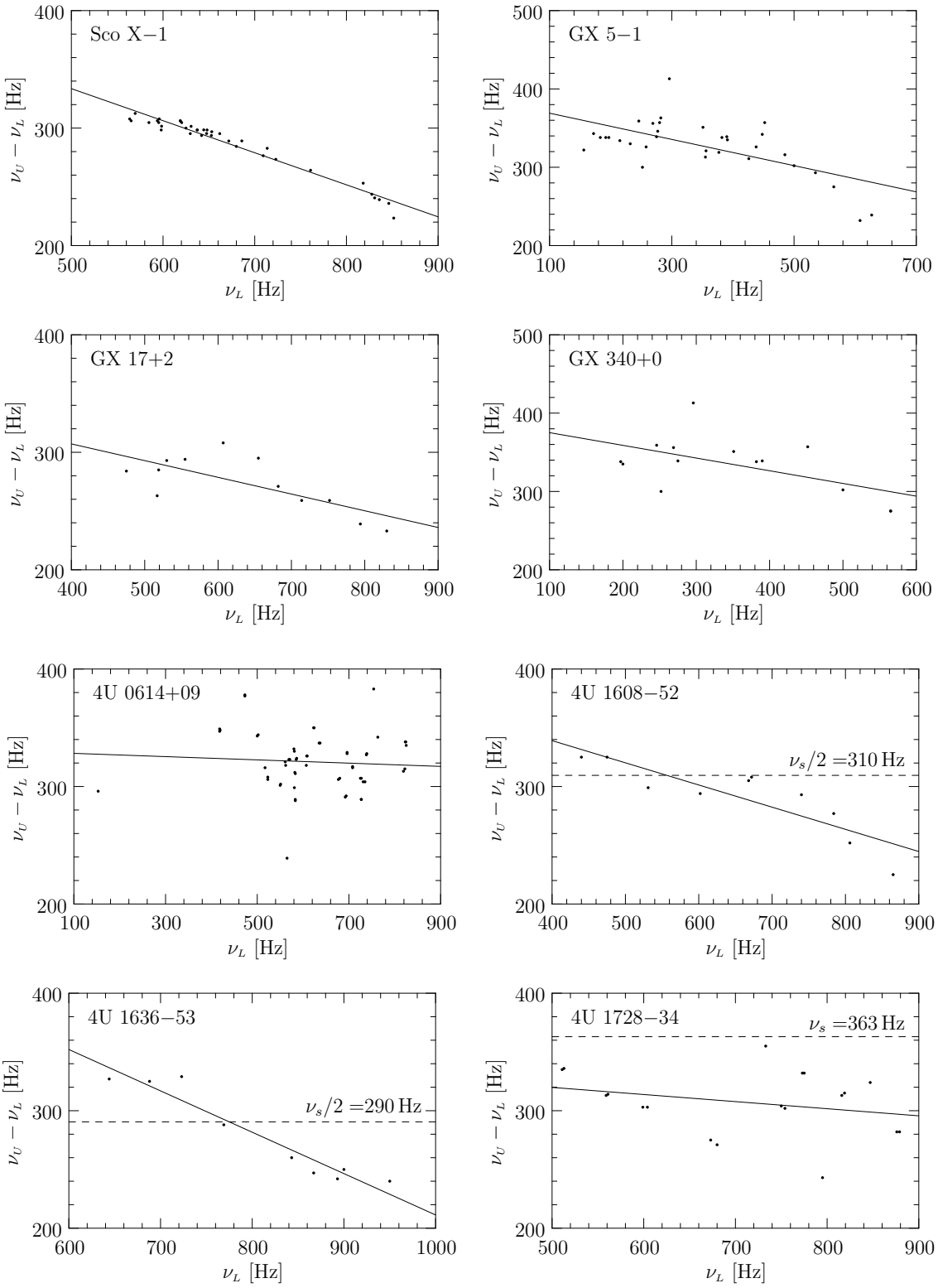

FIGURE 1.6: Correlation between $\nu_U - \nu_L$ and ν_L in selected neutron-star sources. Measured pairs of HFQPO frequencies (*black dots*) and the curve predicted by the best LIN fit through the data (*solid line*) are indicated. If available, also ploted is the spin frequency of the neutron star or half of it (*dashed line*).

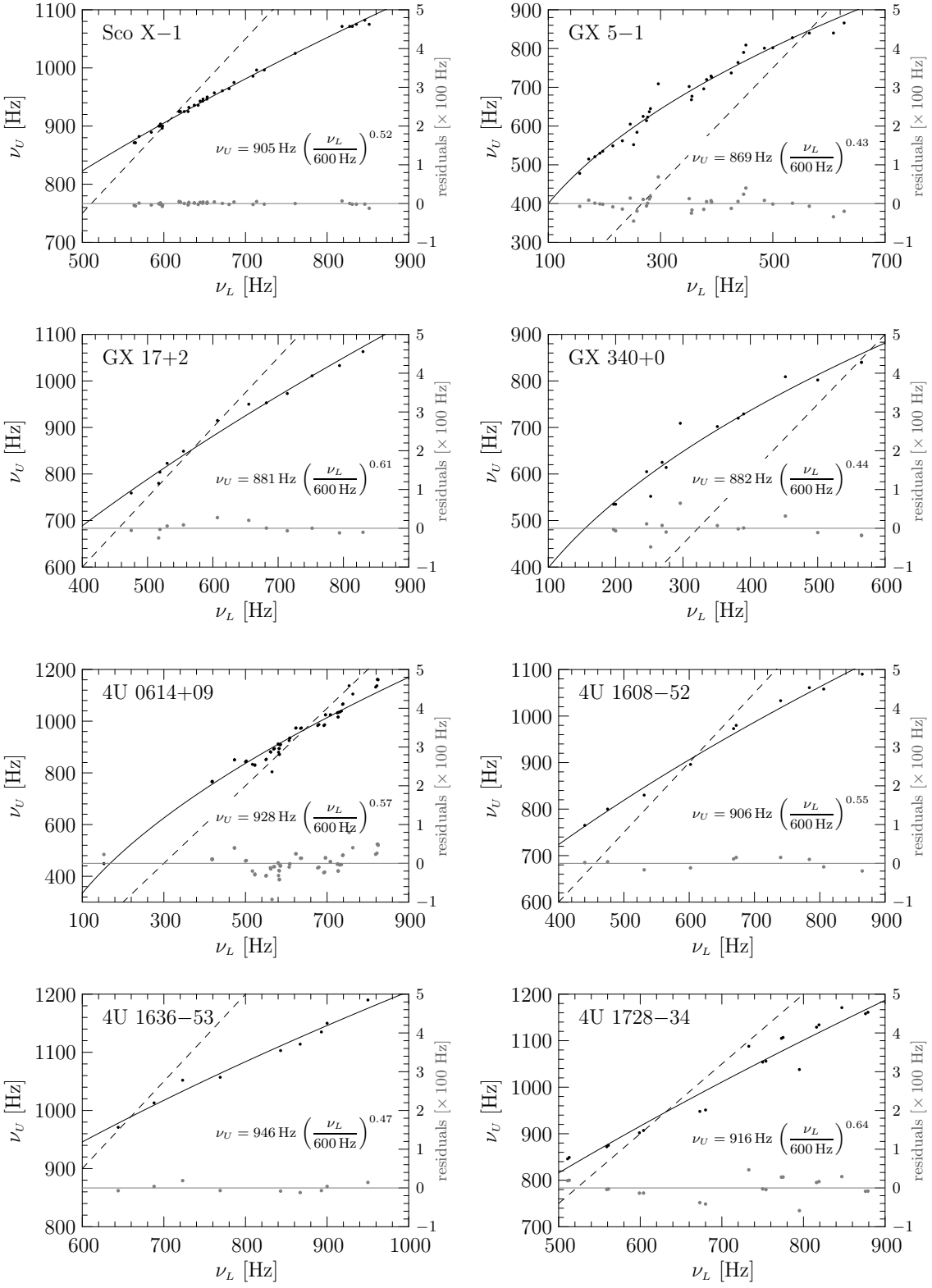

FIGURE 1.7: Correlations between the individual observations of the ν_U and ν_L frequencies in selected neutron-star sources. Measured pairs of HFQPO frequencies (*black dots*), the best PWL fit through the data (*solid black line*), its coefficients and the residuals (*gray dots*) are indicated. Also ploted is the 3/2 black-hole line (*dashed line*). Error bars are not shown, as they are not known for all data points, otherwise they are typically a few Hertz.

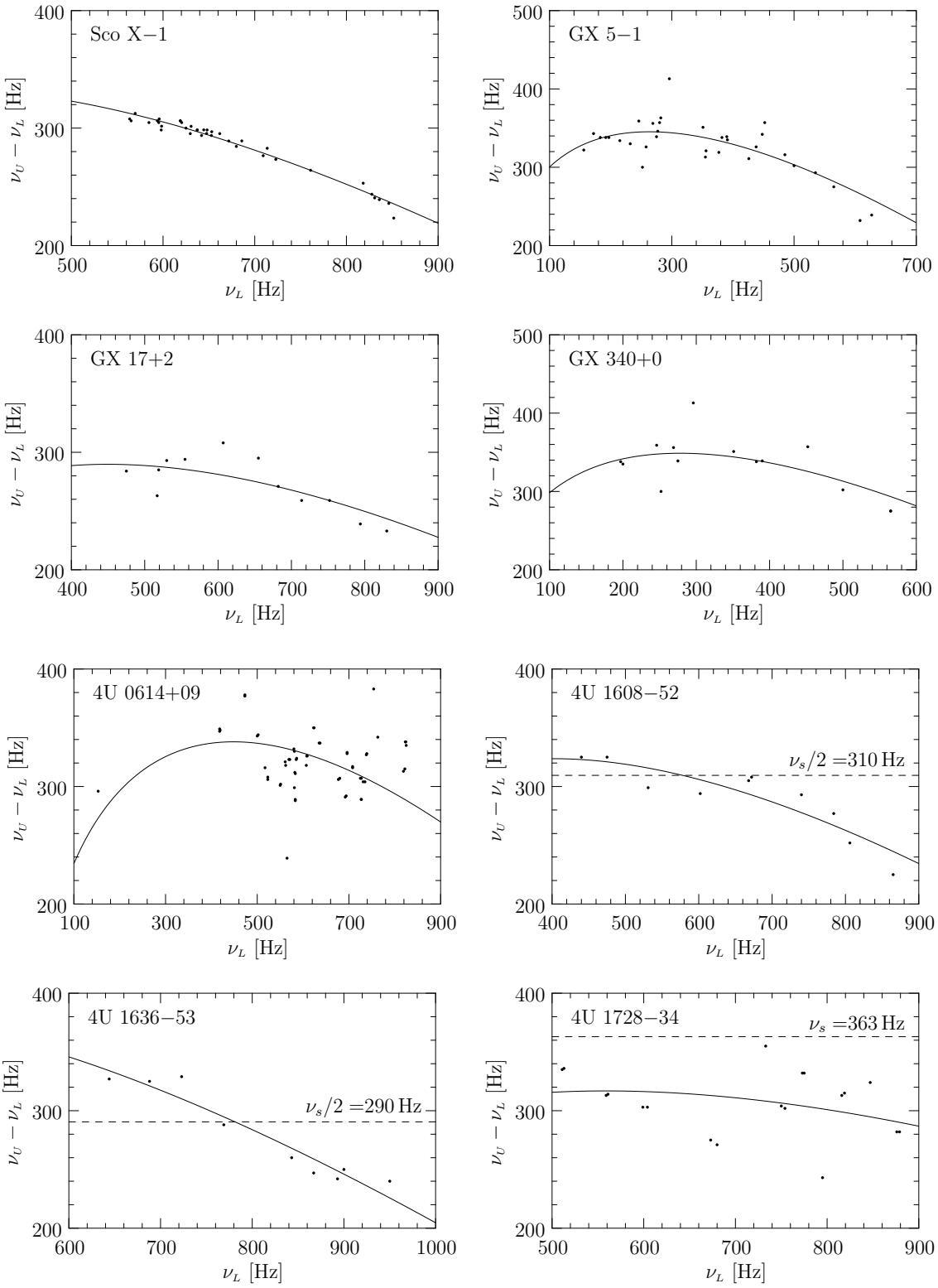

FIGURE 1.8: Correlation between $\nu_U - \nu_L$ and ν_L in selected neutron-star sources. Measured pairs of HFQPO frequencies (*black dots*) and the curve predicted by the best PWL fit through the data (*solid line*) are indicated. If available, also ploted is the spin frequency of the neutron star or half of it (*dashed line*).

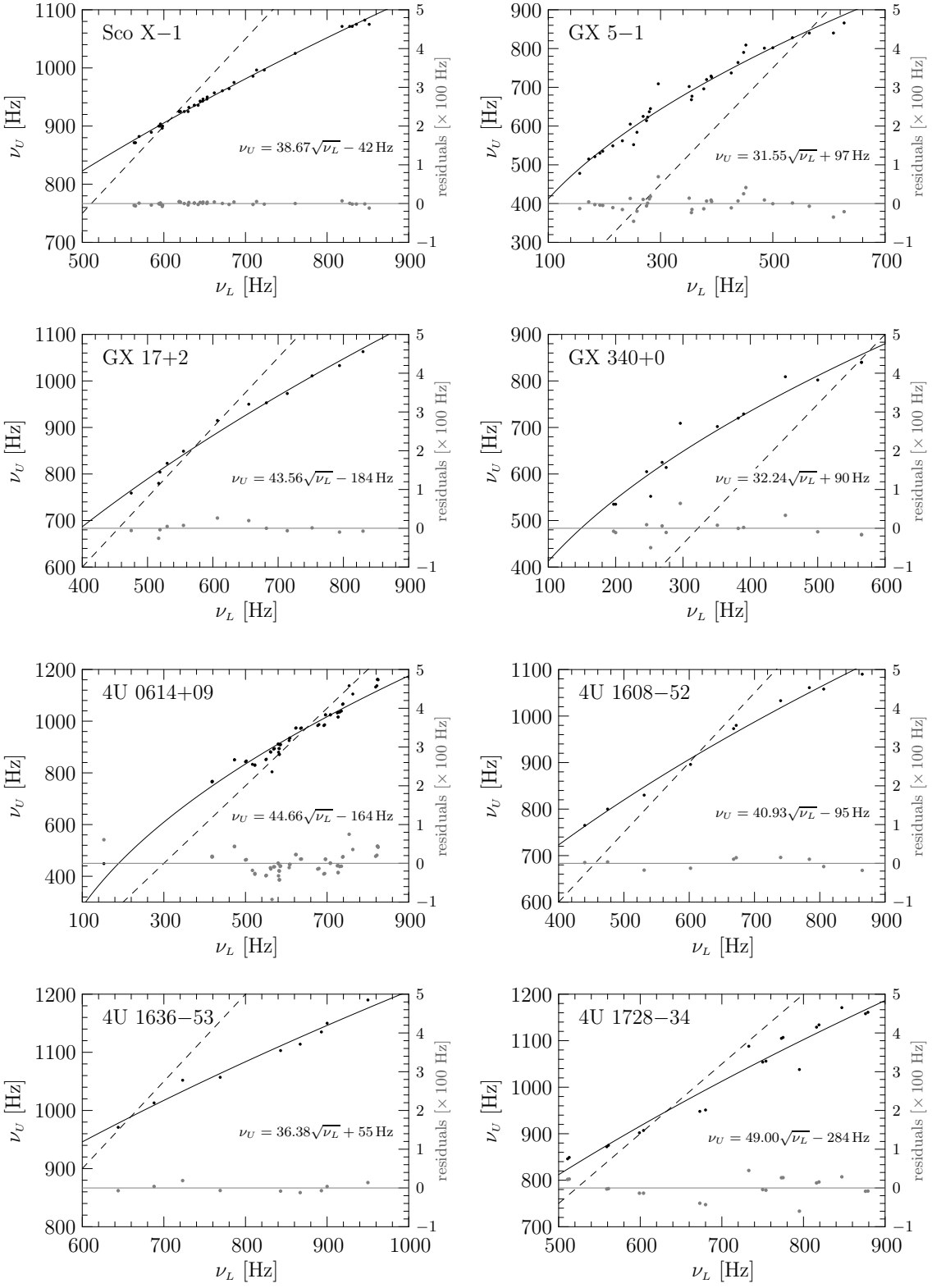

FIGURE 1.9: Correlations between the individual observations of the ν_U and ν_L frequencies in selected neutron-star sources. Measured pairs of HFQPO frequencies (*black dots*), the best SQRT fit through the data (*solid black line*), its coefficients and the residuals (*gray dots*) are indicated. Also ploted is the 3/2 black-hole line (*dashed line*). Error bars are not shown, as they are not known for all data points, otherwise they are typically a few Hertz.

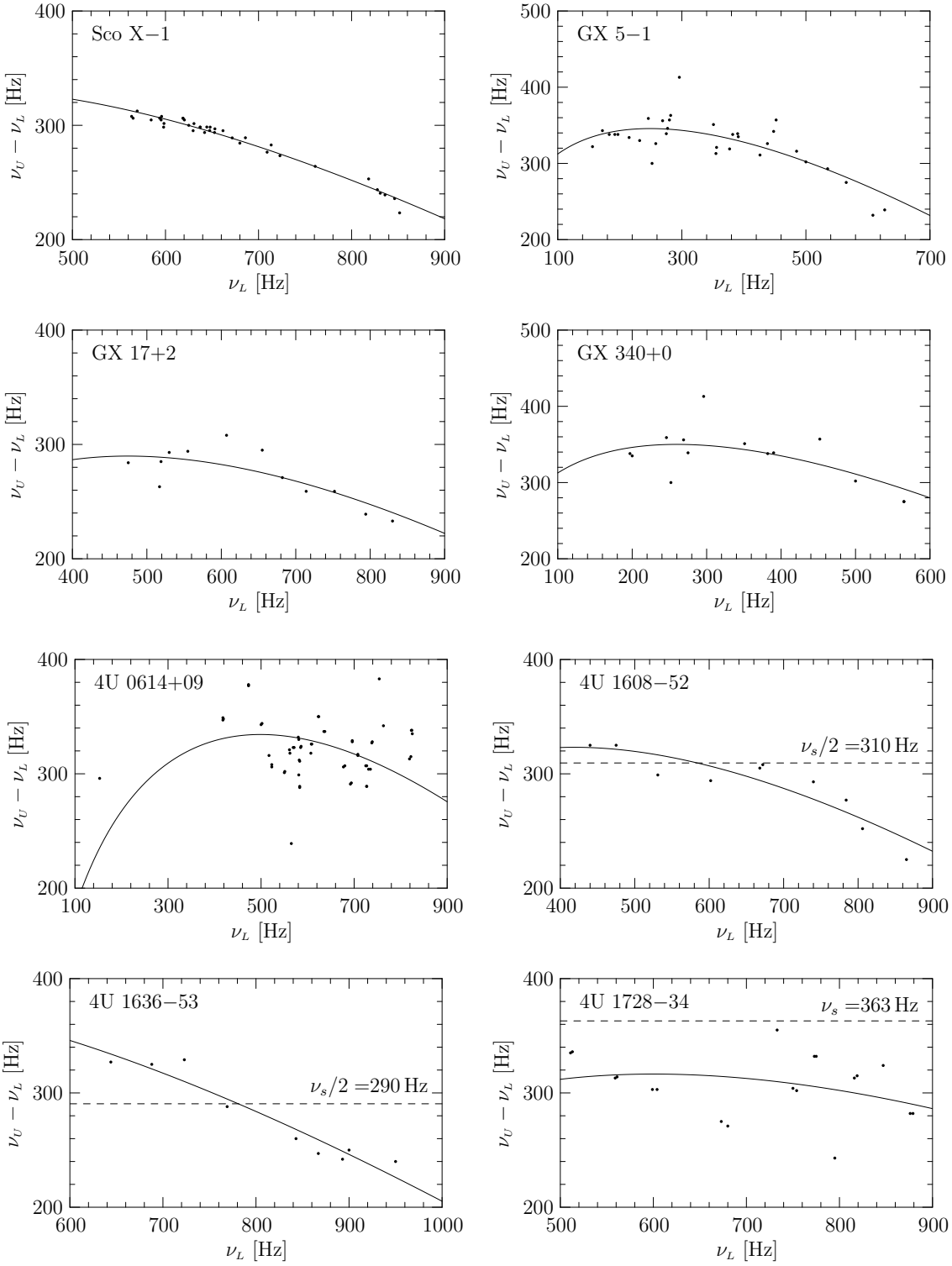

FIGURE 1.10: Correlation between $\nu_U - \nu_L$ and ν_L in selected neutron-star sources. Measured pairs of HFQPO frequencies (*black dots*) and the curve predicted by the best SQRT fit through the data (*solid line*) are indicated. If available, also ploted is the spin frequency of the neutron star or half of it (*dashed line*).

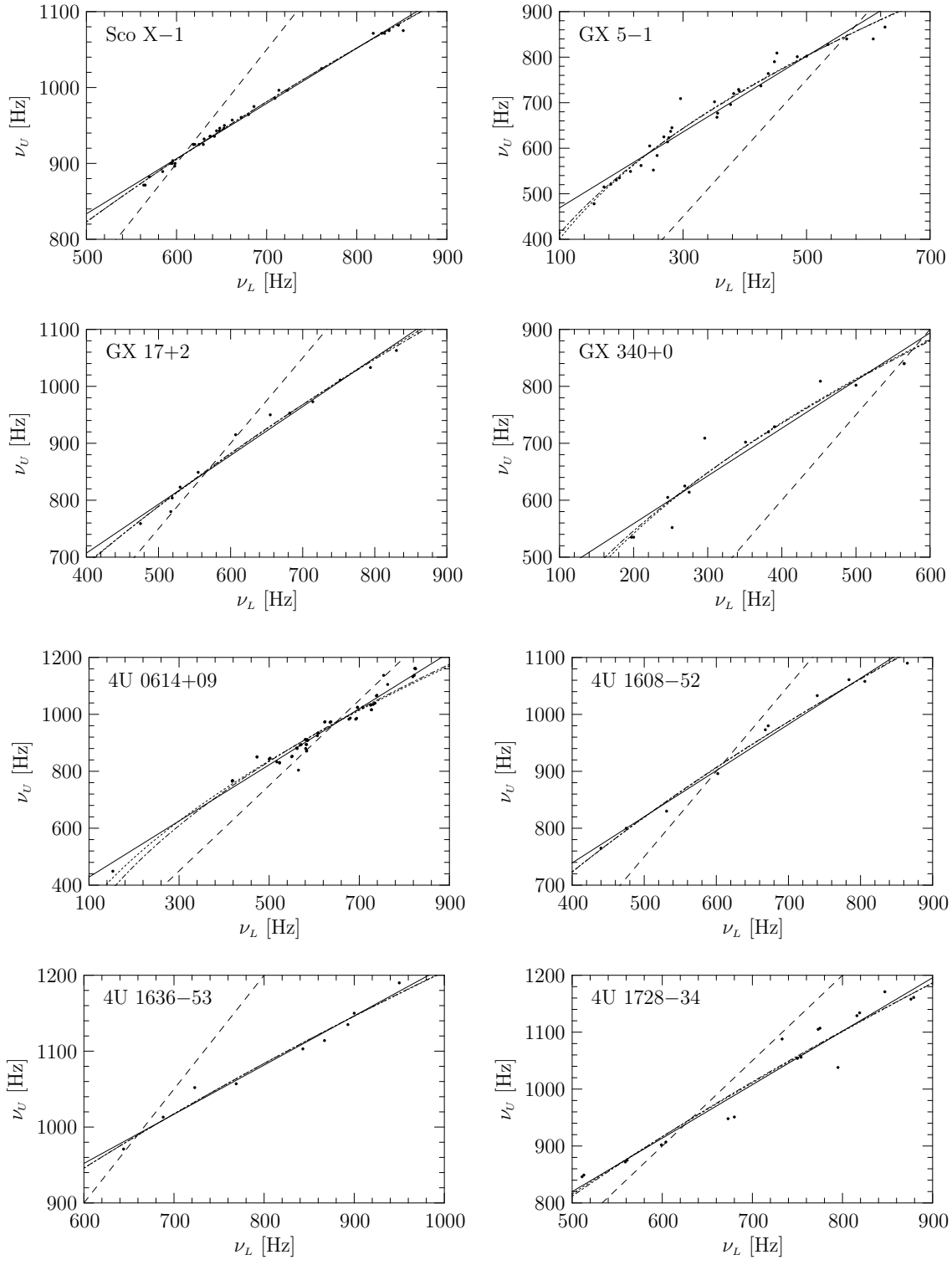

FIGURE 1.11: Correlations between the individual observations of the ν_U and ν_L frequencies in selected neutron-star sources. Measured pairs of HFQPO frequencies (*black dots*), the best LIN (*solid line*), PWL (*dotted line*) and SQRT (*dash-dotted line*) fits through the data are indicated. Also ploted is the 3/2 black-hole line (*dashed line*). Error bars are not shown, as they are not known for all data points, otherwise they are typically a few Hertz.

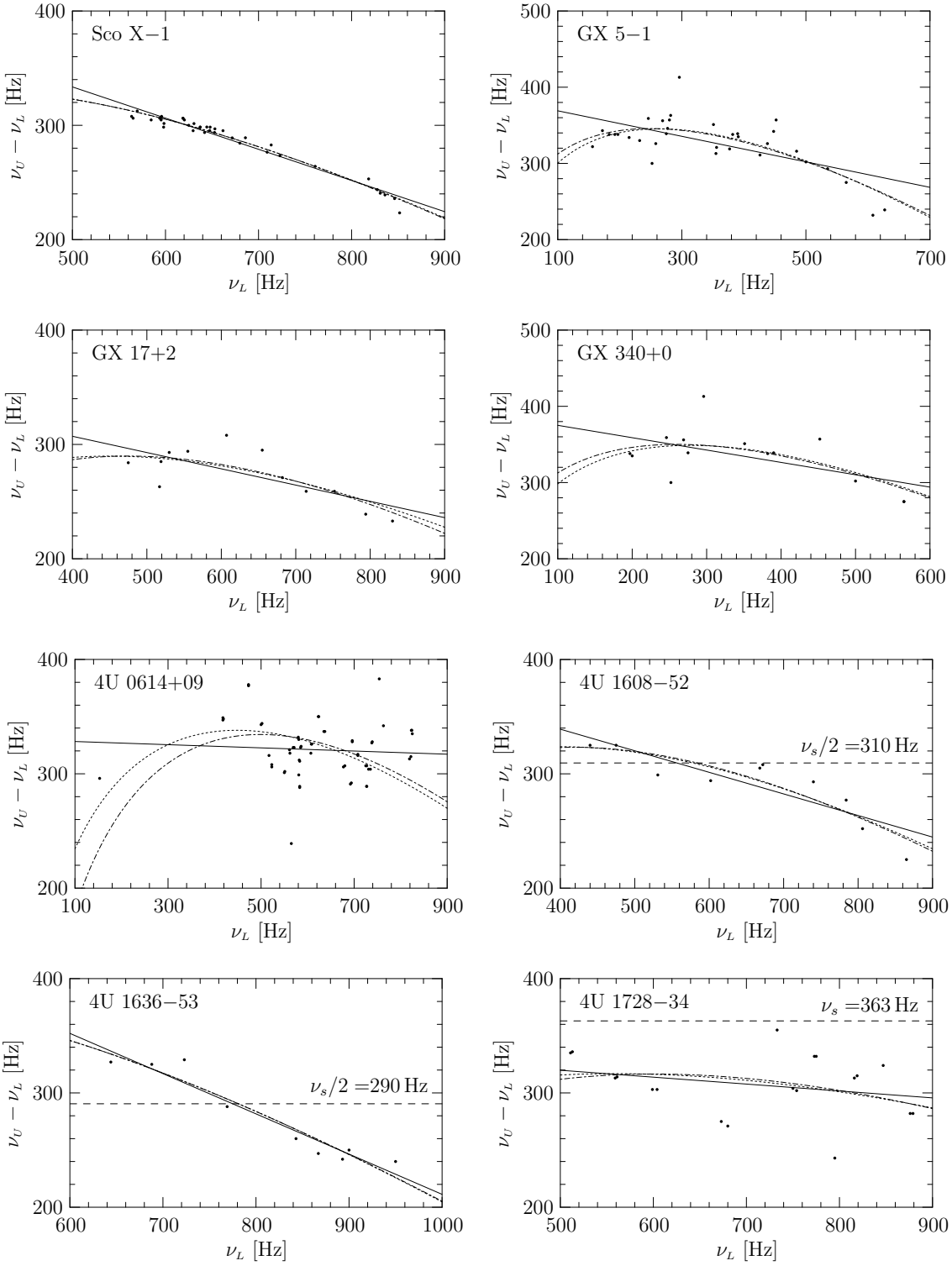

FIGURE 1.12: Correlation between $\nu_U - \nu_L$ and ν_L in selected neutron-star sources. Measured pairs of HFQPO frequencies (*black dots*) and the curves predicted by the best LIN (*solid line*), PWL (*dotted line*) and SQRT (*dash-dotted line*) fits through the data are indicated. If available, also ploted is the spin frequency of the neutron star or half of it (*dashed line*).

1.6 Anti-correlation between the slope and shift

Double peak kHz QPO frequencies in neutron star sources vary in time by a factor of hundreds Hertz, while in microquasar sources the frequencies are fixed and located at the line $\nu_U = 1.5\,\nu_L$ in the frequency–frequency plot. The crucial question in the theory of twin HFQPOs is whether or not those observed in neutron-star systems are essentially different from those observed in black holes. In black-hole systems the twin HFQPOs are known to be in the 3 : 2 ratio for each source. At first sight, this seems not to be the case for neutron stars. For each individual neutron star, the upper and lower kHz QPO frequencies, ν_U and ν_L, are with high accuracy linearly correlated, $\nu_U = A\,\nu_L + B$, with the slope $A < 1.5$ (see Figure 1.3), *i.e.* the frequencies are definitely not in the 1.5 ratio.

It has been already noted in Section 1.4 that the global frequency–frequency correlation (the *'Bursa line'*) is in fact formed by a number of individual lines, *i.e.* that the coefficients A, B of the linear relation

$$\nu_U = A\,\nu_L + B\,, \tag{1.4}$$

are slightly different for each individual source. In this section, we examine the frequency–frequency correlations separately for eleven neutron star sources (seven atoll + four Z sources; listed in Table 1.3) by fitting each of them with the linear formula (1.4), where the coefficients A and B are hereafter referred to as the slope and the shift, respectively.

Two different sets of frequency data are used for the analysis. One is the set that has already been used in the previous section, which contains collected frequency pairs obtained using different methods and published in the literature by various authors in 1996 − 2002 (hereafter data set 1). This set contains six atoll sources: 4U 0614+09, 4U 1608−52, 4U 1636−53, 4U 1702−43, 4U 1728−34, 4U 1735−44; and four Z sources: GX 5−1, GX 17+2, GX 340+0, Sco X−1. The second set, kindly provided by D. Barret, was extracted directly from all science event files available in the *RXTE* archives up to the end of 2004 (hereafter data set 2). The raw event files were consistently analysed using a method, which is described in Appendix D, and therefore frequency pairs obtained in this way represent a very coherent set of data. The set contains six atoll sources: 4U 0614+09, 4U 1608−52, 4U 1636−53, 4U 1728−34, 4U 1735−44 and 4U 1820−30.

The results of the linear regression analysis of the frequency data, including values of the slope and shift and of the corresponding errors for each source, are summarized in Table 1.3 and plotted in Figure 1.13 showing the slope–shift plane. The dependence $A = A(B)$ strongly suggests that the two quantities are anti-correlated and obey a general relation

$$A = \alpha - \beta\,B\,. \tag{1.5}$$

The best linear fits for the anti-correlation give

$$\alpha = (1.44 \pm 0.09), \quad \beta = (1.49 \pm 0.20) \times 10^{-3}\ \mathrm{Hz}^{-1} \qquad \text{(data set 1)}, \tag{1.6a}$$

$$\alpha = (1.46 \pm 0.10), \quad \beta = (1.48 \pm 0.20) \times 10^{-3}\ \mathrm{Hz}^{-1} \qquad \text{(data set 2)}. \tag{1.6b}$$

The anti-correlation law that we have just discovered is very robust. Sources fairly closely follow the anti-correlation line with the typical value of the reduced χ^2 being about 0.77 for both data sets. That means that intersections of their individual frequency–frequency linear fits (individual *'Bursa lines'*) cluster near a single point, $[N_L, N_U]$, whose coordinates may be determined from the coefficients α, β of the anti-correlation (1.5),

$$N_L = \frac{1}{\beta} = (976 \pm 203)\ \mathrm{Hz}\ , \tag{1.7a}$$

$$N_U = \frac{\alpha}{\beta} = (673 \pm 93)\ \mathrm{Hz}\ . \tag{1.7b}$$

The existence of the common intersection point and its position immediately bring into relevance the idea that there is a similar mechanism for HFQPOs at work in both neutron stars and black holes. That is, the ratio N_U/N_L equals to 1.5 with the accuracy of 3% and the intersection point lies almost on the black-hole 3/2 line (Figure 1.3; *red* line). This suggest that the 3 : 2 ratio known from microquasars may also be relevant for the neutron-star kHz QPOs. Indeed, Abramowicz, Bulik, Bursa & Kluźniak (2003) showed that the distribution of frequency ratios has a significant excess near the value 1.5 in neutron stars. Their findings were later challenged by Belloni *et al.* (2005), who obtained similar results and in addition found that the distribution is in fact multi-peaked with 1.5 being the dominant ratio.

If the connection between the neutron-star and black-hole QPOs is real, as we will hereafter assume to be so, then the intersection point should lie exactly on the 3/2 line and the anti-correlation law (1.5) should be rephrased to the form

$$A = \frac{3}{2} - \frac{1}{\nu_L^\circ}\, B\ , \tag{1.8}$$

where ν_L° represents here the lower *'eigenfrequency'* of the source, *i.e.* the point, where the source line crosses the 3/2 line in the Bursa plot. The best fit to the data gives

$$\nu_L^\circ = (628 \pm 47)\ \mathrm{Hz} \qquad \text{(data set 1)}, \tag{1.9a}$$

$$\nu_L^\circ = (629 \pm 17)\ \mathrm{Hz} \qquad \text{(data set 2)}. \tag{1.9b}$$

Similarly to black holes, we may expect that ν_L° is related to the mass of the source and that the black-hole inverse mass scaling law (Section 1.3) is also applicable to neutron stars. The fact that the individual positions of sources in the A–B plane do not strictly follow the anti-correlation line (1.6a,b) can then be attributed to small diversities in neutron-star masses. If we consider two sources with slightly different masses, in the slope–shift plane they would lie at proximate lines with a common vertex at $[0, 1.5]$, although their exact positions on these lines could be arbitrary. Neutron stars are expected to have masses in a narrow range $\sim 1.5 - 3\, M_\odot$, hence the mass lines would be rather close to one another in the A–B plane, as well as the crossings of source lines with the 3/2 black-hole line in the

Source	type	ν_L range [Hz]	A	ΔA	B [Hz]	ΔB [Hz]	references
4U 0614+09	A	150– 830	0.99	0.03	330	17	[9,10,11]
4U 1608−52	A	440– 870	0.81	0.04	415	26	[5,9,12]
4U 1636−53	A	640– 950	0.65	0.04	563	30	[5,6,9]
4U 1702−43	A	650– 770	0.74	0.05	521	38	[9]
4U 1728−34	A	510– 880	0.94	0.05	350	38	[1,5,11]
4U 1735−44	A	630– 900	0.64	0.05	569	32	[2,9]
GX 5−1	Z	150– 630	0.83	0.04	386	14	[4,7]
GX 17+2	Z	470– 830	0.86	0.04	364	28	[3]
GX 340+0	Z	190– 570	0.84	0.07	391	26	[4,9]
Sco X−1	Z	560– 850	0.73	0.01	470	7	[8]
BEST FIT	$A = (1.44 \pm 0.09) - (1.49 \pm 0.20) \times 10^{-3}$ Hz^{-1}					$(\chi^2/\text{d.o.f.} = 0.767)$	
4U 0614+09	A	570– 780	1.02	0.03	302	23	[13]
4U 1608−52	A	560– 920	0.75	0.03	459	17	[13]
4U 1636−53	A	550– 940	0.72	0.01	503	8	[13]
4U 1728−34	A	660– 850	1.00	0.05	352	40	[13]
4U 1735−44	A	710– 840	0.90	0.07	372	56	[13]
4U 1820−30	A	680– 820	0.93	0.05	323	36	[13]
BEST FIT	$A = (1.46 \pm 0.10) - (1.48 \pm 0.20) \times 10^{-3}$ Hz^{-1}					$(\chi^2/\text{d.o.f.} = 0.763)$	

TABLE 1.3: Characterictics of ν_U–ν_L frequency correlations of individual sources (atoll and Z) and coefficients of their linear fits. Top part lists data collected from various papers published in the period 1996–2002 (data set 1; see references below). Bottom part lists a coherent set of data provided by D. Barret (data set 2). The best linear fits $A(B)$ corresponding to the two sets are also indicated.
References: [1] Di Salvo *et al.* (2001), [2] Ford *et al.* (1998), [3] Homan *et al.* (2002), [4] Jonker *et al.* (2000a), [5] Jonker *et al.* (2000b), [6] Jonker *et al.* (2002a), [7] Jonker *et al.* (2002b), [8] van der Klis *et al.* (1997), [9] van der Klis (2000), [10] van Straaten *et al.* (2000), [11] van Straaten *et al.* (2002), [12] van Straaten *et al.* (2003), [13] data by D. Barret to appear in Abramowicz *et al.* (2006).

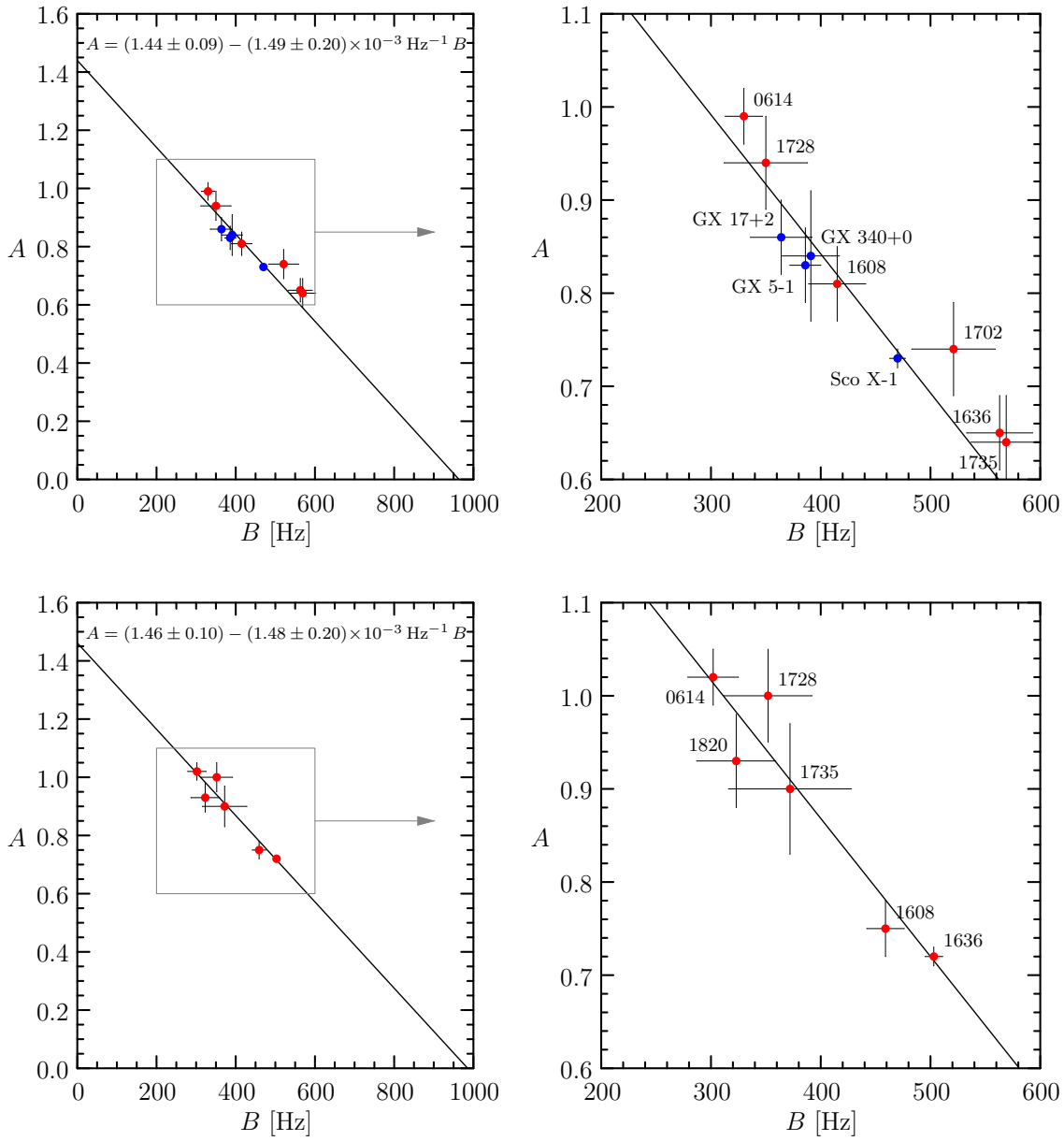

FIGURE 1.13: The anticorrelation between the slope and shift in neutron-star sources. The results of analysis of the two different sets of data, are presented respectively in the *top* (data set 1) and *bottom* (data set 2) pair of panels. Atoll sources are ploted in *red*, Z sources are ploted in *blue*. The shift A and the slope B correspond to the best linear fit of the ν_U–ν_L correlation for each source. Clearly, A and B are anticorrelated among the sources with the best fits indicated by the *solid line* in each panel. The fits cross the vertical slope axis very close to 1.5, which points to the connection with the black-hole HFQPOs.

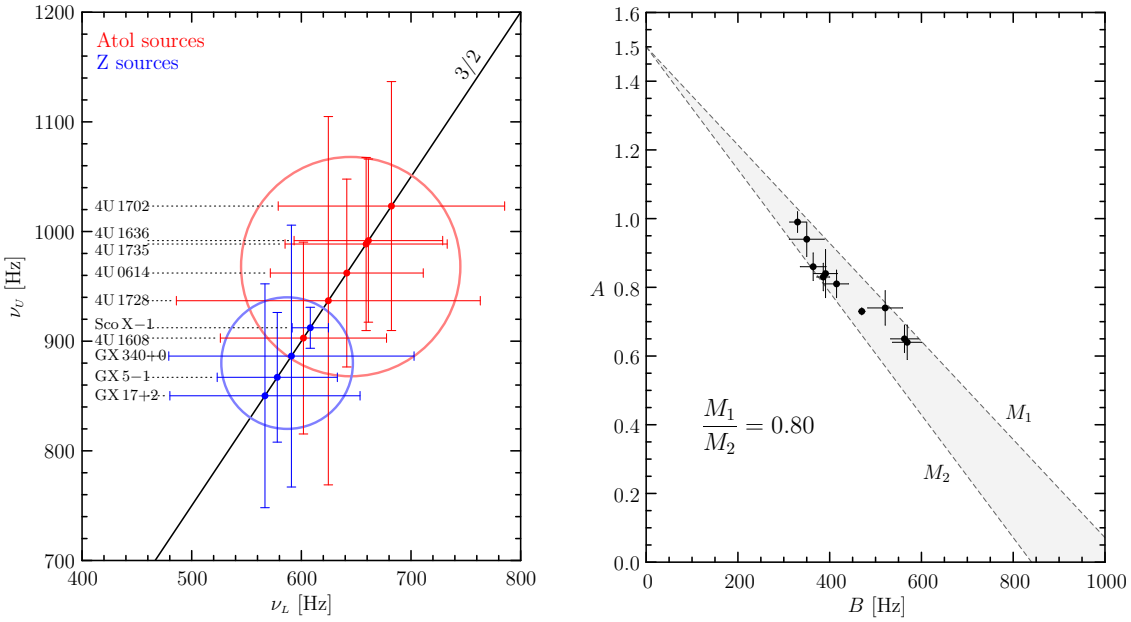

FIGURE 1.14a: Intersection points of the frequency correlations in individual neutron-star sources with the black-hole 3/2 line. All source lines intersect the 3/2 line near the point $[942, \nu_L^\circ{=}628]$, but Z sources prefer somewhat lower and atoll sources somewhat higher values of ν_L°. This suggests that Z sources may have larger masses than atoll sources by a factor of $\sim$10%.

FIGURE 1.14b: The anti-correlation and the effect of the inverse mass scaling law. The slopes and shifts of the frequency correlations are such that they all fall in a narrow triangle in the A–B plane with the vertex at $[0, 1.5]$. The opening angle of the triangle corresponds to the ratio of masses between the lightest and the heaviest neutron star.

frequency–frequency plot. By scaling the ν_L° parameter of equation (1.8), we find that the $A(B)$ relation is steeper or softer for more massive or less massive sources, respectively. This is demonstrated in Figure 1.14b. The range in eigenfrequencies among the examined sources is about 200 Hz, which offers a suggestion that their masses do not differ more than by 20%. If we know the mass of some source with a reasonably small error, we will be able to precisely determine also masses of the others, but for the moment only relative comparisons can be made.

There is a certain trend for Z sources to have a slightly lower values of A than atoll sources for the same values of B (see Figure 1.13). It is even more evident if we calculate positions of the intersection points for each source. Figure 1.14a shows, where the source lines of six atoll and four Z sources cross the 3/2 black-hole line. Clearly, Z sources have lower eigenfrequencies than atoll sources by $\sim$10% and should therefore be (on average) by a similar factor more massive than atolls.

In the above considerations we have, nevertheless, disrespected the presence of magnetic fields around neutron stars, which is probably one of the differences between the Z

and atoll sources. Accreting low-mass X-ray binaries are believed to have magnetic field generally $\lesssim 10^{10}$ Gauss, because stronger field would destroy the accretion disc far from the star, but the actual proportions in the field strengths of the two types of sources is unknown. It was thought that atoll sources had weaker field than Z sources by a factor of ten. This claim was supported by the presence of low-frequency HBO oscillations in Z sources (Alpar & Shaham 1985; Shibazaki & Lamb 1987) and by a paradigm about the mutual exclusion between pulsations and type I X-ray bursts, which exclusively occur in atoll sources (*e.g.* Lewin *et al.* 1993). Since the discovery of millisecond pulsations in the thermonuclear burster SAX J1808.4−3658 (Wijnands & van der Klis 1998), this supposition is no longer true, because apparently atoll sources can have relatively strong magnetic field and be pulsars, too.

CHAPTER 2

Constraints on resonance models of QPOs from black-hole spin estimates

The spectral and timing X-ray observations of Galactic black-hole binary systems provide us with information about physical processes that occur in accretion discs near black hole event horizons. One of the main goals of these studies is to obtain constraints on black hole masses and spins using predictions of general relativity in the regime of strong gravity.

The masses of about 20 accreting black holes located in X-ray binary sources have been determined by measurements of radial velocities from the Doppler shift of absorption lines in optical spectra of the secondary components (McClintock & Remillard 2005; Casares *et al.* 2004; Orosz *et al.* 2004). However, the number of reliable measurements of black-hole spins is significantly lower (*e.g.* Miniutti *et al.* 2004; Davis *et al.* 2005). There are three different approaches used to measure the spin of an accreting black hole: by fitting relativistically broadened iron K-alpha lines, by fitting spectral continua, and by searching for high-frequency quasi-periodic oscillations. The last method would be clean and the most accurate, if we knew what exactly excites the oscillations. Because we do not yet, we may by then put to use the other two methods to find out *what actually does oscillate*.

The first section of this Chapter reviews the idea of high-frequency QPOs as a non-linear resonance phenomenon and lists a class of models that have been proposed as a possible resonance modes, which excite the QPOs in the Galactic black-hole and neutron-star sources. The next section summarises predictions for the spins of three microquasars given by each of the resonance models. In the third Section, the spin predictions given by these models are compared with the recent angular momentum estimate for GRO J1655−40. It is found that none of the present resonance models is consistent with the value of the spin obtained by spectral fits of the X-ray continuum. Instead, observational constraints seem to favour another, so far not considered resonance, which is described in the last section. This Chapter is based on a paper in preparation (Bursa 2006).

2.1 High-frequency QPOs as a non-linear resonance

Observations of the twin HFQPOs are now well established in both neutron-star and black-hole binary sources. They have revealed to our attention many similarities as well as plenty of differences in these two types of objects. In neutron stars, HFQPO frequencies wander in time by tens of Hertz, but their ratio clusters mainly around 3/2. The frequencies follow a single special line in detections collected from *all* sources, while the slope and shift of the linear correlation is slightly different for each source. There exists an anti-correlation between the slope and the shift, which picks up the 3/2 value with an astonishing precision. In black holes, the frequencies stay fixed or vary only a little. They always occur in the 3 : 2 ratio and they seem to scale inversely with mass.

All this and other previously discussed evidence offer a strong encouragement for seeking interpretations of HFQPOs in fundamental features of strong gravity, namely in the orbital and epicyclic motion of fluid elements in accretion discs. The rational ratios of the frequencies originally lead Kluźniak & Abramowicz (2001) to a formulation of a resonance model for HFQPOs. In this model (see a recent review in Abramowicz & Kluźniak 2004b and a collection of review articles, edited by Abramowicz 2005b, that describe the model), a non-linear coupling in the motion of accreting fluid is made responsible for the twin QPOs. At particular radii in the disc, commensurabilities between certain combinations of epicyclic and orbital frequencies can lead to an excitement of a parametric-like or a forced-like resonance between the particular types of motion. In this way, general relativity itself picks up certain frequencies from the disc regardless of the properties of the source.

Unlike Newtonian $1/r$ gravity, general relativity predicts independent frequencies for different types of periodic motion in the strong gravitational field of a rotating compact object (Nowak & Lehr 1998; Merloni *et al.* 1999). The condition $\nu_K > \nu_z > \nu_r$ is always satisfied for the Keplerian orbital, vertical epicyclic and radial epicyclic frequencies, respectively. The radial epicyclic frequency ν_r reaches a maximum at a particular radius and goes to zero at the marginally stable circular orbit. This allows for two of the three frequencies (or a combination) to be in a ratio of small natural numbers somewhere in the disc.

A whole class of relativistic resonance models has been be constructed with different combinations of frequencies (see *e.g.* Abramowicz & Kluźniak (2004b); Abramowicz *et al.* (2004) for a detailed description of possible models). The most natural is the parametric resonance between the vertical and radial epicyclic frequency: $\nu_U = \nu_z$, $\nu_L = \nu_r$, $2\nu_z = 3\nu_r$ (3:2 resonance). Another possibility is a forced resonance between the epicyclic modes, which gives two solutions: $\nu_U = \nu_z$, $\nu_L = \nu_z - \nu_r$, $\nu_z = 3\nu_r$ (3:1 resonance) and $\nu_U = \nu_z + \nu_r$, $\nu_L = \nu_z$, $\nu_z = 2\nu_r$ (2:1 resonance). Finally, models with coupling between the orbital Keplerian motion and the radial epicyclic motion can be considered: $\nu_U = \nu_K$, $\nu_L = \nu_r$, $2\nu_K = 3\nu_r$ (Keplerian 3:2 resonance); $\nu_U = \nu_K$, $\nu_L = \nu_K - \nu_r$, $\nu_K = 3\nu_r$ (Keplerian 3:1 resonance) and $\nu_U = \nu_K + \nu_r$, $\nu_L = \nu_K$, $\nu_K = 2\nu_r$ (Keplerian 2:1 resonance).

A parametric-like resonance occurs in a multi-component system, where one part of the system parametrically excites another part (*e.g.* Tondl *et al.* 2000). The primary system

oscillates due to external or parametric excitations or due to self-excitation, and excites the other subsystems. If certain conditions are met, one of these subsystems may in turn further excite the primary system. The classical example of auto-parametric resonance is that of the elastic pendulum consisting of a spring fixed at one end. A parametric resonance in a system, whose eigenfrequency ω_1 is itself perturbed at a frequency ω_2 commensurate with ω_1, leads to the Mathieu type of equation

$$\delta\ddot{x} + \omega_1^2 \left[1 + h\cos(\omega_2 t)\right] \delta x = 0 \,, \tag{2.1}$$

where $h\cos(\omega_2 t)$ term acts as an 'energy' source and is said to parametrically excite the system. Resonances occur when $\omega_1/\omega_2 = 2/n$, $n = 1, 2, 3, \ldots$ and the strongest one has the smallest possible value of n. In thin discs, random fluctuations have generally greater radial than vertical amplitudes and therefore the radial epicyclic frequency plays the role of the perturbing frequency to the vertical epicyclic frequency. Because in strong gravity $\nu_r < \nu_z$, the smallest possible value of n for a resonance is $n=3$, which means that $\nu_z : \nu_r = 3 : 2$. The radius, where the two epicyclic frequencies of freely moving particles are in the $3:2$ ratio, is $10.8\,r_{\rm g}$ for a non-rotating black hole and gets as close as to $4\,r_{\rm g}$ with an increasing spin.

A forced resonance occurs in a system, which is perturbed by a periodic external force,

$$\delta\ddot{x} + \omega_1^2\,\delta x + \text{damping} = h\cos(\omega_2 t) \,. \tag{2.2}$$

In a damped harmonic oscillator, amplitudes gradually decay to zero. When it is driven by a periodic force, one oscillation survives and the system oscillates not with its eigenfre-

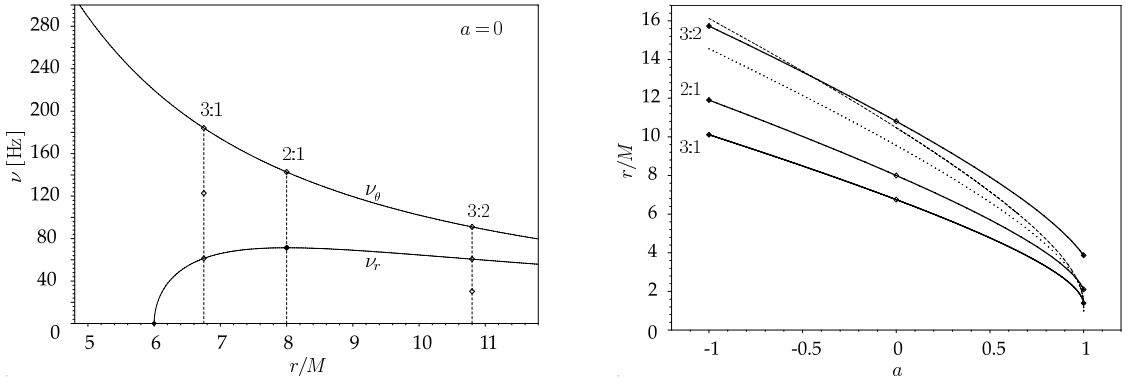

FIGURE 2.1: *Left:* Locations of the three resonances: the 3:2 parametric, and 2:1 and 3:1 forced for Schwarzschild case of a non-rotating $10\,M_\odot$ black hole. *Right:* These locations depending on the black hole spin. Also shown is the radius (*dotted line*), at which the standard relativistic Shakura-Sunyaev disc emits locally the maximal flux, and the radius (*dashed line*) corresponding to the pressure centre of the maximally thick torus, *i.e.* the torus with constant angular momentum equal to the Keplerian value at marginally bound orbit. (Adopted from Abramowicz *et al.* 2004.)

Resonance		XTE 1550−564	GRO J1655−40	GRS 1915+105
$[\nu_z, \nu_r]$:	3 : 2	+0.89 — +0.99	+0.96 — +0.99	+0.69 — +0.99
	2 : 1	+0.12 — +0.42	+0.31 — +0.42	−0.41 — +0.44
	3 : 1	+0.32 — +0.59	+0.50 — +0.59	−0.15 — +0.61
$[\nu_K, \nu_r]$:	3 : 2	—	—	+0.79 — +1.0
	2 : 1	+0.12 — +0.43	+0.31 — +0.42	−0.41 — +0.44
	3 : 1	+0.29 — +0.54	+0.45 — +0.53	−0.13 — +0.55

TABLE 2.1: Summary of angular momentum estimates as they are predicted by different resonance models for the three microquasars with known masses. The uncertainty in the spin estimates is due to uncertainties in the black-hole mass measurements. (Adopted from Török 2005b.)

quency ω_1 but with the frequency ω_2 of the periodic force. The amplitude of oscillations depends on the driving frequency. It has its maximum when the driving frequency matches the eigenfrequency and a resonance occur. In that case $\omega_1 = n\,\omega_2$ as observed. Obviously, there is not any integer value n such that ω_1, ω_2 could be in the 3 : 2 ratio. However, combination frequencies $\nu_z + \nu_r$ and $\nu_z - \nu_r$ can be in resonance with the radial epicyclic frequency in the disc if $n = 2$ or $n = 3$.

Non-linear effects in the two types of oscillators are important. Both the dependency of the eigenfrequency of the non-linear oscillator on the amplitude and the non-harmonicity of the oscillation lead to a behaviour that evoke parallels with the behaviour of the high-frequency QPOs in neutron stars and black holes.

2.2 Black hole spin predictions

For each resonance model Török *et al.* (2005) have made fits to the observational data for the three microquasars with known masses (XTE 1550−564, GRO J1655−40 and GRS 1915+105) in order to predict values of their spins. They compare the observed upper HFQPO frequency of each source with frequencies predicted by individual models at particular resonant radii. Based on the knowledge of mass of the sources they calculate the range for the black hole angular momentum required by each model to work. Their results are summarised in Table 2.1.

The observational data already excludes the Keplerian 3:2 resonance in the case of two sources, as it requires spins $a > 1$. If it is assumed that the HFQPOs are produced by the same type of resonance in all black-hole sources, then this model can be ruled out as incompatible with observations. Other models discussed by Török *et al.* are so far consistent with measured masses, but as they note, future observations or developments in accretion theory can narrow down the choice. In this context, direct measurements of black-hole spins may be especially useful to limit the number of possibilities further.

2.3 The spin of GRO J1655−40 and implications for resonance models

Shafee *et al.* (2005) have recently published an analysis of X-ray spectral data from *ASCA* and *RXTE* of the two black hole candidates, GRO J1655−40 and 4U 1543−47, where they estimate the angular momenta of these sources. Here, GRO J1655−40 (hereafter J1655) is of a high interest, because it also shows the twin HFQPOs.

Their analysis is based on fitting the X-ray thermal continuum spectra using a fully relativistic model of a thin accretion disc around a Kerr black hole (Li *et al.* 2005). The model includes all relativistic effects as well as self-irradiation of the disc, limb-darkening effects and the spectral hardening factor. It, however, strongly relies on the assumed value of the spectral hardening factor, which cannot be obtained from the data and must be estimated independently. The state-of-the-art non-LTE disc atmosphere model of Davis *et al.* (2005) is used to estimate the factor.

The spin of J1655, according to Shafee *et al.*, is $a \simeq 0.65 - 0.75$. Facing this estimated value, *none* of the predictions of the 'basic' six resonance models (3:2, 2:1 3:1; Table 2.1), neither the models with 'higher' resonances 5:1, 5:2, 5:3 (Török *et al.* 2005) give the angular momentum of J1655 to be compatible with the spin measurement. They predict spins either too high (>0.96) or too low (<0.6). The one with the closest approach is the 3:1 forced resonance, which predicts spin in the range $0.50 - 0.59$. This could mean that none of these models in their current formulations is able to explain the origin of HFQPOs in black hole sources. In particular, the parametric resonance $\nu_z : \nu_r$ can be ruled out not only because it predicts very high spins, but also because it gives wrong masses in the $a = 0$ limit. If the QPO mechanism should be the same for both black-hole and neutron-star sources (Kluźniak & Abramowicz 2003), then it can be seen from Figure 2.2 that this resonance gives, in the $a = 0$ limit, mass of the source about $2\,M_\odot$ for QPO frequencies of J1655, *i.e.* 300 and 450 Hertz. Neutron stars have frequencies typically two times higher than that, so their masses would be two times less according to the $1/M$ scaling – about $1\,M_\odot$, which is too low for a neutron star.

Possible combinations of mass and spin for the frequencies seen in J1655 are shown in Figure 2.2. It shows the predictions of the standard resonance models as well as the prediction of the $\nu_z : \nu_K - \nu_r$ resonance, which is discussed in the next section.

Although the spectral fitting has been done very carefully, it has some weak points. The assumed value of the spectral hardening factor is one of them. Next, the analysis assumes that the disc terminates at the marginally stable orbit in the thermal dominant state and that it has zero torque at the inner edge. Relaxing these conditions leads to lower spin estimates, as well as considering effects of magnetic fields on the emergent spectrum. The only effect, which softens the spectrum and gives higher black-hole spins, is the presence of density inhomogeneities in the inner region of the disc created by MRI turbulences and by photon bubbles. Shafee *et al.* also note that a black hole in an X-ray binary may accrete at most $1\,M_\odot$ during the lifetime of the system, which leads to the spin $\lesssim 0.35$. If so and if measured spin is ~ 0.7, the black hole had to be born with some

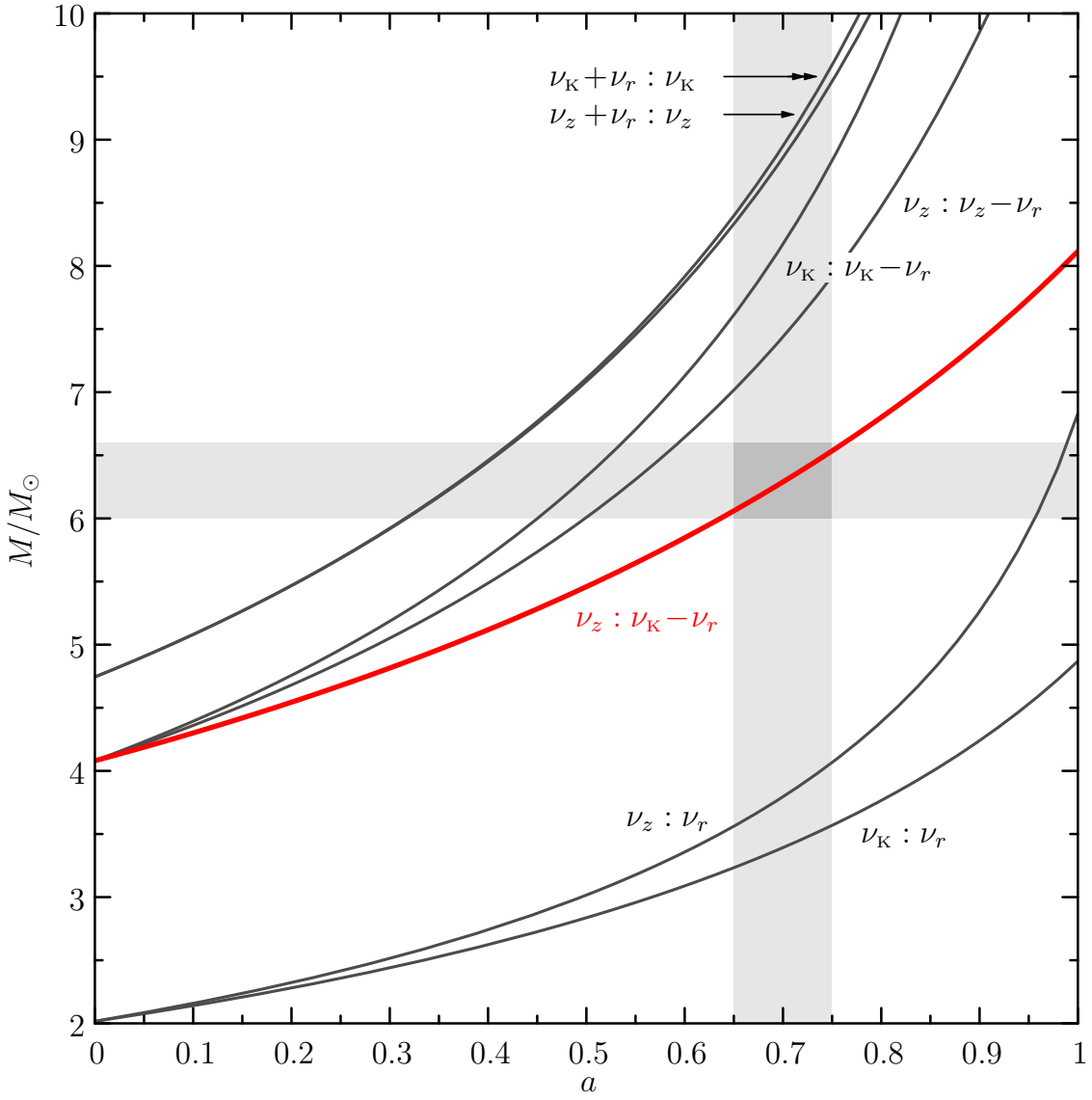

FIGURE 2.2: Possible combinations of mass and angular momentum predicted by individual resonance models for the HFQPO frequencies observed from GRO J1655−40. Thin lines represent predictions of the 3:2, 3:1 and 2:1 resonances. The thick red line shows the prediction of the $\nu_z : \nu_{\rm K}-\nu_r$ resonance. Shaded regions indicate the likely ranges for the mass of J1655 (inferred from optical measurements of radial curves) and its dimensionless angular momentum parameter a (inferred from the X-ray spectral data fitting).

initial amount of angular momentum. It is then questionable, whether its rotational axis is aligned with the rotational axis of the binary system as it is assumed in the model (see Maccarone 2002), and it brings an inclination uncertainty to the spectral fitting. Improved disc atmosphere models will probably change the estimated value of the spin, but probably not very significantly. Namely, the possibility of having the black hole spun-up to $a > 0.9$ seems to be very unlikely.

It is also important to stress that the spin predictions of resonance models are based on the formulae of the epicyclic motion of free test particles in a gravitational field. In general, because of pressure gradient, magnetic and other forces, these frequencies will be subjects of some corrections (Blaes *et al.* 2006), which may change the positions of the resonance lines in the mass–spin plot.

In the light of the previously described effects, it is still possible that some of the resonances can stay in the game. The closest one is the $\nu_K : \nu_K - \nu_r$ resonance, which may fit the measured value of the spin, if improved disc atmosphere models indeed lower its estimate or if frequency corrections move the resonance radius closer to the black hole.

2.4 Resonances in an eccentric torus

If a resonance is about to be a mechanism for producing the QPOs, one may, interestingly, contemplate a new model to satisfy the observational evidence, which has not been considered so far: the resonance between the vertical epicyclic frequency ν_z and the periastron precession frequency $\nu_{\mathrm{PP}} = \nu_K - \nu_r$. These two frequencies are in the 3:2 ratio very near the marginally stable orbit (Figure 2.3). For a black hole with spin $a = 0.75$ it occurs around $r = 4.3\,r_{\mathrm{g}}$, while marginally stable orbit is at $r_{\mathrm{ms}} = 3.16\,r_{\mathrm{g}}$. The occurrence of HFQPOs may then correspond to a formation of a slightly eccentric fluid torus at the inner edge of the accretion disc. It will be shown in Chapter 4 that relativistic effects on light propagation may be responsible for a sufficient modulation of the radiation emerging from the torus.

There are, however, some issues, which make this type of resonance objectionable. It is namely the fact that frequencies of the orbital motion and the frequencies of the two modes of epicyclic motion differ from one another in an axially symmetric spacetime of a rotating black hole. This imposes a very general restriction on a modulation mechanism of quasi-periodic oscillations:

If all three modes of a particle motion are involved in a resonance and some linear combination of the three frequencies forms a rational ratio, then a modulation mechanism must not add any other frequency to the combination, otherwise the observed frequencies would not be commensurable.

In another words it means that the frequencies in the resonance must be the same frequencies that are observed.

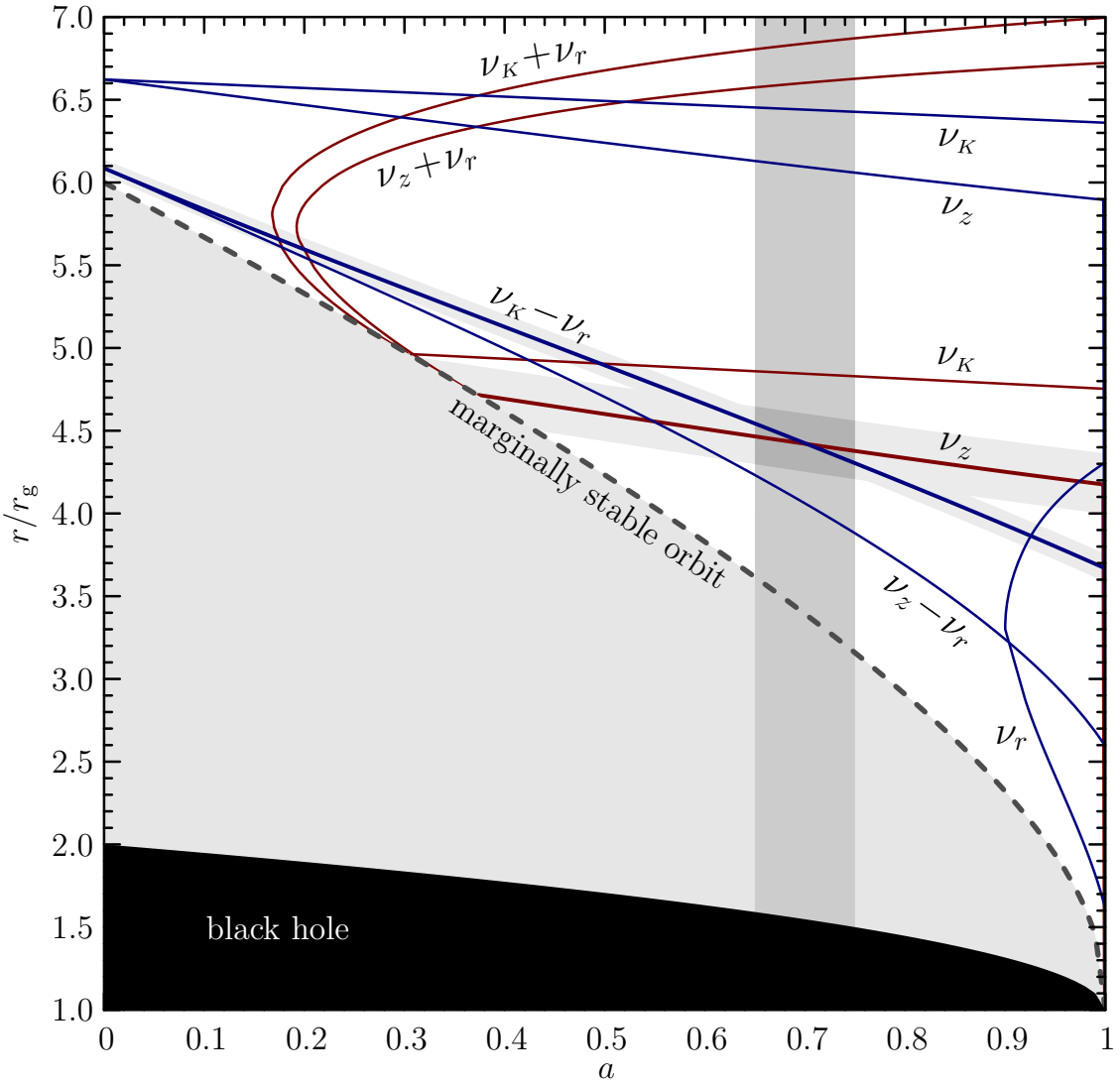

FIGURE 2.3: This plot shows, where the frequencies of different modes of orbital motion (or their combinations) are equal to those observed in GRO J1655−40, *i.e.* 450 Hz (*red lines*) and 300 Hz (*blue lines*). A resonance is possible at every radius, where a red line crosses a blue one. The *gray* vertical bar represents the estimated range of spin of the black hole in J1655. The *light gray* shading of lines shows the radius uncertainty based on the uncertainty of mass estimate for the black hole (only for ν_z and $\nu_K-\nu_r$) . The only combination of frequencies, which satisfies observational constraints, is the resonance between ν_z and $\nu_K-\nu_r$.

Source	Measured mass[(a)] $[M_\odot]$	Measured spin	Predicted spin
XTE 1550−564	8.4 — 10.8	—	0.41 — 0.77
GRO 1655−40	6.0 — 6.6	0.65 — 0.75	0.64 — 0.76
GRS 1915+105	10 — 18	—	−0.09 — 0.78

TABLE 2.2: Summary of the predictions of angular momentum as they are given by the $\nu_z : \nu_K$–ν_r resonance for the three microquasars with known masses. The ranges in the spin predictions correspond to the uncertainties in the black-hole mass measurements.
[(a)] See Orosz *et al.* 2002, Greene *et al.* 2001, Greiner *et al.* 2001

An eccentric torus, in which fluid elements oscillate radially with frequency ν_r, makes a precession of apsides with frequency $\nu_{\rm PP}$. The latter one is also the frequency at which the outgoing flux will be modulated by the Doppler effect. There are two possibilities for an occurrence of QPOs by the $\nu_z : \nu_{\rm PP}$ resonance: either radial oscillations are coupled with ν_z or ν_K, but then the observed $\nu_{\rm PP}$ will not generally form a rational ratio with ν_z, or there is a direct resonance between ν_z and $\nu_{\rm PP}$, but in this case it is unclear what physical mechanism would couple these modes and keep them in the 3:2 ratio.

The relevance of the $\nu_z : \nu_{\rm PP}$ resonance can be tested by estimating spins of the other two microquasars with known masses, which show high-frequency QPOs. We have seen that the model predicts the spin of J1655 to be $a = 0.64 - 0.76$, which is an excellent match with the estimated value $0.65 - 0.75$. For the other two microquasars, the model predicts spins to be in the range $0.41 - 0.77$ for XTE 1550−564 and $-0.09 - 0.78$ for GRS 1915+105 (see these result summarised in Table 2.2). Unfortunately, current knowledge of their distances and large errors in mass measurements do not allow to accurately use the spectral fitting method to constrain the angular momenta of those black holes.

CHAPTER 3

Oscillating torus as a modulation mechanism for black-hole HFQPOs

The second important aspect of quasi-periodic oscillations, beside knowing what oscillates, is a modulation mechanism of the emergent flux. Even if we know what oscillates, there has to be a mechanism that periodically modulates the outgoing radiation by several percent of the mean. It has been found out that in neutron-star sources, where QPO oscillations are strong and it is possible to have a high signal to noise ratio and a sufficiently high count-rates, the HFQPOs originate in the boundary layer, *i.e.* the actual luminosity modulation takes place on the neutron star surface (Gilfanov *et al.* 2003; Gilfanov & Revnivtsev 2005). That suggests that the mechanism of QPOs periodically enhances the feed of material onto the star, which burns when it hits the surface and intensify the radiation production.

Such kind of modulation cannot work in black-hole sources, because most of matter is disappearing under the horizon. It is likely that the absence of the solid surface is the reason why QPOs are much weaker in black holes than in neutron stars – we are perhaps lucky to observe the actual process not outshined by any of its consequent effects.

Observations show that the solely presence of a thin accretion disc is not sufficient to produce the HFQPO oscillations, because they are exclusively connected to the spectral state, where the energy spectrum is dominated by a steep power law with some weak thermal disc component. A model is more appropriate, where an outer cool disc is continuously transitioned into or sandwiched by a hot, thick, but optically thin flow (Esin *et al.* 1998). An optically thin advection–dominated accretion flow (ADAF; see a review by Narayan *et al.* 1998) is mostly transparent for photons, and therefore general relativistic light bending and lensing effects may gain a particular importance. Significant temporal variations in the observed flux can then be accomplished by global oscillations of such geometrically thick flow, fluid tori.

In order to explore, whether it is possible to obtain some flux modulation just by effects of strong gravity, we set up a model of a possible accretion configuration, largely simplified to a presence of a hot and optically thin luminous torus, optionally surrounded by a cool opaque disc. The torus is considered in a *'slender approximation'*, *i.e.* with its size being smaller as compared to its distance from the gravity centre. Later on, in an astrophysically realistic model, the optically thin medium can represent a scattering corona or a diluted advection dominated flow, in which additional processes of local microphysics play a more complicated role.

The idea of a slender torus was initially invented by Madej & Paczyński (1977) in their model of an accretion disc of the dwarf nova U Geminorum. They noticed that in the slender limit and in the Newtonian gravity, the surfaces of constant effective potential form concentric circles. The same idea of slender torus in a form of a 'thin isothermal ring' was then used by Papaloizou & Pringle (1984, 1985) in their remarkable papers about the stability of non-self-gravitating polytropic tori. The additional symmetry induced by the Newtonian potential was employed by Blaes (1985), who found a complete set of normal mode solutions with an analytic description of all eigenfunctions and eigenfrequencies for the linear perturbations of polytropic tori with constant specific angular momentum.

It has been proved recently both in general Newtonian theory (with a non-spherically symmetric potential, Blaes *et al.* 2006) and in Einstein relativity (Abramowicz *et al.* 2005c) that *in an axially symmetric stationary spacetime, a toroidal distribution of a perfect fluid in equilibrium always admits global epicyclic eigenmodes of oscillations.* In particular they have shown that in the slender limit (which corresponds to the sound speed $c_{\rm s}=0$) there exist rigid and axisymmetric ($m=0$) modes between possible solutions of the non-relativistic and relativistic versions of the Papaloizu-Pringle equation. These modes represent the simplest global and always-present oscillations in an accretion flow, axisymmetric up–down and in–out motion. The oscillations are sinusoidal, with frequencies equal to the meridional and radial epicyclic frequencies.

In this Chapter we first briefly summarise the basic equations of the theory of geometrically thick accretion discs and review the calculations of epicyclic oscillations of a slender torus by Blaes (1985) and Abramowicz *et al.* (2005c). Then we setup a simple model of a torus filled with an optically thin gas and describe its thermodynamical and radiative properties. This model serves as a source of radiation for the numerical ray-tracing code, which is used to transport radiation emitted locally in the torus to an observer at infinity through the curved spacetime. The last section describes some technical details of numerical ray-tracing and postprocessing of calculated lightcurves. This Chapter is based on work published in Bursa (2004).

3.1 Relativistic tori in accretion flows

Thick non-Keplerian accretion discs (tori) are likely to be present in many astrophysical objects, *e.g.* quasars and other active galactic nuclei, in X-ray binaries and microquasars, and likely also in the central engine of gamma-ray bursts. In particular, it is well known (Abramowicz *et al.* 1978) that in a system formed by a black hole surrounded by a thick disc, the gas flows in an effective (gravitational plus centrifugal) potential, whose structure is comparable with that of a close binary. The pressure gradients balance the gravitational and centrifugal forces, allowing for the existence of stationary configurations of matter in a non-geodesic circular motion and contained within closed constant pressure equipotential surfaces. The Roche torus encompassing the black hole has a cusp-like inner edge located at the Lagrange point L1, where mass transfer driven by the radial pressure gradient is possible.

In the following, we derive main equations for standard geometrically thick accretion discs using an elegant Killing-vector notation (see also Fishbone & Moncrief 1976, Abramowicz *et al.* 1978, Kozlowski *et al.* 1978, Kuwahara 1988 and references therein).

Euler equation

The geometry of an exterior spacetime surrounding static a star or black hole of mass M is in the standard coordinate system $(t,\, r,\, \theta,\, \phi)$ described by the Schwarzschild line element

$$\mathrm{d}s^2 = -\left(1-\frac{2\,M}{r}\right)\,\mathrm{d}t^2 + \left(1-\frac{2\,M}{r}\right)^{-1}\,\mathrm{d}r^2 + r^2\,(\,\mathrm{d}\theta^2 + \sin\theta^2\,\mathrm{d}\phi^2)\,, \tag{3.1}$$

where the metric coefficients depend neither on the time coordinate t (stationarity), nor the azimuthal coordinate ϕ (axisymmetricity), which means (Misner, Thorne & Wheeler 1973) that the spacetime contains timelike and azimuthal Killing vector fields, $\eta^\mu = \delta^\mu_t$ and $\xi^\mu = \delta^\mu_\phi$, along which the geometry does not change. If X^μ, Y^μ are two arbitrary Killing vectors, then following identities are satisfied (Misner, Thorne & Wheeler 1973):

$$\nabla_\mu X_\nu + \nabla_\nu X_\mu = 0 \qquad \text{(Killing equation)}\,, \tag{3.2a}$$

$$X^\mu \nabla_\mu Y_\nu = Y^\mu \nabla_\mu X_\nu\,, \tag{3.2b}$$

$$X^\mu \nabla_\mu Y_\nu = -\tfrac{1}{2}\nabla_\mu (XY)\,, \tag{3.2c}$$

where we use the notation $X^\mu Y^\nu g_{\mu\nu} = (XY)$. The metric then takes the form,

$$\mathrm{d}s^2 = (\eta\eta)\,\mathrm{d}t^2 + g_{rr}\,\mathrm{d}r^2 + g_{\theta\theta}\,\mathrm{d}\theta^2 + (\xi\xi)\,\mathrm{d}\phi^2\,. \tag{3.3}$$

The perfect fluid with four-velocity u^μ is described by the usual stress-energy tensor

$$T^{\mu\nu} = (\epsilon + p)\,u^\mu\,u^\nu + p\,g^{\mu\nu}\,, \tag{3.4}$$

where the fluid variables ϵ, p and n (n will become in use later on) are respectively the proper energy density, the isotropic pressure and the particle density. The four-velocity

vector u^μ of the fluid rotating purely in the azimuthal direction around the z axis has the form

$$u^\mu = \left(u^t,\, 0,\, 0,\, u^\phi\right) = u^t \left(\eta^\mu + \Omega\, \xi^\mu\right) , \tag{3.5}$$

where we have introduced the angular velocity $\Omega \equiv u^\phi/u^t$.

The relativistic Euler equation of motion for the perfect fluid is contained in the continuity equation of the stress-energy tensor,

$$\nabla_\mu T^\mu_{\ \nu} = 0 , \tag{3.6}$$

which gives the expression for the 4-acceleration a^μ of the flow,

$$a_\mu = -\frac{\nabla_\mu p}{p+\epsilon} . \tag{3.7}$$

In addition to the energy conservation law (3.6), the divergence of $T^{\mu\nu}$ projected along a Killing vector field X^ν,

$$\nabla_\mu \left(T^\mu_{\ \nu} X^\nu\right) = X^\nu \left(\nabla_\mu T^\mu_{\ \nu}\right) + T^{\mu\nu} \left(\nabla_\mu X_\nu\right) = 0 , \tag{3.8}$$

is also identically zero because of anti-symmetricity of $\nabla_\mu X_\nu$ (3.2a). Substituting (3.4) into (3.8), we obtain

$$u^\mu \nabla_\mu \frac{(p+\epsilon)\,(u^\nu X_\nu)}{n} = 0 , \tag{3.9}$$

where we have used to advantage the conservation law of the baryonic number, $\nabla_\mu(n\, u^\mu) = 0$. Hence, there are two quantities, constants of motion along the fluid lines, corresponding to two Killing vectors, namely the energy

$$\mathscr{E} = -\frac{p+\epsilon}{n}\, u_\mu\, \eta^\mu = -\frac{p+\epsilon}{n}\, u_t \tag{3.10}$$

and the angular momentum

$$\mathscr{L} = \frac{p+\epsilon}{n}\, u_\mu\, \xi^\mu = \frac{p+\epsilon}{n}\, u_\phi \tag{3.11}$$

per baryon (Bardeen 1973; Kozlowski *et al.* 1978). These two quantities then define the specific angular momentum (angular momentum per unit mass)

$$\ell \equiv \frac{\mathscr{L}}{\mathscr{E}} = -\frac{(u\xi)}{(u\eta)} = -\frac{u_\phi}{u_t} , \tag{3.12}$$

which together with angular velocity Ω can be used to describe the fluid motion. Ω and ℓ are related by relation

$$\Omega = -\ell\, \frac{(\eta\eta)}{(\xi\xi)} . \tag{3.13}$$

Now we return back to the Euler equation of motion (3.7) and calculate the a_μ. By definition of 4-acceleration, it is

$$a_\mu \equiv u^\nu \nabla_\nu u_\mu = A^2 \left[\eta^\nu + \Omega\, \xi^\nu\right] \nabla_\nu \left[\eta_\mu + \Omega\, \xi_\mu\right] . \tag{3.14}$$

The value of $A = u^t$ can be found from the normalization of 4-velocity, $u^\mu\, u_\mu = -1$, and with the help of identities (3.2) we get

$$a_\mu = -\frac{1}{2}\, \frac{\nabla_\mu\, (\eta\eta) + \Omega^2\, \nabla_\mu\, (\xi\xi)}{(\eta\eta) + \Omega^2\, (\xi\xi)} . \tag{3.15}$$

A Keplerian, *i.e.* geodesic, motion has $a_\mu = 0$ and in the spherically symmetric spacetime is planar, satisfying the condition

$$\frac{\mathrm{d}g_{tt}}{\mathrm{d}r} + \Omega^2\, \frac{\mathrm{d}g_{\phi\phi}}{\mathrm{d}r} = 0 , \tag{3.16}$$

which integrated gives the well-known third Kepler's law

$$\Omega^2 = \frac{G\, M}{r^3} . \tag{3.17}$$

Equation (3.15) can be rearranged to the form

$$a_\mu = -\frac{1}{2}\, \nabla_\mu \ln \left[(\eta\eta) + \Omega^2\, (\xi\xi)\right] + \frac{1}{2}\, \frac{(\xi\xi)\, \nabla_\mu \Omega^2}{(\eta\eta) + \Omega^2\, (\xi\xi)} . \tag{3.18}$$

The standard definition of the effective potential in a spherically symmetric gravitational filed is

$$\mathcal{U} = -\frac{1}{2} \ln \left(g^{tt} + \ell^2 g^{\phi\phi}\right) . \tag{3.19}$$

The metric components that appear in the formula (3.19) may be invariantly defined in terms of the Killing vectors η^μ and ξ^μ (Abramowicz & Kluźniak 2004a),

$$g^{tt} = e^{-2\Phi} \equiv \frac{1}{(\eta\eta)} , \tag{3.20}$$

$$g^{\phi\phi} = -\frac{1}{\tilde{r}^2}\, e^{-2\Phi} \equiv \frac{1}{(\xi\xi)} , \tag{3.21}$$

where Φ is the gravitational potential and $\tilde{r}$ is the circumferential radius. Then we can substitute (3.19) into (3.18) and write the Euler equation (3.7) in terms of the effective potential $\mathcal{U}$, angular velocity Ω and specific angular momentum ℓ,

$$-\frac{\nabla_\mu p}{p + \epsilon} = \nabla_\mu\, \mathcal{U} - \frac{\Omega \nabla_\mu \ell}{1 - \Omega\, \ell} . \tag{3.22}$$

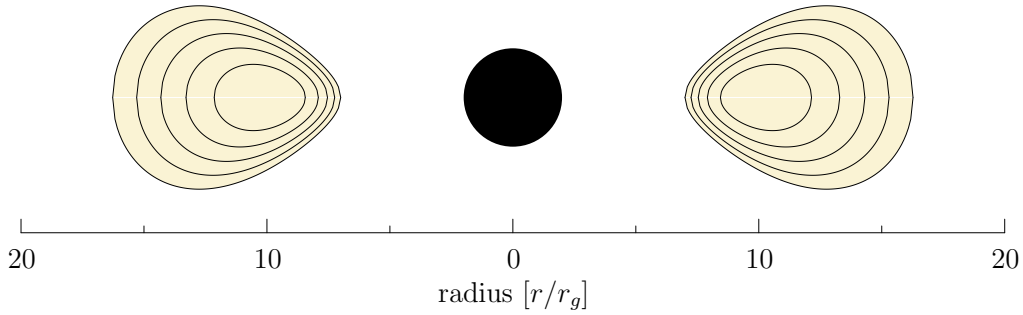

FIGURE 3.1: A relativistic torus surrounding a black hole. Equipotential contours, given by equation (3.26) are separated by a constant step in the effective potential.

Equipotential structure of a barotropic fluid

For a barotropic fluid, *i.e.* the fluid described by a one-parametric equation of state $p=p(\epsilon)$, the surfaces of constant pressure and constant total energy density coincide and it is possible to find a potential W such that $\nabla W = -\nabla p/(p+\epsilon)$, which simplifies the problem enormously. If the left-hand side of the equation can be expressed as a gradient, it follows that the right-hand side has to be expressed as a gradient as well. It therefore implies that there exists an invariant function – a rotation law

$$\Omega = \Omega(\ell) \,, \tag{3.23}$$

which characterizes the rotation of the fluid. If we define a potential Ψ as

$$\Psi = -\int_{\ell_0}^{\ell} \frac{\Omega \, \mathrm{d}\ell}{1-\Omega\,\ell} \,, \tag{3.24}$$

then the solution of Euler equation (3.22) can be compactly written in the form

$$W = \mathcal{U} + \Psi + \mathrm{const} \,. \tag{3.25}$$

The shape of the 'equipotential' surfaces $W(r,\,\theta) = \mathrm{const}$ is then given by specification of the rotation law (3.23) and of the gravitational field. The equipotential surfaces can be closed or open. The closed ones determine stationary equilibrium configurations – the fluid can fill any of these. Moreover, there is a special self-crossing surface (with a cusp located in the equatorial plane), where accretion onto the black hole is possible due to the Paczyński (1987) mechanism.

Of particular interest is a point, where the actual radial distribution of angular momentum crosses the Keplerian distribution. It represents the centre of the torus r_0, where the pressure p has zero gradient (also density has zero gradient here). At this point, gravitational and centrifugal force are just balanced and the fluid moves freely with the rotational velocity Ω and the specific angular momentum ℓ having their Keplerian values

$\Omega_{\rm K}(r_0)$ and $\ell_{\rm K}(r0)$. Inside the central ring radius, the angular momentum distribution is super-Keplerian, $\ell > \ell_{\rm K}(r_0)$, so that the pressure gradient forces must be directed inwards to balance the surplus centrifugal force. Outside r_0 the situation is just opposite – pressure compensates the deficient of the centrifugal source in the flow with sub-Keplerian distribution of ℓ.

The problem is usually further simplified by the assumption of constant specific angular momentum. It is known that all characteristic properties of the equipotential surfaces for a general rotation law are reflected by the equipotential surfaces of the simplest configurations with constant ℓ (Jaroszyński *et al.* 1980). Moreover, such a configuration is very important astrophysically, being marginally stable (Seguin 1975). Under the condition ℓ=const, the rotational potential Ψ is zero and a simple relation follows from (3.25),

$$W(r,\,\theta) \equiv \ln(-u_t) = \frac{1}{2}\,\ln\left[\frac{-\,g_{tt}\,g_{\phi\phi}}{g_{\phi\phi}+\ell^2\,g_{tt}}\right]\,, \tag{3.26}$$

in which the shape of equipotentials is given by the value of ℓ and by metric coefficients only. The profile of the equipotential surfaces for a non-self-gravitating torus with constant specific angular momentum is illustrated in Figure 3.1.

3.2 Slender approximation

We will assume that the accreting gas filling the torus is in an adiabatic equilibrium and can be described by a polytropic equation of state of the form (Tooper 1965)

$$p = K\,\rho^{\gamma} \tag{3.27}$$

with the energy density given as

$$\epsilon = \rho + \frac{p}{\gamma-1}\,. \tag{3.28}$$

Here, γ is the adiabatic index, which has a value of $^5/_3$ for a mono-atomic (completely ionized) gas, and K is the polytropic constant determining the specific adiabatic process. The polytropic constant implicitly contains the temperature of the gas and may be determined by finding the pressure and density at a given point, *e.g.* the torus centre.

Polytropes represent a special subclass of barotropic fluid configurations, which enables us to integrate the right-hand side of the equation (3.22) to find the potential W (the enthalpy of the gas) in terms of thermodynamical quantities.

$$\begin{aligned} W = -\int\frac{\mathrm{d}p}{p+\epsilon} = -\int\frac{\mathrm{d}p}{\frac{\gamma}{\gamma-1}\,p+\left(\frac{p}{K}\right)^{1/\gamma}} = \\ -\ln\left[1+\frac{K\,\gamma}{\gamma-1}\,\rho^{\gamma-1}\right] = -\ln\left[1+\frac{\gamma}{\gamma-1}\,\frac{p}{\rho}\right]\,. \end{aligned} \tag{3.29}$$

The integration constant has been conveniently chosen by the condition $W(\rho{=}0) = 0$ so that the zero level of W is on the surface of the torus, where the density is zero too. When

the local sound speed $c_{\rm s}^2 \equiv {\rm d}p/{\rm d}\rho \propto p/\rho$ is small compared to the speed of light $c^2 = 1$, the above expression can be approximated by

$$W \simeq -\frac{\gamma}{\gamma - 1}\frac{p}{\rho} \,. \tag{3.30}$$

It is convenient to introduce the Lane-Emden function $f(r,\, z)$ (Chandrasekhar 1960) by

$$\rho = \rho_0\, f^n \quad \text{and} \quad p = p_0\, f^{n+1} \,, \tag{3.31}$$

where $n = (\gamma - 1)^{-1}$ is called the polytropic index. The function f is equal to unity at the central pressure maximum and is zero on the torus surface. Substituting into (3.25) we obtain the Bernoulli equation in the form

$$\mathcal{U} + \Psi + (n+1)\,\frac{p_0}{\rho_0}\, f = {\rm const} \,, \tag{3.32}$$

where the integration constant can be determined by evaluating the equation at the central point. For a constant specific angular momentum fluid, which is hereafter assumed, and according to the definition (3.24) of the potential Ψ we find

$$f = 1 - \frac{\rho_0}{p_0\,(n+1)}\Big(\mathcal{U} - \mathcal{U}_0\Big) \,. \tag{3.33}$$

We are interested in how the function f behaves in the vicinity of the torus centre. For that purpose we introduce spherical coordinates $(t,\, r,\, \theta,\, \phi)$ and define expansion variables $\bar{x}$, $\bar{z}$ by ${\rm d}\bar{x} = \sqrt{g_{rr}}\,{\rm d}r/r_0$, ${\rm d}\bar{z} = \sqrt{g_{\theta\theta}}\,{\rm d}\theta/r_0$ with the condition $\bar{x} = \bar{z} = 0$ at the torus centre r_0, where also the metric coefficients are evaluated. For the difference of the effective potential between the centre and its vicinage we have

$$\mathcal{U} - \mathcal{U}_0 = \frac{r_0^2}{2}\left[\frac{1}{g_{rr}}\left(\frac{\partial^2\mathcal{U}}{\partial x^2}\right)_0 \delta\bar{x}^2 + \frac{1}{g_{\theta\theta}}\left(\frac{\partial^2\mathcal{U}}{\partial x^2}\right)_0 \delta\bar{z}^2\right] \,. \tag{3.34}$$

The first derivatives of $\mathcal{U}$ miss because the central point corresponds to the minimum of the potential and the mixed second derivatives vanish due to the reflection symmetry around the equatorial plane. The second derivatives of the effective potential with respect to $\bar{x}$ and $\bar{z}$ give radial and vertical epicyclic frequencies $\omega_r^{(1)}$ and $\omega_z^{(1)}$ in the centre of the torus as measured by a local co-moving observer (Abramowicz & Kluźniak 2004a, *c.f.*).

Following the notation of Blaes (1985), we define a parameter β determining the thickness of the torus,

$$\beta^2 \equiv \frac{2(n+1)\,p_0\, g_{tt}^2(r_0)}{\rho_0\,\Omega_0^2\, r_0^2} = \frac{2\,n\,c_{\rm s\,0}^2\, g_{tt}^2(r_0)}{\Omega_0^2\, r_0^2} \,. \tag{3.35}$$

If we rewrite equation (3.34) and substitute derivatives of $\mathcal{U}$ by dimensionless epicyclic frequencies $\bar{\omega}_r \equiv \omega_r/\Omega_0$ and $\bar{\omega}_z \equiv \omega_z/\Omega_0$, we obtain

$$f = 1 - \frac{1}{\beta^2}\Big(\bar{\omega}_r^2\,\bar{x}^2 + \bar{\omega}_z^2\,\bar{z}^2\Big) \,. \tag{3.36}$$

The torus is *slender* if $\beta \ll 1$, *i.e.* when the rotation flow is highly supersonic. The torus in this limit is geometrically thin and the surfaces of constant pressure and density have elliptic shapes with semiaxes in the ratio of the epicyclic frequencies. Moreover, in the Newtonian gravitational field, $\Phi \propto 1/r$, indeed the ellipses become circles and the torus is circular in cross-section with the radius $R_0 = \beta\, r_0$.

3.3 Perturbed equilibrium and epicyclic modes

Now, we consider small perturbations around the equilibrium of the stationary and axially symmetric torus in the form

$$X(r,\, \theta,\, \phi,\, t) = \delta X_*(r,\, \theta)\, e^{i(m\phi - \omega t)}\ . \tag{3.37}$$

These perturbations are, in terms of a single quantity $\mathcal{W}$, governed by the Papaloizou-Pringle equation. This equation was originally derived (Papaloizou & Pringle 1984) in Newtonian theory and only recently it was generalized to be valid in Einstein gravity too (Abramowicz *et al.* 2005c).

The general relativistic form of the quantity $\mathcal{W}$ is

$$\mathcal{W} = \frac{\delta p}{u^t\, \rho\, (m\Omega - \omega)}\ . \tag{3.38}$$

For barotropic $\ell = \text{const}$ tori, Abramowicz *et al.* derived a covariant version of the Papaloizou-Pringle equation, which in the slender limit ($\beta \to 0$) reads

$$f\, \frac{\partial^2 \mathcal{W}}{\partial r^2} + n\, \frac{\partial f}{\partial r}\, \frac{\partial \mathcal{W}}{\partial r} + f\, \frac{\partial^2 \mathcal{W}}{\partial z^2} + n\, \frac{\partial f}{\partial z}\, \frac{\partial \mathcal{W}}{\partial z} + \frac{2n}{\beta^2} \left(m - \frac{\omega}{\Omega_0} \right) = 0\ . \tag{3.39}$$

It is identical in form with the non-relativistic Papaloizou-Pringle equation for oscillations of the constant angular momentum slender tori, so it also has the same solutions. In the spherically symmetric Newtonian potential ($\omega_r = \omega_z$), this equation was fully solved in exact analytic form by Blaes (1985), who gave a complete set of its eigenmodes, with a complete analytic description of all eigenfunctions and all eigenfrequencies. More recently, Blaes *et al.* (2006) found that in general Newtonian case ($\omega_r \neq \omega_z$), there are two particular solutions of the equation,

$$\mathcal{W}_r = C_r\, r\, e^{i(m\phi - \omega_r t)}, \quad \mathcal{W}_z = C_z\, z\, e^{i(m\phi - \omega_z t)}\ , \tag{3.40}$$

with C_r, C_z being two arbitrary constants. The solution (3.40) is consistent with epicyclic oscillation modes. The fluid velocity is spatially constant on the torus cross-sections, entirely radial in the case of the radial epicyclic mode $\mathcal{W}_r$ and entirely vertical in the case of the vertical epicyclic mode $\mathcal{W}_z$. The radial and vertical oscillations are sinusoidal, with frequencies equal to the epicyclic frequencies ω_r and ω_z. Moreover these modes are axisymmetrical and therefore stable against the Papaloizou-Pringle instability.

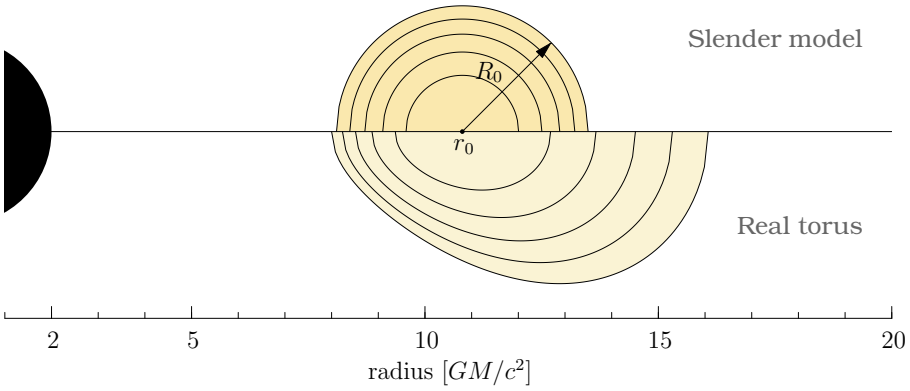

FIGURE 3.2: An illustration of the equipotential structure of a real relativistic torus (*lower part*) and of our circular slender torus model (*upper part*) surrounding a black hole. The equipotential contours are separated by equal steps in the potential W.

3.4 Model of a slender torus

We will use the previous results to construct a simple model of an slender torus filled with an polytropic hot and optically thin gas. We setup its equipotential structure and prescribe the emissivity.

Thermodynamical properties

When the torus is in the hydrodynamic equilibrium, pressure gradients specified by the enthalpy W are just compensated by gradients of the effective potential $\mathcal{U}$ so that $W = \mathcal{U} + \text{const}$. In the case of a constant specific angular momentum torus, this relation explicitly gives W in terms of the metric functions (equation 3.26).

From the thermodynamical point of view, the enthalpy (plus the equation of state) specifies the pressure, density and temperature structure. In a polytropic torus, the relation is given by equation (3.29), from which we can extract a formula for the density on the torus cross-section,

$$\rho(\varpi) = \left[\frac{\gamma-1}{K\,\gamma}\left(e^{W(\varpi)}-1\right)\right]^{\frac{1}{\gamma-1}} . \tag{3.41}$$

Here, we have introduced the cross-sectional radius ϖ, which measures the radial distance from the torus centre (see Figure 4.10 on p. 81). Assuming the gas is ideal and satisfies $p\,V = N\,k_{\mathrm{B}}\,T$, we also get a formula for the temperature,

$$T(\varpi) = \frac{m_{\mathrm{u}}\,\mu}{k_{\mathrm{B}}}\frac{p}{\rho} = \frac{m_{\mathrm{u}}\,\mu}{k_{\mathrm{B}}}\frac{\gamma-1}{\gamma}\left(e^{W(\varpi)}-1\right) , \tag{3.42}$$

where μ, k_{B} and m_{u} and the molecular weight, the Boltzmann constant and the atomic mass unit, respectively.

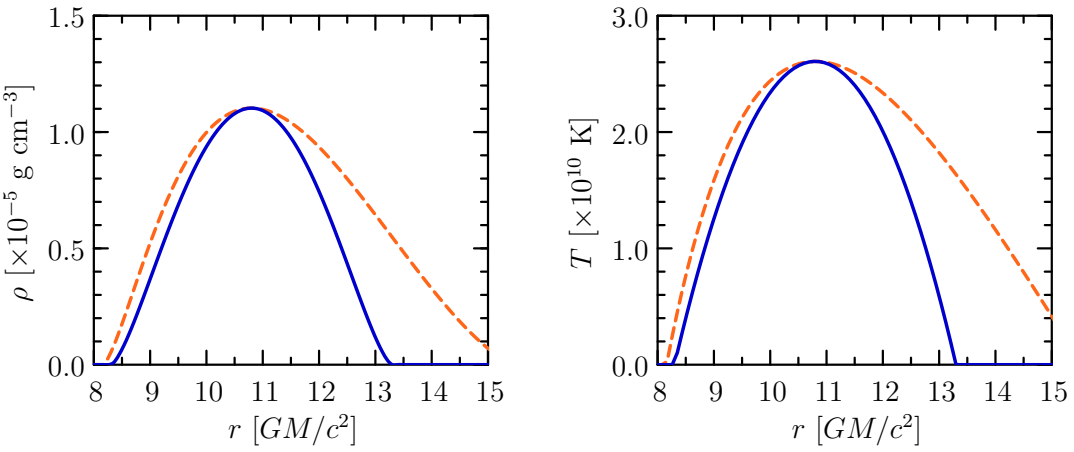

FIGURE 3.3: The density (*left*) and temperature (*right*) profiles of a polytropic gas forming an accretion torus with the centre at $r_0 = 10.8\,M$. Solid lines represent the slender model with radius $R_0 = 2\,M$ and dashed lines represent the real torus filling the potential well of the same depth.

Equipotential structure

We have seen in Section 3.2 that in the slender limit cross-sections of the torus have an elliptical shape. For our torus model, we make even stronger simplification and construct a torus with circular cross-sections as it is in the Newtonian limit. We make an expansion of (3.26) at the central point $r = r_0$ in the z-direction to obtain the profile of the enthalpy in the form

$$W(\varpi) = \frac{R_0^2 - \varpi^2}{2\,r_0^2\,(r_0/r_{\rm g} - 3)}\,. \tag{3.43}$$

Again, the integration constant is set such that the enthalpy is equal to zero on the torus surface, $W(R_0) = 0$.

By combining (3.43) with (3.41) and (3.42) we obtain the density and temperature profiles in the torus body. The equipotential structures of a relativistic torus, determined by Eq. 3.26, and of our model are illustrated in Figure 3.2 and the corresponding profiles of the density and temperature are shown in Figure 3.3.

Bremsstrahlung cooling

The bremsstrahlung emission includes radiation from both electron–ion and electron–electron collisions (Stepney & Guilbert 1983; Narayan & Yi 1995b),

$$f = f_{ei} + f_{ee}\,. \tag{3.44}$$

The contributions of either types are given by

$$f_{ei} = n_e\,\bar{n}\,\sigma_T\,c\,\alpha_f\,m_e\,c^2\,F_{ei}(\theta_e) \quad \text{and} \tag{3.45}$$

$$f_{ee} = n_e^2\,c\,r_e^2\,\alpha_f\,m_e\,c^2\,F_{ee}(\theta_e)\;, \tag{3.46}$$

where n_e and $\bar{n}$ are number densities of electrons and ions, m_e and $r_e = e^2/m_e c^2$ denotes mass of electron and its classical radius, α_f is the fine structure constant, $F_{ee}(\theta_e)$ and $F_{ei}(\theta_e)$ are radiation rate functions and $\theta_e = k\,T_e/m_e\,c^2$ is the dimensionless electron temperature. $F_{ee}(\theta_e)$ and $F_{ei}(\theta_e)$ are about of the same order, so that the ratio of electron–ion and electron–electron bremsstrahlung is

$$\frac{f_{ei}}{f_{ee}} \approx \frac{\sigma_T}{r_e^2} \approx 8.4 \tag{3.47}$$

and we can neglect the contribution from electron–electron collisions. For the function $F_{ei}(\theta_e)$ Narayan & Yi (1995b) give the following expression:

$$F_{ei}(\theta_e) = 4\left(\frac{2\theta_e}{\pi^3}\right)^{1/2}\left[1 + 1.781\,\theta_e^{1.34}\right]\;, \qquad \theta_e < 1\;, \tag{3.48}$$

$$= \frac{9\theta_e}{2\pi}\left[\ln(1.123\,\theta_e + 0.48) + 1.5\right]\;, \qquad \theta_e > 1\;. \tag{3.49}$$

In case of multi-component plasma, the density $\bar{n}$ is calculated as a sum over individual ion species, $\bar{n} = \sum Z_j^2\,n_j$, where Z_j is the charge of j-th species and n_j is its number density. For a hydrogen–helium composition with abundances $X:Y$ the following hold for the electron, ion and total density:

$$n_e \equiv \sum Z_j\,n_j \quad = \quad 1\cdot n_{\rm H} + 2\cdot n_{\rm He} \quad = \quad \tfrac{X+2Y}{X+Y}\,\sum n_j\;, \tag{3.50}$$

$$\bar{n} \equiv \sum Z_j^2\,n_j \quad = \quad 1\cdot n_{\rm H} + 4\cdot n_{\rm He} \quad = \quad \tfrac{X+4Y}{X+Y}\,\sum n_j\;, \tag{3.51}$$

$$\rho \equiv \sum A_{{\rm r}j}\,m_{\rm u}\,n_j \;=\; m_{\rm u}(1\cdot n_{\rm H} + 4\cdot n_{\rm He}) \;=\; m_{\rm u}\,\tfrac{X+4Y}{X+Y}\,\sum n_j\;, \tag{3.52}$$

where $A_{{\rm r}j}$ is the relative atomic weight of the j-th species, $m_{\rm u}$ denotes the atomic mass unit and we define $\mu \equiv (X+4Y)/(X+Y)$. The emissivity is then

$$f_{ei} = 4.30\times10^{-25}\,\tfrac{\mu+2}{3\,\mu}\,\rho^2\,F_{ei}(\theta_e)\;\;\text{erg cm}^{-3}\;\text{s}^{-1}\;, \tag{3.53}$$

which for the non-relativistic limit ($\theta_e \ll 1$) and Population I abundances ($X = 0.7$ and $Y = 0.28$) gives

$$f_{ei} = 3.93\times10^{20}\,\rho^2\,T^{1/2}\;\;\text{erg cm}^{-3}\;\text{s}^{-1}\;. \tag{3.54}$$

This formula differs from the one given by Abramowicz *et al.* (1996, Eq. 65), as they apparently did not multiply their formula by the abundance factor.

3.5 Computational method

Most of the results presented in the following Chapter are obtained using a numerical ray-tracing. The detailed description of the `sim4` code, which has been used for calculations, is given in Appendix B. Here we only briefly review the basic assumptions, the computational scheme and describe the methods of analysis of the resulting lightcurves.

Spacetime metric

Numerical ray-tracing calculations are mostly performed in the Schwarzschild spherically symmetric spacetime, described by a metric function (in spherical coordinates)

$$\mathrm{d}s^2 = -\left(1-\frac{2\,M}{r}\right)\,\mathrm{d}t^2 + \left(1-\frac{2\,M}{r}\right)^{-1}\,\mathrm{d}r^2 + r^2\,(\,\mathrm{d}\theta^2 + \sin\theta^2\,\mathrm{d}\phi^2)\,. \tag{3.55}$$

For comparisons with the flat-spacetime situation without light bending, some calculations are done using the Minkowski metric,

$$\mathrm{d}s^2_{\mathrm{mk}} = -\,\mathrm{d}t^2 + \,\mathrm{d}r^2 + r^2\,(\,\mathrm{d}\theta^2 + \sin\theta^2\,\mathrm{d}\phi^2)\,. \tag{3.56}$$

The Schwarzschild metric is the basic choice to start with. It includes all important general relativistic effects, but is sufficiently simple in the sense that photon trajectories are planar. This simplicity allows to more easily isolate and recognise the essential effects of strong gravity on light propagation, as we will see in the next Chapter.

Ray-tracing

The code uses a method of direct ray-tracing outlined by Ftaclas *et al.* (1986) instead of the more frequently used transfer-function method (Cunningham 1975, 1976), as it is more convenient for the numerical calculations of radiative transport in the spatially extended emitters. The ray-tracing calculations are performed by numerical integrating the geodesic equation and the equation of geodesic deviation using a fourth-order Runge-Kutta integrator with an adaptive step-size control. The adaptive stepping in the affine parameter allows the integration routine to quickly overrun the long path in the relatively flat spacetime far from the source of gravity and, on the other hand, carefully pass the strong-curvature region near the black hole while maintaining high accuracy of 10^{-12}. It is also used to determine intervals at which to record photon's position and momentum.

A special care is taken to process photon paths near-crossing the coordinate polar axis, where the $g_{\theta\theta}$ component of the metric is close to zero and the integrator has problems to pass over this point. When $|\sin\theta| < 10^{-5}$, the integration step is repeatedly multiplied by a value proportional to the inclination and chosen accuracy, which causes the the integration to overskip the pole and continue with unchanged momentum.

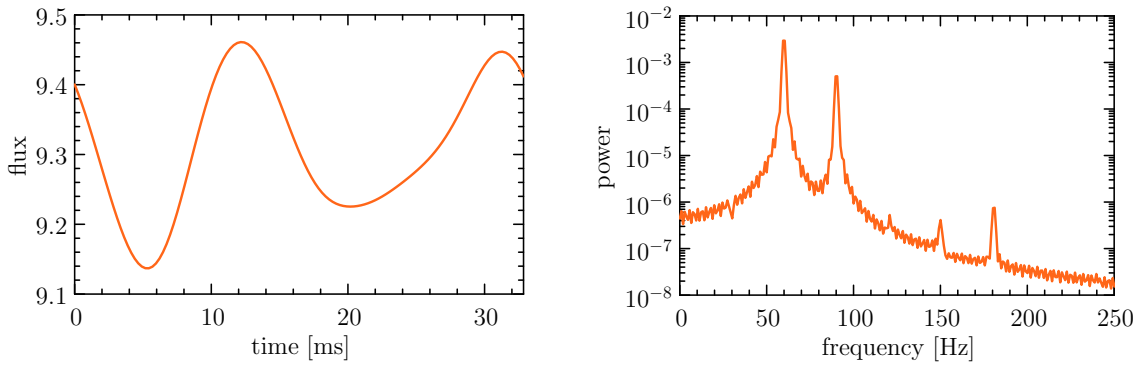

FIGURE 3.4: An example lightcurve (*left*) and the corresponding power spectrum (*right*) as a result of numerical ray-tracing.

The lightcurves and images presented in this work have been calculated using the sets of 300×300 or 500×500 (for lightcurves) and 1000×1000 (for images) rays. For each ray, from many hundreds up to several thousands of waypoints are recorded during the ray-tracing. The waypoints are then used to reconstruct the photon's trajectory when computing lightcurves, so it is possible for each photon bundle (*i.e.* a pixel on the image plane) to follow up its way from and/or through the source to the observer and integrate the radiation transfer equation.

Since the image is constructed on the observer's sky plane, all gravitational lensing effects connected to changing areas of photon-flux tubes are implicitly included by the calculation method. Regions of high magnification behind the black hole will cover more pixels of the image, hence they will appear brighter than the non-magnified regions. This is one of advantages of the direct ray-tracing method. The integration over the source, instead of over the image, would require a Jacobian transformation between the source and observer coordinates (see *e.g.* Dovčiak 2004 for a detailed description and usage of the transfer-function method).

Fourier analysis of lightcurves

Using the `sim4` code numerous lightcurves have been computed for various values of configuration parameters. Each lightcurve covers as many Keplerian periods $T_{\mathrm{K}} = 2\,\pi/\Omega_{\mathrm{K}}(r_0)$ as needed for the torus to complete the oscillations movements and return to its initial position and phase. All lightcurves have been computed with 128 or 256 time bins, so that the sampling frequency varied with the duration of simulations, but typically about 40 time bins per one Keplerian period were used.

The resulting lightcurves have been fourier-analysed using the standard Fast Fourier Transform (Press *et al.* 1986). Oscillation powers have been read by fitting the power

density spectrum (PDS) with Lorentzian profiles

$$L(\omega) = \frac{LN}{4\left(\dfrac{\omega - \omega_{\rm c}}{LW}\right)^2 + 1} \ , \tag{3.57}$$

with the centroid frequency $\omega_{\rm c}$ being the frequency of imposed oscillations. The powers, given as

$$P(\omega_{\rm c}) = 2\pi\, LN\, LW \ , \tag{3.58}$$

have been finally converted to the fractional root mean square amplitudes of the total bolometric luminosity, as described in Appendix C. An example lightcurve from the numerical ray-tracing and the corresponding power spectrum are shown in Figure 3.4.

CHAPTER 4

Strong gravity effects on light modulation from an oscillating slender torus

Relativistic tori can generally oscillate in a mixture of internal and global modes. Internal modes invoke pressure and density waves within the torus, while its shape remains nearly unchanged. The outgoing flux is therefore directly modulated by variations in the profiles of thermodynamical properties and by the corresponding change of the local emissivity in the optically thin medium. In this case, lensing or any general relativistic effect on the radiation transport is not important, which is off our interest here. Global modes, on the other hand, alter mainly the topological structure and spatial distribution of the material. Because light rays do not follow straight lines in a curved spacetime, these changes can be displayed out by effects of gravitational lensing and light bending.

Numerous models have been proposed so far to explain the black-hole QPO's origin. The production of QPOs has been examined with models of orbiting blobs and spots (Stella & Vietri 1999; Schnittman & Bertschinger 2004), a resonance between some modes of orbital motion (Kluźniak & Abramowicz 2001), extended non-axisymmetric features (*e.g.* spiral arms or warps; Kato 2004; Wagoner *et al.* 2001), thick or non-planar accretion discs (Rezzolla *et al.* 2003), magnetic coupling between the black hole and the disc (Wang *et al.* 2005), *etc.*

So far, a certain level of non-axisymmetry has been preferred in proposed models, as it was thought that a non-axisymmetry is a necessary condition for the X-ray flux modulation in black-hole QPOs. Here we show that gravitational bending of the photon trajectories in the vicinity of a black hole suffices to appreciably modulate the flux observed at infinity even if the source of radiation is axially symmetric.

In this final Chapter we show how simple global oscillation modes of a gaseous torus affect the outgoing flux received by a static distant observer and how the flux modulation depends on the geometry and various parameters of the torus. We perform a large-scale three-dimensional ray-tracing in the Schwarzschild spacetime and show that a perfectly axisymmetric torus oscillating in the radial and vertical directions can in principle cause a significant modulation of emerging radiation. The modulation at the radial oscillation frequency is caused by changes of the gas properties in the torus, while only general relativistic effects of strong gravity (such as light lensing, bending and time delays) are responsible for modulation at the vertical oscillation frequency. Radiation produced in any relativistic torus, how complex soever its oscillations can be, will then be subject to the very same modulation by strong gravity effects.

The first section of this Chapter describes the rigid oscillation modes that we impose on the stationary and incompressible torus. In the following sections we subsequently discuss in details the effects of the g-factor, spacetime geometry, observer's inclination, torus size and distance, and of the obscuration by an outer optically thick disc. Then we slightly generalise the initial assumptions and relax the incompressibility condition. The last section presents some preliminary results of ray-tracing from the 3D MHD simulation of an optically thin accretion flow.

This Chapter is based on work published in Bursa *et al.* (2004) and Bursa (2005).

4.1 Oscillation of a slender torus

We impose on the torus rigid and axisymmetric ($m=0$) sinusoidal oscillations in the vertical direction, *i.e.* parallel to its axis, as well as in the perpendicular radial direction. Such assumption will serve us to model the possible basic global modes found by Abramowicz *et al.* (2005c). In our model, the torus is rigidly displaced from its equilibrium (Figure 4.10), so that the position of the central circle of maximal pressure varies in time as

$$r(t) = r_0 + \delta r \, \sin(\omega_r t) \, , \tag{4.1}$$

$$z(t) = \delta z \, \sin(\omega_z t) \, . \tag{4.2}$$

Here, $\omega_z = \Omega_{\rm K} = (M/r_0^3)^{\frac{1}{2}}$ is the vertical epicyclic frequency, in Schwarzschild geometry equal to the Keplerian orbital frequency, and $\omega_r = \Omega_{\rm K}(1-6r_{\rm g}/r_0)^{\frac{1}{2}}$ is the radial epicyclic frequency. The torus is placed at the distance $r_0=10.8\,M$ so that the oscillation frequency ratio $\omega_z:\omega_r$ is $3:2$, but the choice is arbitrary and only serves to mimic the observed frequency ratio. In the default configuration, the cross-section radius is $R_0=2.0\,M$ and amplitudes of the both vertical and radial motion are set to $\delta z = \delta r = 0.1\,R_0$.

We initially assume an *'incompressible'* mode, where the equipotential structure, the thermodynamical quantities describing the torus and in particular its size are fixed and *do not vary* in time as the torus moves. This test case helps us to identify and fully understand the effects of light bending on observed lightcurves and power spectra. Later in this Chapter we describe also a *'compressible'* mode, which is more close to a real situation, and discuss how changes of the torus properties affect powers in the different oscillations.

The radial motion of the incompressible torus results in a periodic change of its volume. Because the optically thin torus is assumed to be filled with a polytropic gas radiating by bremsstrahlung cooling and we fix the density and temperature profiles, there is a corresponding change of luminosity $L \propto \int f \, {\rm d}V$, with a clear periodicity at $2\pi/\omega_r$. On the contrary, the vertical motion does not change the properties of the torus or its overall local luminosity. We find that in spite of this, and although the torus is perfectly axisymmetric, the flux observed at infinity clearly varies at the oscillation frequency ω_z. This is caused by relativistic effects at the source (lensing, beaming and time delay), and no other cause need to be invoked to explain in principle the highest-frequency modulation of X-rays in luminous black-hole binary sources.

4.2 The role of g-factor

The g-factor is one of the prominent relativistic effects, which plays a key-role in changing observed PDS powers in a modulated flux. It combines effects of the gravitational redshift and of the Doppler boosting. For a small viewing angles (face-on views), there is only significant gravitational redshift in the region close to the gravity centre (up to $\sim 20\,r_g$). Whereas for large viewing angles (edge-on views), Doppler shift becomes important as the

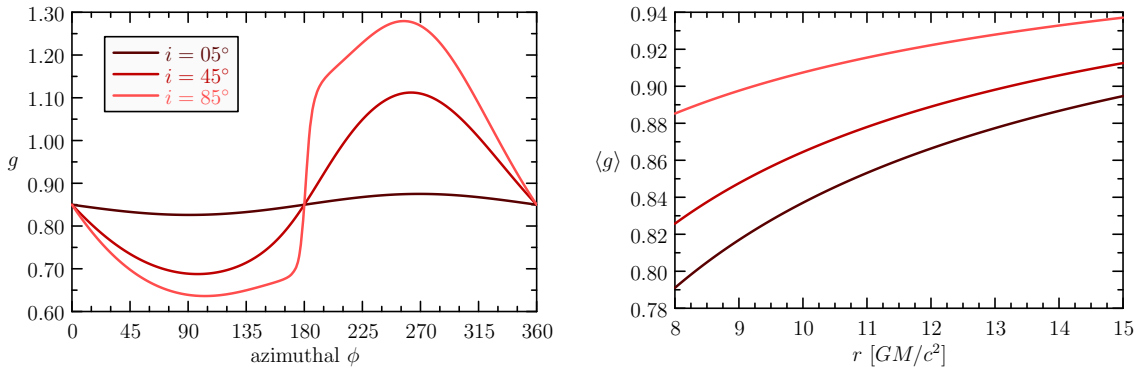

FIGURE 4.1: *Left*: The azimuthal dependence of g-factor (Doppler+redshift) from a circular Keplerian orbit at $r=10.8\,M$. The observer's azimuthal position is $\phi=0°$.
Right: The azimuthally averaged g-factor from Keplerian orbits at different radii.
(The approximative formula of Pecháček *et al.* (2005) has been used to plot these figures.)

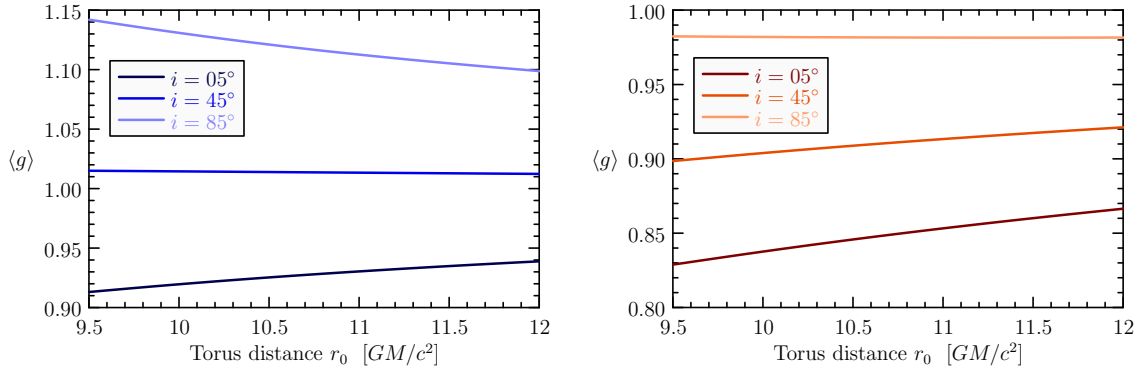

FIGURE 4.2: The radial dependence of the volume-averaged g-factor of a steady non-oscillating torus of size $R_0=2.0\,M$ placed at different radii. Both Minkowski (*left*, Doppler only) and Schwarzschild (*right*, Doppler+redshift) cases are shown.

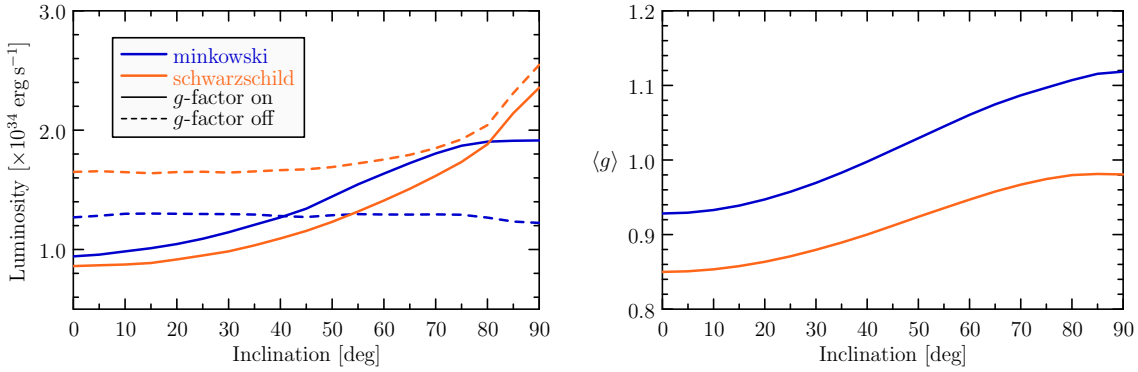

FIGURE 4.3: The total bolometric luminosity (*left*) and the volume-averaged g-factor (*right*) of a steady non-oscillating torus of size $R_0=2.0\,M$ placed at $r_0=10.8\,M$. Luminosities are computed with and without (*i.e.* $g\equiv1$) inclusion of the effect of g-factor. Both Minkowski and Schwarzschild cases are shown.

relative velocity of the orbiting gas changes. The effect of g-factor in the case of a fluid torus is illustrated in Figures 4.1–4.3 (see also *e.g.* Zhang *et al.* 2003 for maps of g-factor in the equatorial plane).

The Doppler effect brightens up the part of the accretion flow, where the gas moves towards the observer, and darkens the receding part,

$$g_{\mathrm{DP}} = \frac{1}{\gamma\,(1-\beta\cos\theta)}\ . \tag{4.3}$$

Here, γ is the Lorentz factor due to the total velocity of the gas and $\beta\cos\theta$ is the velocity directed towards the line of sight of a photon. The importance of the Doppler effect grows with increasing relative difference between radial gas velocities in the approaching and receding part of the flow; the effect is maximal for inclinations approaching $\pi/2$ (Figure 4.1, *left*). On average, *i.e.* azimuthally integrated over a circular orbit, the brightened part wins over the dimmed part (Figure 4.1) so that the observed emission increases with inclination (Figure 4.3).

The gravitational redshift component of the g-factor

$$g_{\mathrm{RS}} = \sqrt{-g_{tt}} = \sqrt{1-\frac{2\,r_{\mathrm{g}}}{r}}\ , \tag{4.4}$$

comes as a consequence of the equivalence principle and adds the dependence on the radial distance from the centre of gravity, which is an important fact to explain the qualitative differences between radial oscillation powers in the compressible and incompressible mode (later in this Chapter, Section 4.8). Its effect can be seen in Figure 4.1 (*right*).

Before we discuss how changes in different parameters of the model affect power of imposed oscillations, we consider for a moment a steady non-oscillating torus viewed from different angles. Figure 4.3 shows how the total bolometric luminosity of the torus changes with inclination of the observer. In Minkowski spacetime and if Doppler effect is omitted (*dashed blue line*), we expect the luminosity to be independent on the viewing angle and to be constant. This is indeed true, although there is some decrease for $i > 80°$ caused by a partial obscuration of the torus by the $2\,r_{\mathrm{g}}$ black-hole sphere. If Doppler is switched on (*solid blue line*), its effect beams the radiation mainly in the direction of the velocity of the orbiting fluid. Therefore, the luminosity is lower if viewed face-on and higher for an edge-on view, as compared with the previous case. The same effect of obscuring the of the torus slugs the rising trend at high viewing angles. In Schwarzschild spacetime, the effects of gravitational red-shift and light bending come into play and the situation is very much different. Without considering the g-factor (*dashed orange line*), the luminosity has initially a similar profile as with Minkowski metric, but when the observer is more than 45° inclined, it starts to grow thanks to the appearance of the secondary image of the rare part of the torus below the black hole. If g-factor is included (*solid orange line*), the luminosity is generally decreased because of the gravitational red shift of photon energies, but it rises steeply with inclination pushed up by the appearance of multiple images plus by the Doppler effect. At edge-on view it reaches almost the same level as the *dashed* line, while it is only $\sim$50 % if looking face-on.

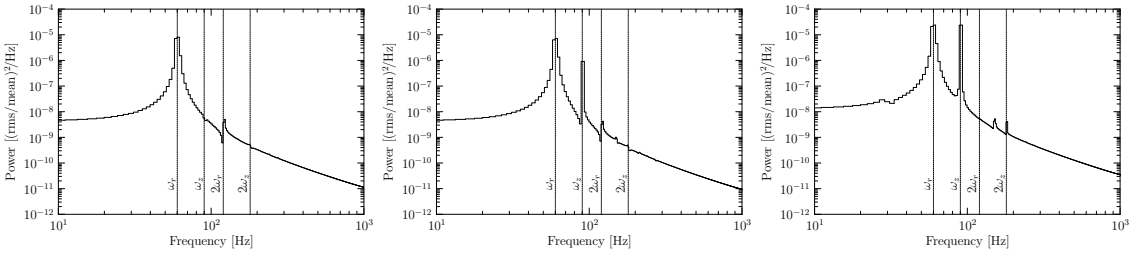

FIGURE 4.4: Power spectra of an oscillating torus calculated in the Newtonian limit (*left*), Minkowski spacetime (*middle*) and the Schwarzschild spacetime (*right*). Viewing angle is 70°.

4.3 Effect of spacetime geometry

In the Newtonian limit and when the speed of light $c \to \infty$, the only observable periodicity is the radial oscillation. There is no sign of any modulation at the ω_z frequency in the lightcurve, although the torus is moving vertically. This is clear and easy to understand, because the $c \to \infty$ limit suppresses the time delay effects and causes photons from all parts of the torus to reach an observer at the same instant of time, so it is really seen as rigidly moving up and down giving no reason for modulation at the vertical frequency.

When the condition of the infinite light speed is relaxed, the torus is no longer seen as a rigid body. The delays between photons, which originate at different parts of the torus body, significantly alter its image. Those emerging from the front and back at the same coordinate time will be detected at different instants separated by the interval

$$\Delta t \simeq \frac{2\, r_0}{c}\, \sin i\ , \tag{4.5}$$

where i is the viewing angle (*i.e.* inclination of the observer). It is maximal for an edge-on view ($i = {}^{\pi}/_{2}$) and compared to the Keplerian orbital period it is

$$\frac{\Delta t}{T_{\mathrm{K}}} \simeq (2\pi^2\, r_0/r_g)^{-1/2}\, \sin i\ . \tag{4.6}$$

This makes about 10% at $r_0 = 10.8M$. The torus is seen from distance as an elastic ring, which modulates its brightness also at the vertical oscillation frequency ω_z due to the time delay effect and the seeming volume change.

Curved spacetime adds the effect of light bending. Photons are focused by the central mass' gravity, which leads to a magnification of any vertical movement. Black hole is not a perfect lens, so that parallel rays do not cross in a single point, but rather form a narrow focal furrow behind it. When the torus trench the furrow (at high viewing angles), its oscillations are greatly magnified by the lensing effect. This is especially significant in the case of the vertical oscillation, as the bright centre of the torus periodically passes through the focal line.

Figure 4.4 illustrates the geometry effect on three Fourier power density spectra of an oscillating torus. The spectra are calculated for the same parameters and only the metric is changed. The appearance of the vertical oscillation peak in the 'finite light speed' case and its power amplification in the relativistic case are clearly visible.

4.4 Effect of inclination

In the previous paragraphs we have found out that both the time delay and the lensing effects are most pronounced when the viewing angle is high. Now we will show how much is the observed flux modulated when the torus is seen from different directions.

The effect of inclination is probably the most featured, in spite of it is difficult to be directly observationally determined. Changing the line of sight affect the power in the radial/vertical oscillation frequencies, because different effects are important at different angles. When the torus is viewed face-on (*i.e.* from the top), we expect the amplitude of ω_r to be dominant, as the radial pulsations of the torus can be nicely seen and light rays passing through the gas are not yet strongly bent. When viewed almost edge-on, the Doppler effect reduces the power of ω_r, while gravitational lensing amplifies the power in ω_z. Thus we expect the vertical oscillation to overpower the radial one. Figure 4.6 (*left*) shows the inclination dependence of oscillation powers in the Minkowski spacetime (*top* panel) and in the curved Schwarzschild spacetime (*bottom* panel).

In the case of flat spacetime, we see that the power of the radial oscillation is even, if Doppler effect is not considered. It corresponds to the periodic change of volume and luminosity (as measured by an observer orbiting with the fluid), $L^\circ \sim \int f \, \mathrm{d}V \sim \delta r \sin(\omega_r t)$. When special-relativistic effects are taken into account, they reflect variations in azimuthal orbital velocity of the fluid in the radially oscillating constant specific angular momentum torus. The observed variance in the luminosity is modified by the Doppler factor g_{DP}, $L \sim g_{\mathrm{DP}}^4 L^\circ$. Looking face-on, g_{DP} contains the transverse Doppler effect term only and is an increasing function of radius as well as L°, which in turn amplifies the power of the radial oscillation above the $g \equiv 1$ level. The effect of beaming $\sim (\beta \sin i)^{-1}$ starts to be important with higher viewing angles, it turns over the radial dependence of g_{DP} and weakens the radial oscillation power. The transition in the slope of $g_{\mathrm{DP}}(r)$ comes at $i \sim 45^\circ$, where the red curves cross each other. It will be shown in Section 4.8 that whether the power is decreased or increased with inclination depends on how L° depends on $r(t)$. The vertical oscillation decreases continuously with an increasing angle of view, being independent of the g-factor. At inclinations $i > 75^\circ$ it has, however, a significant excess, which is caused by the obscuration of part of the torus behind an opaque sphere of radius $2\,r_{\mathrm{g}}$ representing the central black hole.

When gravity effects on light rays propagation are added, the situation for the radial oscillation is very much similar to the Minkowski case, except that the attenuation of its power is softer and the transition in g-factor comes at higher inclination $\sim 70^\circ$ due to the effect of the gravitational red-shift. The importance of light bending is clearly visible from the blue line, *i.e.* the vertical oscillation, progression. It is raising slowly for inclinations $i > 45^\circ$, then it shows a steeper increase for $i > 75^\circ$, reaches its maximum at $i = 85^\circ$ and

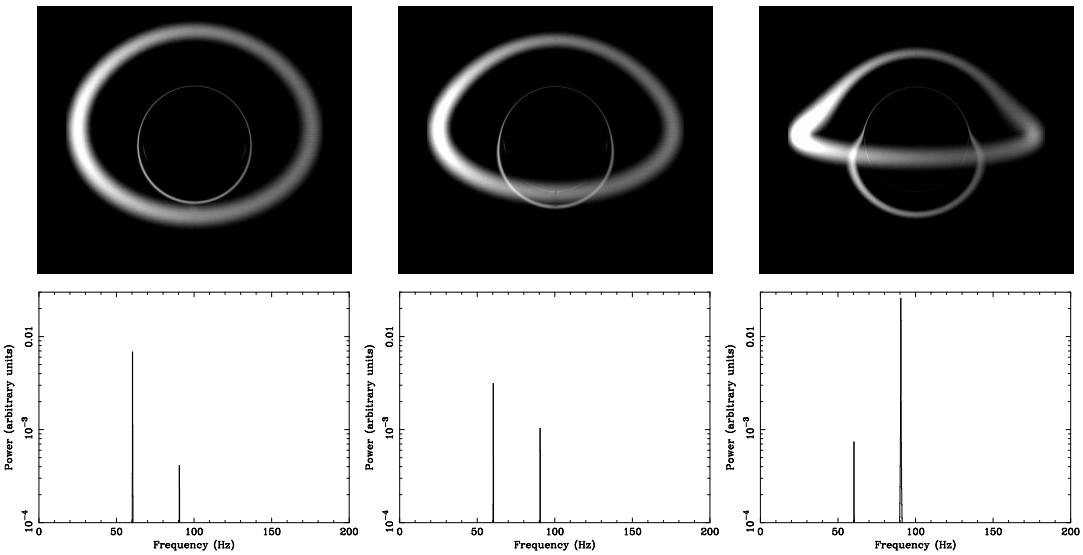

FIGURE 4.5: Results of numerical simulations of the oscillating torus in Schwarzschild geometry. The equilibrium distance of the torus $\tilde{r}_0 = 10.8M$, its cross-section radius is $R_0 = 1.5M$. (Top):–snapshots of an instant image, as viewed by a distant observer, (bottom):–the power spectrum, for three different viewing angles, $i = 45°$ (left), $60°$ (middle) and $80°$ (right).

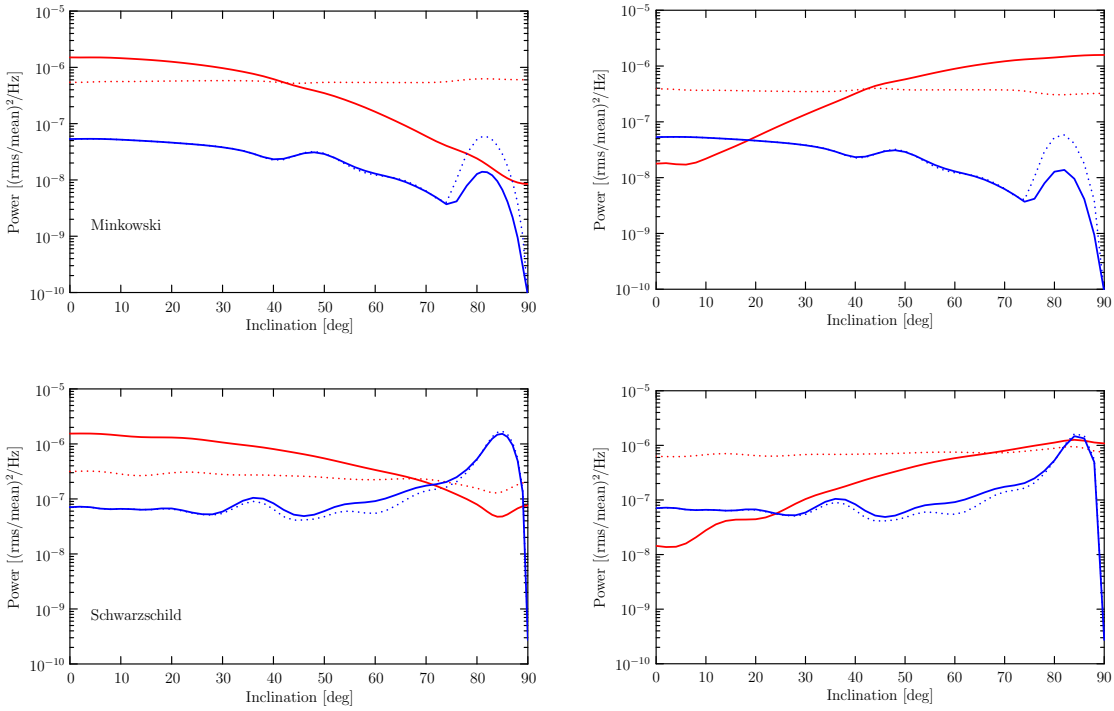

FIGURE 4.6: The inclination dependence of powers in the radial (*red*) and the vertical (*blue*) oscillations. Top panel shows calculations in the flat spacetime, bottom panel shows powers as computed in the curved Schwarzschild spacetime. Dashed lines represent the same calculations done with switched-off g-factor ($g \equiv 1$).

it finally drops down to zero. At the maximum it overpowers the radial oscillation by a factor of 40, while it is 20-times weaker if the torus is viewed face-on. The rapid decrease at the end is caused by the equatorial plane reflection symmetry. If the line of sight is in the $\theta = \pi/2$ plane, the situation is the same above and below the plane, thus the periodicity is $2\,\omega_z$. The power in the base frequency drops abruptly and moves to overtones.

4.5 Effect of the torus size

The effect of the size of the torus is very important to study, because it can be directly tested against observational data. Other free model parameters tend to be fixed for a given source (like inclination), but the torus size may well vary for a single source as a response to temporal changes in the accretion rate.

The power in the radial oscillation is correlated with its amplitude, which is set to $\delta r = 0.1\,R_0$ and grows with the torus size. It is therefore evident, that the radial power will be proportional to R_0 squared. If the amplitude was constant or at least independent of R_0, the ω_r power would be independent of R_0 too. Thus the non-trivial part of the torus size dependence will be incurred by vertical movements of the torus.

Figure 4.7 (*left*) shows the PDS power profiles of both the radial and vertical oscillations for several different inclinations. Indeed, the radial power has a quadratic profile and is more dominant for lower viewing angles, which follows from the previous paragraph. The power in the vertical oscillation is at low inclinations also quadratic and similar to the radial one, but the reason is different. The time delay effect causes apparent deformations from the circular cross-section as the torus moves up and down, *i.e.* to and from the observer in the case of a face-on view. The torus is squeezed along the line of sight at the turning points and stretched when passing the equatorial plane. Deformations are proportional to its size, being the reason for the observed profile. At high inclinations the appearance of strong relativistic images boosts the vertical oscillation power even more. But, as can be clearly seen from the 85° line and partially also from the 80° line, there is a size threshold, beyond which the oscillation power decreases though the torus still grows. This corresponds to the state, where the torus is so big that the relativistic images are saturated. Further increase of the torus size only entails an increase of the total luminosity, while the variability amplitude remains about the same, hence leading to the fractional rms amplitude downturn.

4.6 Effect of the torus distance

The distance of the torus from the gravity centre also affects the intensity of modulation in observed lightcurves (Figure 4.8, *left*). The power in the radial oscillation is either increasing or decreasing, depending on the inclination. Looking face-on, the g-factor is dominated by the redshift component and the power in ω_r is increasing with the torus distance being less dumped. When the view is more inclined, the Doppler component starts to be important and the oscillation looses power with the torus distance. The critical inclination is about 70°.

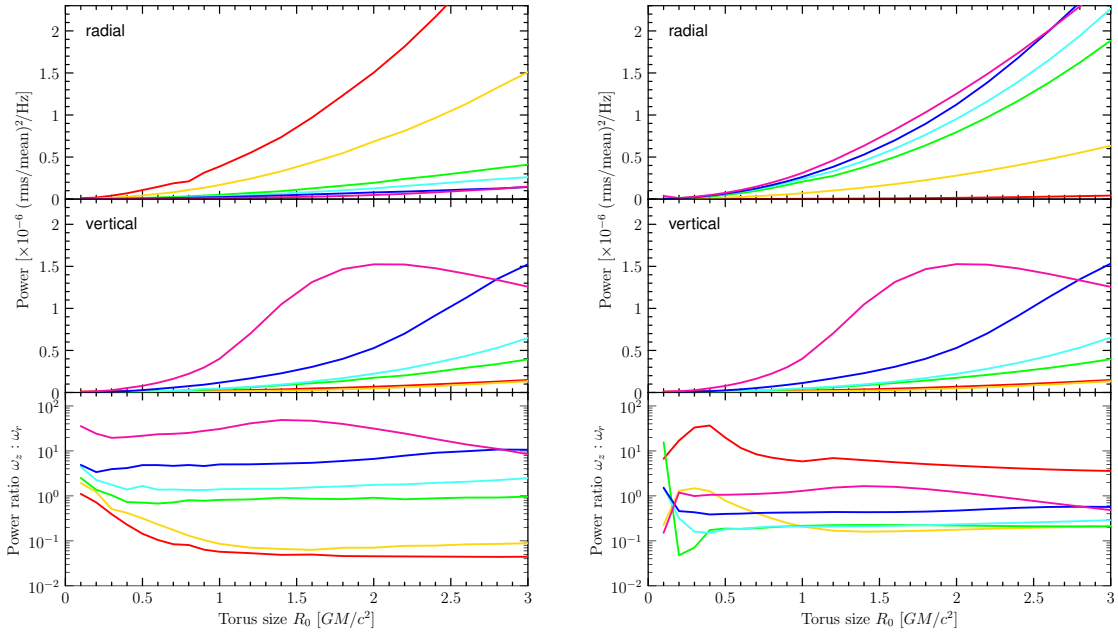

FIGURE 4.7: Powers in the radial (*top*) and vertical (*middle*) oscillations and their ratio (*bottom*) as a function of the torus size. Different viewing angles are plotted.

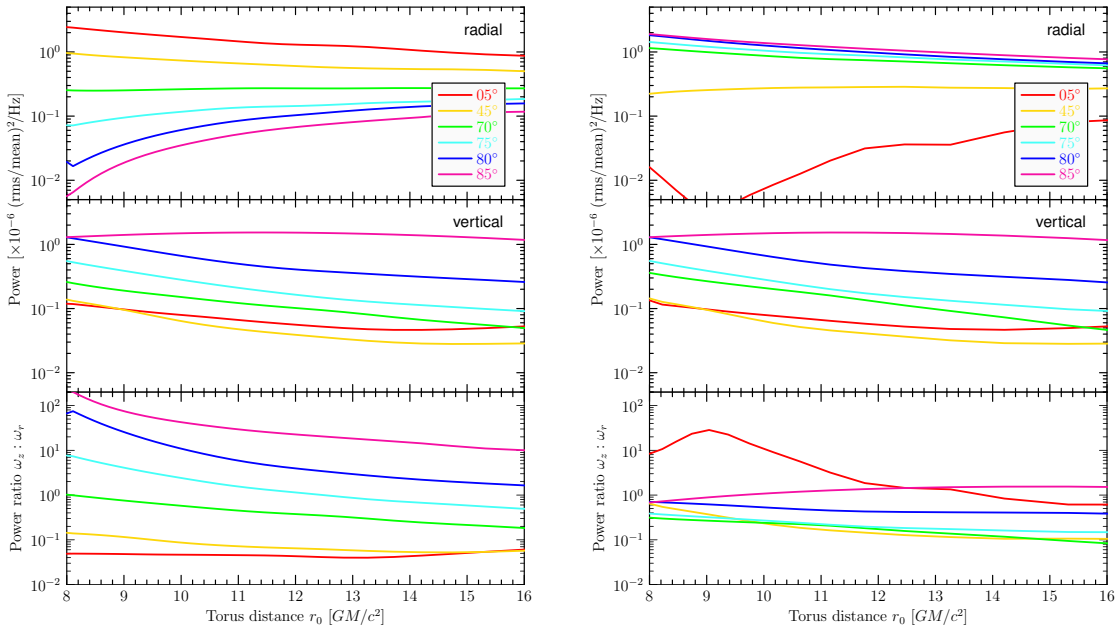

FIGURE 4.8: Powers in the radial (*top*) and vertical (*middle*) oscillations and their ratio (*bottom*) as a function of the torus distance from the gravity centre. Different viewing angles are plotted.

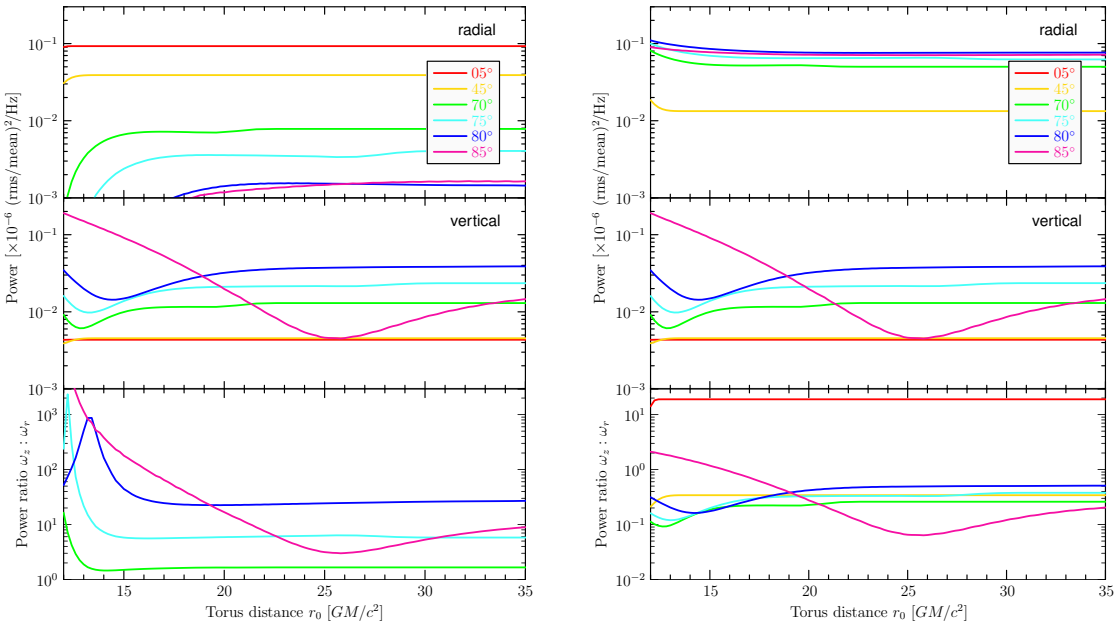

FIGURE 4.9: Powers in the radial (*top*) and vertical (*middle*) oscillations and their ratio (*bottom*) as a function of the torus distance from the gravity centre. Different viewing angles are plotted.

The power of vertical oscillation generally decreases with the torus distance. It is made visible mainly by the time delay effect and because with the increasing distance of the torus the oscillation period also increases, the effect is loosing on importance. An exception is when the inclination is very high. The large portion of visible relativistic images causes the vertical power first to increase up to some radius, beyond which it then decays. Both small and large tori do not have much of visible secondary images, because they are either too compact or they are too far. The ideal distance is about $11\,r_{\rm g}$ – this is the radius, where the torus has the largest portion of higher-order images, corresponding to the maximum of the vertical power.

Generally, the relative power of the vertical oscillation is getting weaker as the torus is more and more far-away from the gravitating centre. This is most significant for higher viewing angles, where the drop between $8\,r_{\rm g}$ and $16\,r_{\rm g}$ can be more than one order of magnitude. On the other hand, for low inclinations the effect is less dramatic and if viewed face-on the power ratio is nearly independent from the distance of the fluid ring.

4.7 Effect of disc obscuration

So far we have been assuming that there is only the torus around the black hole and that photons, once emitted, are either captured or can freely escape to infinity. In fact, there is likely an outer cool disc surrounding the torus, from which the torus is formed, and which

can as well have a substantial effect on light modulation. The Shakura–Sunyaev disc is optically thick and blocks propagation of photons crossing the equatorial plane beyond its terminal radius. Most of the stopped photons has been strongly bent and has carried information predominantly about the vertical mode, thus the presence or not-presence of an opaque disc may be important for the power distribution in QPO modes, namely the vertical one.

The disc is considered as a geometrically thin and non-transparent body. It lies in the the equatorial plane (at $z=0$) and goes from infinity down to some terminal radius r_{d}, which is a parameter of the model. For the purpose of this example, the torus is put somewhat closer to the black hole, with its inner edge near the marginally stable orbit. Its centre is at $r_0 = 9.4\,r_{\mathrm{g}}$, its size is $R_0 = 3.0\,r_{\mathrm{g}}$, and oscillation amplitudes are $\delta r = \delta z = 0.2\,r_{\mathrm{g}}$. The disc can extend as close as to the torus, but does not penetrate into it ($r_{\mathrm{d}} > r_0+R_0+\delta r$). Figure 4.9 (*left*) shows how powers in the oscillation modes are changed if an opaque disc is present.

If the system is viewed from low inclinations ($< 45°$), the disc has a little effect on the oscillation power. Strongly bent photons appear close to the photon orbit inside the main image of the torus and only a few of them are blocked by the disc, even if it goes close and touches the torus from outside. At larger inclinations ($> 45°$) and when the disc is close to the torus, power in the radial oscillation starts to decrease. It is because part of the torus is periodically obscured, which is compensated by the intrinsic luminosity modulation due to the changing volume in the incompressible mode, though. The power in the vertical oscillation is first lowered as the disc goes in, but then it is amplified again when the disc gets very close. The actual value of r_{d}, where the trend is changed, strongly depends on the inclination, roughly proportional to $\sim R_0 \tan i$. The power starts to decrease when the disc obscures the bottom outer lensed image of the rear part of the torus. This lensed image carries a large part of the ω_z power (especially at high inclinations), because it is formed by photons emitted near the optical caustic behind the black hole. Therefore, if part of this image is obscured, some power of the vertical oscillation is lost. When the disc gets only a few r_{g} away from the torus and obscures part of its direct image, the ω_z power is increased, because of a periodical change of the visible volume.

We can conclude that the presence of a thin disc is important, if the disc does not end far from the torus, but rather within a distance of ~ 5 gravitational radii from it, and when the viewing angle is moderate to high. Under these conditions the effect of the torus obscuration by an optically thick medium is capable to substantially change powers in oscillations, and in particular in the vertical mode.

4.8 Compressible torus

Up to this point the torus has been considered incompressible, which does not intrinsically respond to the perturbation of the radial distance in any way. Because the thermodynamical properties stay unchanged, the total mass $M = \int \rho \, \mathrm{d}V$ contained within the torus is

not conserved during the radial movements. Now, we relax this constraint and explore a more general case of an compressible torus.

The radial motion of the torus generally leads to a redistribution of matter within it and, consequently, in changes of describing thermodynamical quantities. When the torus moves inward, closer to the central mass, it will compress and heat up, which will invoke an increase of its luminosity and size. Considering a small deviation from the equilibrium position r_0 we can estimate changes in the density profile, torus dimensions and the corresponding change in the overall luminosity.

The conditions in the torus centre are described by equations for the density (3.41), temperature (3.42) and by the polytropic equation of state (3.27), which can be expanded with respect to the enthalpy W. The expansion is allowed because W given by (3.43) is a small quantity ($\sim 10^{-2}$) in the slender approximation. In the second order, the formula (3.41) for the density becomes

$$\rho = \left(\frac{\gamma-1}{K\,\gamma}\,W\right)^{\frac{1}{\gamma-1}} \left[1 + \frac{1}{2\,(\gamma-1)}\,W + \mathcal{O}(W^2)\right] , \tag{4.7}$$

with a relative error of the order of 10^{-6}. The enthalpy W slightly varies on a cross-section in response to the periodic changes in the torus position $r(t)$. We denote its equilibrium value by $W_0(\varpi) \equiv W(r_0, \varpi)|_{R=R_0}$ and the perturbation due to the torus displacement by δW, so that

$$W(r, \varpi) = W_0(\varpi) + \delta W(r, \varpi) . \tag{4.8}$$

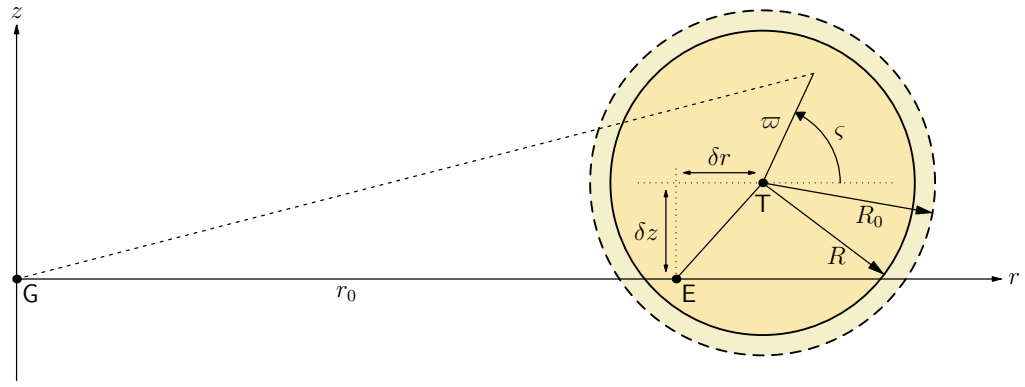

FIGURE 4.10: A schematic illustration of the torus displacement and of the describing variables. The centre T of the torus is shifted radially by δr and vertically by δz from its equilibrium position E, which is in the equatorial plane at the distance r_0 from the centre of gravity G. The displacement results in a compression or expansion of the fluid and in a corresponding change in the torus size. Dashed peripheral line marks the cross-section of the unperturbed torus at radius R_0, while the solid line marks the actual cross-section radius R at the new location.

Substituting to (4.7) and keeping only the first-order terms in δW we obtain

$$\begin{aligned}\rho &= \left(\frac{\gamma-1}{K\,\gamma}\,W_0\right)^{\frac{1}{\gamma-1}}\left[1+\frac{1}{2\,(\gamma-1)}\,W_0+\frac{1}{\gamma-1}\,\frac{\delta W}{W_0}+\mathcal{O}\!\left(\frac{\delta W^2}{W_0^2}\right)\right]\simeq\\ &\simeq\ \rho_0\left[1+\frac{1}{(\gamma-1)}\,\frac{\delta W}{W_0}\right]\,.\end{aligned}\tag{4.9}$$

The value of enthalpy at the torus centre is linked with the torus size by equation (3.43),

$$W(r,\,0)=\frac{(R_0+\delta R)^2}{B^2}=\frac{R_0^2}{B^2}\left(1+\frac{\delta R}{R_0}\right)^2\,,\tag{4.10}$$

where $\delta R(r)$ is the perturbation to the equilibrium radius R_0 on a cross-section and we define

$$B^2\equiv 2\,r_0^2\left(\frac{r_0}{r_{\rm g}}-3\right)\,.\tag{4.11}$$

From (4.9) and (4.10) we obtain a relation between the density perturbation and the perturbation of the torus size,

$$\left.\frac{\delta\rho}{\rho_0}\right|_{\varpi=0}=\frac{2}{\gamma-1}\,\frac{\delta R}{R_0}+\mathcal{O}\!\left(\frac{\delta R^2}{R_0^2}\right)\,.\tag{4.12}$$

The above formula has been calculated at the torus centre $\varpi=0$. It can be, however, extended to the whole cross-section, because from the definition of W follows that in the first order in δR

$$\frac{\delta W(r,\,0)}{W_0(0)}=\frac{\delta W(r,\,\varpi)}{W_0(\varpi)}=2\,\frac{\delta R(r)}{R_0}+\mathcal{O}\!\left(\frac{\delta R^2}{R_0^2}\right)\,.\tag{4.13}$$

For a small radial oscillation we can assume that δR is linearly proportional to the oscillation amplitude δr,

$$\delta R=\alpha\,\delta r\,,\tag{4.14}$$

thus the density perturbation is

$$\frac{\delta\rho}{\rho_0}=\frac{2\,\alpha}{\gamma-1}\,\frac{r_0}{R_0}\,\frac{\delta r}{r_0}\,.\tag{4.15}$$

The parameter α can be determined from the mass-conservation law. The total mass of the gas contained in the torus is

$$M=4\,\pi^2 r\int_0^{R(r)}\rho(\varpi)\,\varpi\,{\rm d}\varpi\,,\tag{4.16}$$

where the density profile $\rho(\varpi)$ on a cross-section is given by (3.41) with enthalpy (3.43).

Using (4.10) this can be integrated to

$$M(r) \simeq 2\,\pi^2\,\frac{\gamma-1}{\gamma}\,r\,R(r)^2\,\left(\frac{\gamma-1}{K\,\gamma}\,\frac{R(r)^2}{B}\right)^{\frac{1}{\gamma-1}}\,. \tag{4.17}$$

The total mass in the torus should conserve during the radial oscillations, meaning that $\mathrm{d}M/\,\mathrm{d}r = 0$. This condition gives

$$\alpha = -\,\frac{\gamma-1}{2\,\gamma}\,\frac{R_0}{r_0}\,. \tag{4.18}$$

The negative sign of α reflects the fact that the torus gets bigger when it gets closer to the centre. Going back to (4.15) we obtain the final expressions for the density and torus size perturbations,

$$\frac{\delta\rho}{\rho_0} = -\,\frac{1}{\gamma}\,\frac{\delta r}{r_0}\,, \tag{4.19}$$

$$\frac{\delta R}{R_0} = -\,\frac{\gamma-1}{2\,\gamma}\,\frac{\delta r}{r_0}\,. \tag{4.20}$$

Luminosity variance

The radial oscillation of the incompressible torus with a fixed size results in a corresponding variance of the volume, mass and luminosity (measured by a local observer orbiting with the fluid), linearly proportional to the actual distance of the torus $r(t)$ from the black hole,

$$L^{\circ}(t) \sim \int f\;\mathrm{d}V \sim r(t) \sim \delta r\,\sin(\omega_r t)\,. \tag{4.21}$$

In the compressible torus, the total mass is conserved and changes in the volume act against the perturbations of density, $\delta V \sim \delta\rho^{-1}$, so that the torus is blown up when compressed. The local luminosity changes with $r(t)$ too, but in a different way,

$$L^{\circ}(t) \sim \int f(\rho)\;\mathrm{d}V \sim \int_0^{R(r)} \rho^{7/3}\;\mathrm{d}V \sim r(t)^{-0.8}\,. \tag{4.22}$$

Note the opposite sign of the exponent, which causes a 'change of phase' in the luminosity response to the radial oscillation. The luminosity is increased when the torus moves closer to the black hole. This inversion has a significant impact on power spectrum.

Effect on power spectrum

Figures 4.6–4.9 (*right*) show how the power in the radial and vertical oscillation depends on model parameters if the torus is compressible. We can see that the power in the vertical oscillation stays unchanged, while the radial power is largely affected, particularly if inclination is changed. There is a clear difference between the *red* curve progression in the left and right panel in Figure 4.6. It is caused by the inversion of the luminosity

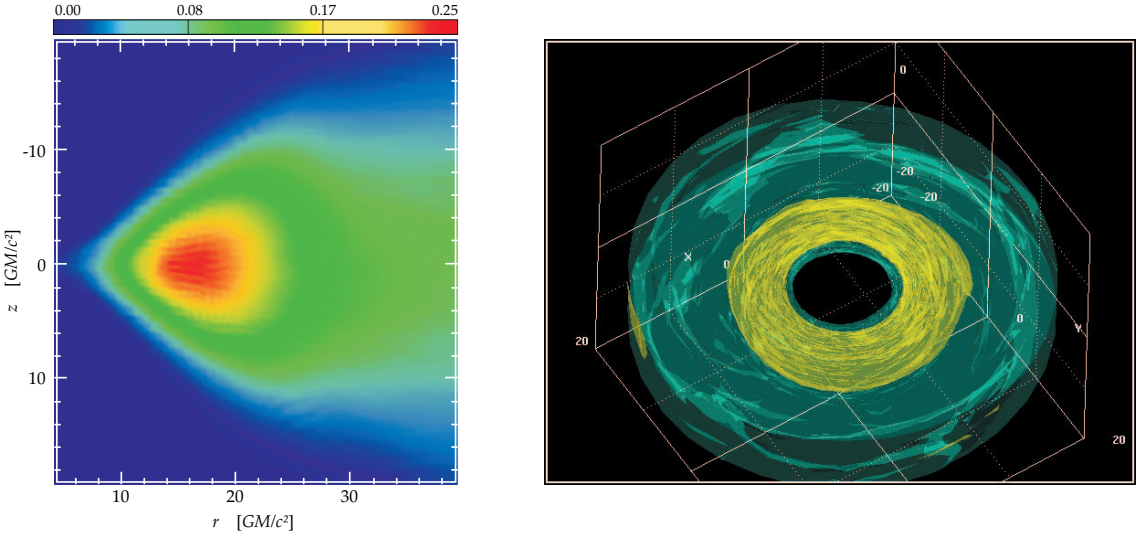

FIGURE 4.11: *Left*: The azimuthally averaged density distribution in the inner part of the simulated accretion flow. Due to the low efficiency of angular momentum transport, a small transient torus develops at $16\,r_{\rm g}$. *Right*: Isosurfaces of the density in a spatial view. The green and yellow contours correspond to $\rho = 0.2\,\rho_0$ and $\rho = 0.1\,\rho_0$ of the initial outer torus central density ρ_0, respectively. (Figures by M. Machida.)

dependence on the torus displacement, which in combination with the effect of g-factor (explained before in Section 4.4) results in a reverse trend of the ω_r power. A similar incidence can be found also in the other figures.

4.9 Comparison with numerical 3D MHD accretion flow simulations

In this section, the results obtained from our torus model are qualitatively compared with outputs of a three-dimensional global resistive magnetohydrodynamical (MHD) simulation of an optically thin accretion flow. This part of work has been done in a coopearation with M. Machida.

The initial state of the magnetohydrodynamical simulation is an equilibrium polytropic ($\gamma = {}^5\!/_3$) torus located at $r_0 = 70\,r_{\rm g}$ with a nearly Keplerian distribution of angular momentum, $L = L_0(r_0)\,(r/r_0)^{0.46}$. The torus is threaded by a weak toroidal magnetic field (Okada *et al.* 1989) with the initial gas to magnetic pressure ratio $\beta \simeq 100$. The presence of the strong gravitational field is simulated by using the pseudo-Newtonian potential (Paczyński & Wiita 1980) of a $10\,M_\odot$ black hole. The self-gravity of the gas and the radiative cooling are neglected.

The initial torus is lead to evolve and after several orbital periods the magnetic field is amplified by number of MHD instabilities together with the differential rotation. The

magnetorotational instability (MRI) driven turbulence develops and the torus deforms itself into an accretion disc by transporting angular momentum outwards by Maxwell stress. In the inner part, the matter accretes to the centre, while the disc is expanded radially by gaining some angular momentum in the outer part. The radial angular momentum distribution is very slightly sub-Keplerian, but because the efficiency of the angular momentum transport rate is $\alpha \lesssim 0.01$, it becomes almost constant in the region $10\,r_{\rm g} < r < 22\,r_{\rm g}$ and a small transitional constant angular momentum torus is created at about $16\,r_{\rm g}$ (Figure 4.11). The existence of such tori appears to be a robust feature of many global magnetohydrodynamic simulations (*c.f.* De Villiers *et al.* 2003).

The inner torus is an eccentric and time-varying structure. As a response to an event of enhanced mass accretion, a crescent-like density fluctuation develops in the torus sustained by a strong magnetic field. The fluctuation can persist several rotational periods, but is finally destroyed by a magnetic reconnection between the lower and higher density regions. The degree of eccentricity of the torus fluctuates in the response to variations in the mass accretion rate being more pronounced after an increased mass inflow and the development of the crescent. For further details of the simulation refer to Machida *et al.* (2004, 2005) and references therein.

The outputs of the simulation are used to analyse the X-ray emission from the inner region of the simulated accretion flow within $40\,r_{\rm g}$ from the central black hole. A continuous segment of 500 ms duration consisting of 100 frames is investigated after the development of the eccentric crescent fluctuation, which corresponds to about 25 orbital periods of the gas in the torus. Assuming the bremsstrahlung emissivity, the lightcurve and its Fourier power spectrum are calculated by ray-tracing photon trajectories from the emission region to the observer (Figure 4.12).

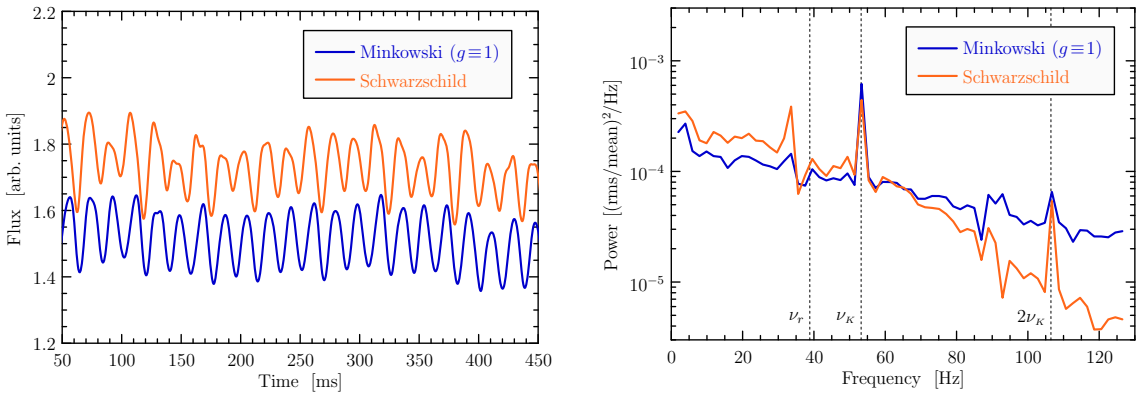

FIGURE 4.12: Sample lightcurves (*left*) and corresponding Fourier power spectra (*right*) from the inner region of the MHD simulation containing a transient torus. The viewing angle is 75° and cases both with and without inclusion of relativistic effects are shown. Dashed lines in the PDS graph mark the Keplerian orbital and radial epicyclic frequencies of free test particles in the Paczyński & Wiita potential.

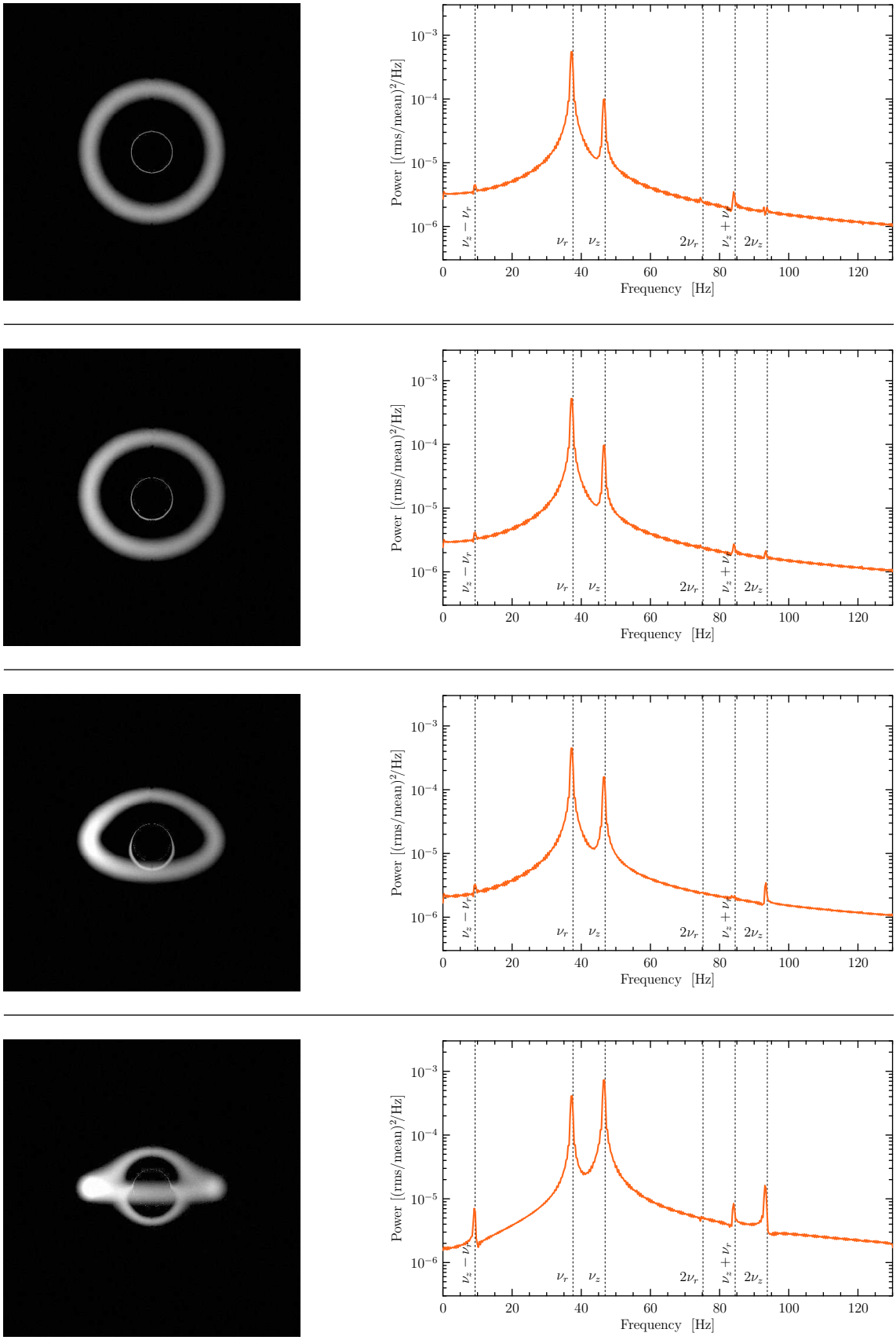

FIGURE 4.13: Instant snapshots and power spectra of a slender torus model at $16\,r_{\rm g}$ viewed from different positions (from top): 5°, 30°, 60° and 85°.

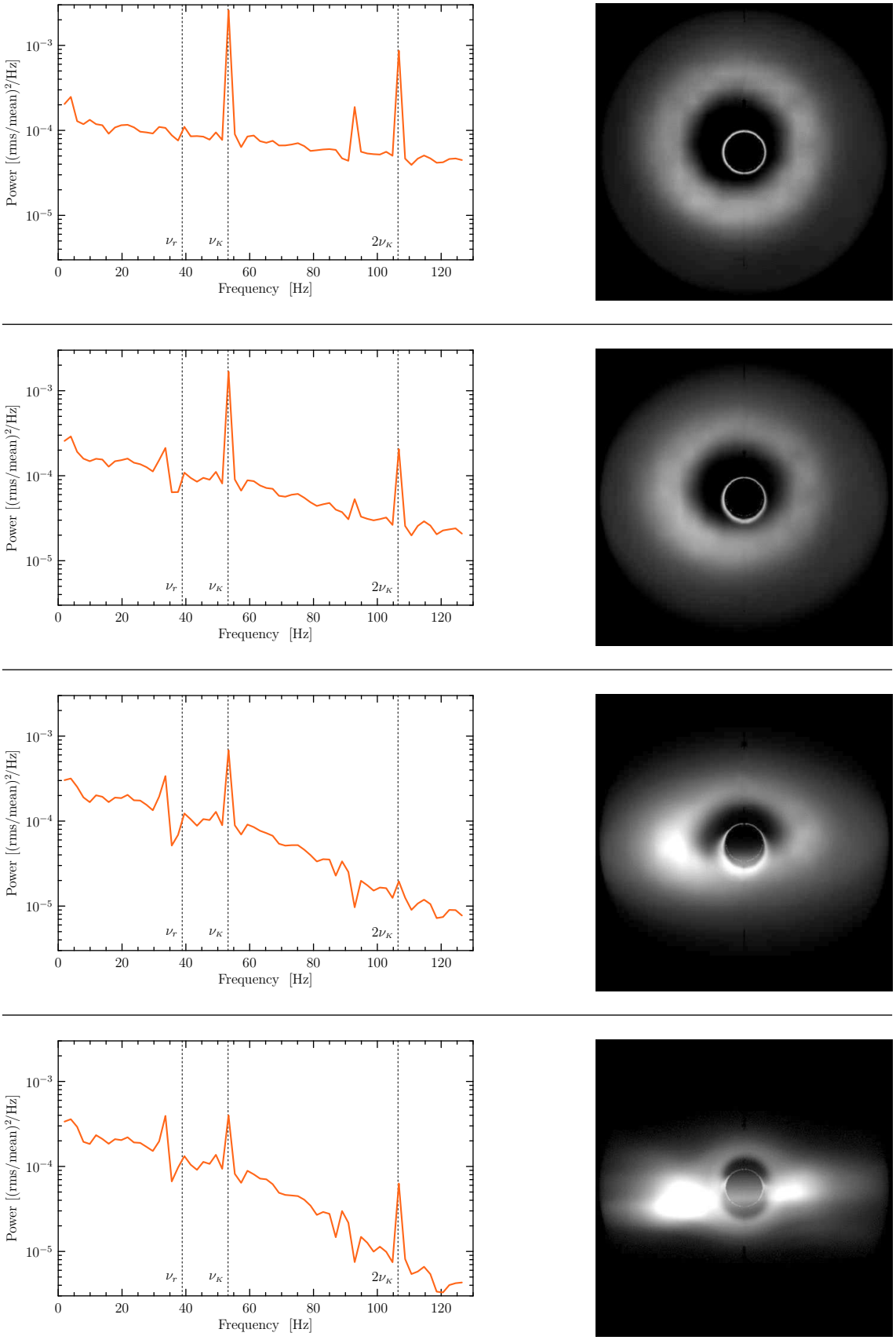

FIGURE 4.14: Instant snapshots and power spectra of a MHD accretion flow simullation by M, Machida viewed from different positions (from top): 5°, 30°, 60° and 85°.

The power spectrum typically shows three prominent features at frequencies 34 Hz, 53 Hz and 106 Hz. The strong 53 Hz and the 106 Hz oscillations clearly correspond to the Keplerian orbital frequency and to its first overtone in the Paczyński & Wiita potential, $\Omega_{\rm K}^{2\,({\rm PW})} = GM/[r(r-2\,r_{\rm g})^2]$. The identification of the 34 Hz oscillation is not that outright. It might correspond to the radial epicyclic oscillation, it may be some beat or it may represent some inertial mode. The radial epicyclic motion in the PW potential has the frequency $\omega_r^{({\rm PW})} = \Omega_{\rm K}^{({\rm PW})}\,[(r-6\,r_{\rm g})/(r-2\,r_{\rm g})]^{1/2}$, which is 39 Hz at the place of the torus. That is about 15% higher than the frequency of the peak in the observed PDS, but it should be noted that the expression is valid for a free test particle motion without an influence of additional forces. Conditions in the torus are strongly affected by the presence of magnetic and gas pressure, so it is quite possible that the actual epicyclic frequency is shifted by some factor (see also Blaes *et al.* 2006).

Figure 4.14 shows the resulting power spectra and instant snapshot images of the transient torus calculated for several different inclinations. They may be compared with similar panels in Figure 4.13, where power spectra and snapshots of a slender torus model are shown. The parameters of the model are chosen such that they resemble the size and distance of the torus in the MHD simulation. The model, however, stays axi-symmetric and oscillates radially and vertically at epicyclic frequencies, as it has been considered throughout this chapter. Despite of this difference, the power spectra reflect a similar pattern of changing power of different peaks depending on the observer's inclination. An additional similarity between the model and the simulated flow may be found, namely that the transient torus oscillates in the vertical direction as well, but not in the rigid mode as the model does. The vertical oscillation frequency is equal to the orbital frequency in the spherically symmetric spacetime, so that the vertical oscillation consequently tilts the torus a little off the equatorial plane. This effect may be seen in the bottom panel in Figure 4.14.

Summary and future prospects

The work presented in this thesis has focused on some aspects of high-frequency quasi-periodic oscillations observed in X-ray radiation coming from accreting neutron-star and black-hole binary sources.

In the case of neutron stars, it has been found that frequencies of the twin-peak oscillations are remarkably correlated among sources, and that this correlation can be described by a linear function. The same is valid if sources are considered individually; linear fits describe the individual frequency correlations with high accuracy, although in some cases a power law can be somewhat better option. Then we have found that the parameters of the linear fits, the slope and the shift, are anti-correlated, which means the source lines intersect close to a single point in the frequency–frequency plot. This point, notably, lies at the 3/2 line marked out by QPO observations from four black hole sources, which brings to attention a possible connection between the neutron-star and black-hole QPOs, and suggests the idea that they all may arise from acting of the same mechanism. Moreover, based on the intersections of source lines with the 3/2 line, neglecting magnetic field effects and assuming the general validity of the inverse mass scaling of QPO frequencies, it has been deduced that the two classes of neutron stars, atoll and Z sources, should differ in their masses by a few tens per cent.

A number of models try to explain the origination of QPOs. Among them, the epicyclic resonance model proposes a class of possible resonances between various combinations of frequencies connected with orbital motion. For each type of resonance, the model makes specific predictions about angular momentum of the three black-holes, whose masses are known. In the case of the source GRO J1655–40, for which also the angular momentum has been estimated recently, the model predictions can be compared with the measured spin estimates. It is found that currently none of the proposed resonances can satisfy the observational evidence. As a possible solution a new type of resonance is proposed and spins of the other two microquasars are predicted.

Then the focus has moved to a modulation mechanism of QPOs. In contrast with previous works, the importance of relativistic effects on light propagation in an optically thin medium is pointed out. A toy model is constructed containing a luminous torus filled with an optically thin gas in order to inspect a possibility of the observed flux modulation

by global oscillations of torus body. It is found that it is quite possible to modulate the observed signal at a sufficient level just by relativistic effects such as light bending, lensing, and time delays. Effects of changing viewing angle, torus size, position, and of a presence of an outer thin disc are examined. Namely the changing inclination and a close presence of the opaque disc is found capable to altering the distribution of power in the vertical and radial oscillation modes. It has been also shown that the g-factor and the torus response to the radial perturbations have a major impact on the observed PDS power in the radial oscillation mode, while power in the vertical mode oscillation is unaffected.

The above summarised results suggest that the origin of high-frequency QPOs may be found in the presence of a toroidal ADAF-type of accretion flow close to the marginally stable orbit. The simple torus model considered in this thesis has primarily served to demonstrate the principal possibility and importance of modulation of observed X-ray lightcurves by relativistic effects on light propagation. Future work should then follow three main directions:

Non-axisymmetric modes. Encouraged by the results of Chapter 2 that a resonance in an eccentric torus may be responsible for QPOs, and by outputs of MHD simulations also showing an eccentric transient torus, we would like to go beyond basic vertical and radial oscillations and explore also a non-axially symmetric cases with non-zero azimuthal wave number ($m > 0$).

Connection with MHD simulations. We plan to perform a ray-tracing from three-dimensional magneto-hydrodynamical simulations to quantify the correlation between intrinsic variations of local emissivity in the flow and their presentment to a distant observer. This work is already in progress and some results have already been presented in Chapter 4.

Spectral states. Some attempts has already been made to unify different spectral states of black-hole binaries (Esin *et al.* 1997) in terms of a model with a thin disc and an extended corona. We would like to follow up the idea, add spectral resolution to the ray-tracing code and simulate energy spectra of various configuration of a cool disc and a hot ADAF.

Appendix A

Frequencies of orbital motion in axially symmetric spacetimes

Free particles moving in an axially symmetric gravitational field of a black hole can generally exhibit three fundamental modes of periodic motion. These are: the Keplerian orbital motion, the radial epicyclic motion and the vertical epicyclic motion. Each mode has a corresponding frequency associated with (Nowak & Lehr 1998; Merloni *et al.* 1999).

The Keplerian motion is the motion of a free particle azimuthally orbiting a point mass. The frequency with which the particle completes full circles and passes through the same azimuthal position, as measured by an observer at infinity, is

$$\Omega_{\rm K}^2 = \left(\frac{G\,M}{r_{\rm g}^3}\right)\,\left(r^{3/2}+a\right)^{-2}\ . \tag{A.1}$$

For a $10\,M_\odot$ Schwarzchild black hole, it has approximately the value of 220 Hz at $r=6\,r_{\rm g}$ (the marginally stable orbit, see below).

The radial epicyclic motion is the oscillation about the original circular orbit of a free particle, if it is radially perturbed. Its frequency is given by the second derivative of the effective potential (see *e.g.* Abramowicz & Kluźniak 2004a) and reads

$$\omega_r^2 = \Omega_{\rm K}^2\,\left(1-\frac{6}{r}+\frac{8\,a}{r^{3/2}}-\frac{3\,a^2}{r^2}\right)\ . \tag{A.2}$$

In general relativity, there is a specific radius, where ω_r drops to zero and where orbits become unstable to radial perturbations. Particles, which pass beyond this point, cannot stay on circular orbits any more and fall freely down to the black hole. For a Schwarzchild black hole ($a=0$), this innermost marginally stable orbit is located at $r=6\,r_{\rm g}$ and move inwards with increasing a (Okazaki *et al.* 1987). In the Newtonian $1/r$ potential, all orbits

are stable and the radial epicyclic frequency is exactly equal to the Keplerian orbital frequency, which makes orbits around Newtonian bodies to be closed ellipses (Chandrasekhar 1995; Kepler 1609).

The vertical epicyclic motion is the oscillation about the original circular orbit of a free particle, if it is perturbed vertically. The corresponding frequency (again given by the second derivative of the effective potential) is

$$\omega_z^2 = \Omega_{\rm K}^2 \left(1 + \frac{4\,a}{r^{3/2}} + \frac{3\,a^2}{r^2}\right) . \tag{A.3}$$

In Newtonian potential and also in the gravitational field of a static black hole, it is exactly equal to the Keplerian orbital frequency.

There are yet two other frequencies connected with the motion of free particles, which are combinations of the fundamental ones: the periastron precession frequency and the Lense-Thirring frequency. In relativity, eccentric orbits undergo an angular precession in their lines of apsides. The frequency of this precession is

$$\omega_{\rm RP} = \Omega_{\rm K} - \omega_r . \tag{A.4}$$

Finally, the next frequency of particle motion not known in the Newtonian physics is the Lense-Thirring precession frequency. It is only present in the gravitational field of a black hole with a non-zero angular momentum. If an orbital plane of a particle is inclined with respect to the equatorial plane, it will start to precess due to the frame dragging effect of the spinning black hole with frequency (to the first order in a)

$$\omega_{\rm LT} = \Omega_{\rm K} - \omega_z \simeq 2a/r^3 . \tag{A.5}$$

Appendix B

The sim4 *code*

Introduction

In the past decade, missions such as XMM, RXTE, BeppoSAX and others have opened an X-ray window to the deep universe and allowed us to observe sources of energetic radiation in details we have never seen before. In many active galactic nuclei as well as in cataclysmic variables and low-mass X-ray binaries we observe rapid temporal changes of the flux (*e.g.* Leighly 2005; Woudt & Warner 2002; Strohmayer 2001; van der Klis 1997a) and of individual spectral features (Miller *et al.* 2002). In the widely accepted scenario, these sources contain a compact object surrounded by an accretion flow in the form of a disc or a torus (see *e.g.* Ulrich *et al.* 1997, van der Klis 2000). The strong gravity near these objects introduces distinctive deviations from Newtonian physics including bending of light rays, gravitational red shift and existence of the inner-most stable circular orbit. All these effects of general relativity affect profiles of observed light curves and have impact on the power spectra.

To address these issues a new three-dimensional modular ray-tracing code has been developed, which can be used to study light curve profiles and power spectra of luminous, spatially extensive astrophysical objects, such as thick accretion flows or tori, as well as radiation from 2D patterns, such as hot spots, belts, thin discs, *etc.*

Description of the code

Various numerical and semi-analytical approaches have been developed in order to tackle the problem of light ray-tracing in a curved spacetime. Some of them are focused on solving a special kind of problems, often they are limited to 2D geometry of a sphere or a disc. Therefore the need for a general, efficient and 3D ray-tracing computational tool has arised which motivates the development of a new code, called `sim4`.

`Sim4` is a parallel MPI/OpenMP modular ray-tracer written in the C language. It is modular in the sense that certain parts of the code (modules) can be easily modified or replaced. There are modules for a metric, a topology and for a model. Each module provides a small set of functions which are called by the core and to which a user may put its own implementation of a problem. This concept of modularity makes the code to be very versatile and powerful – with several changes in the code it is possible to turn focus to a completely different problems.

Ray-tracing

The code uses a method of direct ray-tracing outlined by Ftaclas *et al.* (1986) instead of the more frequently used transfer-function method (Cunningham 1975, 1976), as it is more convenient for the numerical calculations of radiative transport in the spatially extended emitters. The approximation of geometrical optics in a vacuum spacetime is adopted for calculations. The integration begins with division of the image plane into a number of pixels of equal solid angle on the observer's sky, each pixel corresponding to a single light ray. Following the method proposed by Rauch & Blandford 1994 and using given spacetime metric function, for each ray the code determines the initial position and 4-velocity and integrates the geodesic equation

$$\frac{\mathrm{d}^2 x^\mu}{\mathrm{d}\lambda^2} = -\Gamma^\mu_{\alpha\beta}\frac{\mathrm{d}x^\alpha}{\mathrm{d}\lambda}\frac{\mathrm{d}x^\beta}{\mathrm{d}\lambda} \tag{B.1}$$

back in time, *i.e.* from the observer to the source. Note that both in the above equation and throughout, geometrised units $G = c \equiv 1$ are used. This approach has the advantage that only photons which hit the target are actually integrated. On the other hand it puts a constraint on a metric function which must be stationary. Since in most astrophysical cases the distribution of matter is, in the first approximation, spherical, rays for not all pixels on the rectangular image plane are integrated, but only those which have impact parameter less than a certain value.

The determination of the gravitational lensing effect is performed by construction of two unit vectors U and V that, at the beginning, are perpendicular to the photon's 4-velocity and they are perpendicular to one another as well, so they enclose an area of a unit size. These vectors are transported along with the light ray by integrating the geodesic deviation equation if the form

$$\frac{\mathrm{d}^2 U^\mu}{\mathrm{d}\lambda^2} = -2\Gamma^\mu_{\alpha\beta}u^\alpha\frac{\mathrm{d}U^\beta}{\mathrm{d}\lambda} - \Gamma^\mu_{\alpha\beta,\gamma}u^\alpha u^\beta U^\gamma\ , \tag{B.2}$$

where u stands for the photon's 4-velocity, and the same equation for V. The lensing factor, defined as the ratio of the photon tube cross-section area in infinity and at the point of emission, is given by

$$l \equiv \frac{S_\mathrm{inf}}{S_\mathrm{em}} = \frac{1}{U \times V} = \frac{1}{\sqrt{U^\mu U_\mu \cdot V^\mu V_\mu - (U^\mu V_\mu)^2}}\ . \tag{B.3}$$

After certain number of integration steps the code collects the actual photon position, momentum and corresponding lensing factor, passes these information to the topology module which decides whether to save (and eventually dumps the data to an output file) and whether to stop the integration. It allows the user to specify exactly what data will be recorded and for how long the ray will be integrated. The recording condition can be either two or three dimensional and also allows to select several distinct regions. How often the data are recorded depends on chosen precision and also on the integration step. As the integration goes on, the code watches the step size and adjusts the saving frequency: when the step is small it saves more often, when it is large it saves less often and conserves resources.

All data are stored in the file which can be small or huge depending on the resolution, recording condition and chosen precision. This data file is then used to computation of the light curve and, in fact, if the recording condition is made general enough it can be reused many times even for completely different set of problems.

Light curve

In the next step the information from the photon data file is used to construct the light curve. The code reads the set of recorded points for each photon from the file and using the spline interpolation it reconstructs its whole trajectory. Then by making small spatial steps it follows the trajectory back in time from its end to where it starts and always asks the model module to return the amount of radiation flux (with respect to the observer at infinity) which is produced at that place. Knowing the time delay it can then determine the exact instant of time when this amount of flux reaches the observer.

The model module is where all the physics is stored and "where the radiation comes from". It can be as much complex and involve as much physics as one wish including access to external data (for instance from MHD simulations). An example of a possible model is given in the following section.

Visualisation

Visualisation is very similar process to construction a light curve and it follows almost the same procedure. The difference is that while to make a light curve we require very good time resolution and need no spatial resolution, to make an image or a movie we need no or little time resolution but require the information about spatial resolution. So instead of summing the flux carried by each photon to one number, the code records the numbers separately to corresponding pixels of the projection plane making an actual image of the observed object at that point of time.

Ray-tracing in the Schwarzschild spacetime

In spherical coordinates (t, r, θ, ϕ), the Schwarzschild metric is given by

$$\mathrm{d}s^2 = -\left(1 - \frac{2\,M}{r}\right)\,\mathrm{d}t^2 + \left(1 - \frac{2\,M}{r}\right)^{-1}\,\mathrm{d}r^2 + r^2\,(\,\mathrm{d}\theta^2 + \sin\theta^2\,\mathrm{d}\phi^2)\,. \tag{B.4}$$

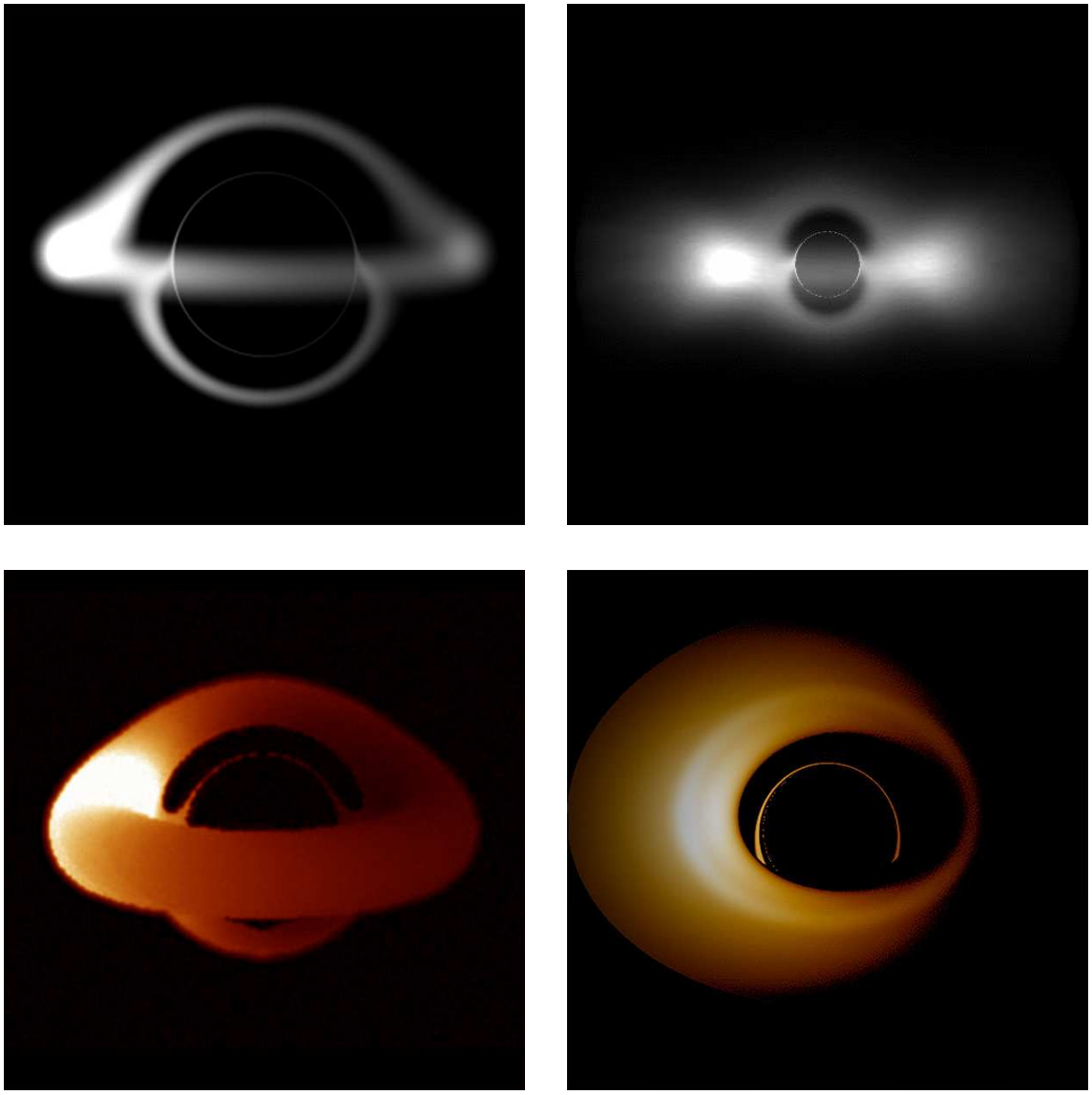

FIGURE B.1: Examples of the power of the ray-tracing code. The panels show models of an optically thin (*top, left*) and optically thick (*bottom, left*) torus, models of an torus embedded into a thin disc (*bottom, right*), and an output from a MHD simulation by M. Machida (*top, right*).

For the ray-tracing it is more convenient to use a modified coordinate system (t, u, m, ϕ), where $u = r^{-1}$ and $m = \cos\theta$. The line element then has the form

$$\begin{aligned} \mathrm{d}s^2 = &-(1 - 2\,M\,u)\;\mathrm{d}t^2 + \\ &u^{-4}(1 - 2\,M\,u)^{-1}\;\mathrm{d}u^2 + \\ &u^{-2}(1 - m^2)^{-1}\;\mathrm{d}m^2 + \\ &u^{-2}(1 - m^2)\;\mathrm{d}\phi^2\;. \end{aligned} \tag{B.5}$$

With this choice, the advantages are that the spatial infinity ($r \to \infty$) is represented by a finite value of u ($u \to 0$) and that the integration routine does not need to evaluate goniometric functions, which speeds up the calculations of photon trajectories.

The integration of geodesic equation starts with vectors for the initial position x^μ and momentum p^μ of a photon, which are chosen in the following way (*e.g.* Chandrasekhar 1983):

$$x^t = 0 \,, \tag{B.6a}$$
$$x^u = u_0 = 10^{-11} \,, \tag{B.6b}$$
$$x^m = m_0 = \cos i \,, \tag{B.6c}$$
$$x^\phi = 0 \,, \tag{B.6d}$$

$$p^t = 1 - 2\,u_0 \,, \tag{B.6e}$$
$$p^u = +\,u_0^2 \sqrt{R} \,, \tag{B.6f}$$
$$p^m = \pm\, u_0^2 \sqrt{M} \,, \tag{B.6g}$$
$$p^\phi = u_0^2 \,(1 - m_0^2)^{-1} \,, \tag{B.6h}$$

where i is the observer's inclination and R, M are given by the initial impact parameters α and β in the x–y image projection plane,

$$l^2 = \alpha^2 \sqrt{1 - m_0^2} \,, \tag{B.7a}$$
$$q^2 = \beta^2 + m_0^2\, \alpha^2 \,, \tag{B.7b}$$
$$R = 1 - (q^2 + l^2)\, u_0^2 + 2\,(l^2 + q^2)\, u_0^3 \,, \tag{B.7c}$$
$$M = q^2 - m_0^2\,(q^2 + l^2) \,. \tag{B.7d}$$

The sign of p^m is determined by the sign of β, being the opposite. For the geodesic deviation equation integration, two arbitrary vectors U^μ, V^μ are constructed perpendicular one another and to the initial 4-momentum vector p^μ as well. Their initial values are:

$$U^t = \beta\, u \,, \qquad V^t = \alpha\, u \,, \tag{B.8a}$$
$$U^u = \beta\, u^3 \,, \qquad V^u = \alpha\, u^3 \,, \tag{B.8b}$$
$$U^m = -u \sqrt{1 - m^2} \,, \qquad V^m = -\alpha\, u^2 \sqrt{1 - m^2} \,, \tag{B.8c}$$
$$U^\phi = -\alpha\, u^2\, m / \sqrt{1 - m^2} \,, \qquad V^\phi = u / \sqrt{1 - m^2} \,. \tag{B.8d}$$

And the initial values of their derivations ($\mathrm{d}/\,\mathrm{d}\lambda = p^\mu\, \partial/\partial x^\mu$) are:

$$\mathrm{d}U^t/\,\mathrm{d}\lambda = \beta\, u^2 \,, \qquad \mathrm{d}V^t/\,\mathrm{d}\lambda = \alpha\, u^2 \,, \tag{B.9a}$$
$$\mathrm{d}U^u/\,\mathrm{d}\lambda = 3\,\beta\, u^4 \,, \qquad \mathrm{d}V^u/\,\mathrm{d}\lambda = 3\,\alpha\, u^4 \,, \tag{B.9b}$$
$$\mathrm{d}U^m/\,\mathrm{d}\lambda = -u^2 \sqrt{1 - m^2} \,, \qquad \mathrm{d}V^m/\,\mathrm{d}\lambda = -2\,\alpha\, u^3\, m / \sqrt{1 - m^2} \,, \tag{B.9c}$$
$$\mathrm{d}U^\phi/\,\mathrm{d}\lambda = -2\,\alpha\, u^3 \sqrt{1 - m^2} \,, \qquad \mathrm{d}V^\phi/\,\mathrm{d}\lambda = u^2 / \sqrt{1 - m^2} \,. \tag{B.9d}$$

Appendix C

Lightcurve analysis and PDS normalisation

The product of the numerical ray-tracing is a lightcurve, which describes the flux seen by a distant observer at equally spaced time bins. The amount of flux coming to the observer in each time bin can be think of as a number of photon counts collected by a detector per the binning interval. To quantify periodicities in the signal, the lightcurve is Fourier transformed to the frequency domain. The procedure used for Fourier analysis of computed lightcurves closely follow the method, which is actually used in the analysis of real observed data (van der Klis 1997b).

A continuous segment of a lightcurve of length T is binned into $N = 2^m$ time bins, where the $k^{\rm th}$ bin contains x_k counts. The Fast Fourier Transform is being performed on the lightcurve, giving a series of frequency amplitudes

$$a_j = \sum_{k=0}^{N-1} x_k e^{i\omega_j t_k} \ , \quad t_k = k\,T/N \ . \tag{C.1}$$

The power spectrum P_j corresponding to statistically independent frequencies $\omega_j = 2\pi j/T$, $j = 0..N/2$ is defined as

$$P_j = \frac{2}{a_0}|a_j|^2 \ , \quad j = 0..N/2 \ , \tag{C.2}$$

Note that $a_0 = \sum_0^{N-1} x_k = N_{\rm ph}$ is the total number of photons detected over the period T, *i.e.* it gives the total observed flux. A normalisation is used, where Fourier powers P_j are given as $Q_j \equiv P_j/\lambda$, where $\lambda = N_{\rm ph}/T$ is the average 'count rate'. With this

normalisation, the sum of powers over all frequency bins multiplied by the width of the bins $\Delta\nu = 1/T$ is

$$\sum_{j=0}^{N/2} Q_j \Delta\nu = \frac{2}{a_0^2} \sum_{j=0}^{N/2} |a_j|^2 = \frac{1}{a_0^2} \left(\sum_{j=0}^{N-1} |a_j|^2 - a_0^2 \right) . \tag{C.3}$$

The fractional root-mean-square of the variability is defined as

$$\mathrm{frms} = \frac{\sqrt{\frac{1}{N} \sum_{k=0}^{N-1} (x_k - \bar{x})^2}}{\bar{x}} , \tag{C.4}$$

where $\bar{x}$ stands for the mean value of the time series,

$$\bar{x} = \frac{1}{N} \sum_{k=0}^{N-1} x_k = \frac{a_0}{N} . \tag{C.5}$$

The squared value of the fractional root mean square amplitude is

$$\mathrm{frms}^2 = \frac{N}{a_0^2} \sum_{k=0}^{N-1} |x_k|^2 - 1 , \tag{C.6}$$

to which the Parseval's theorem may be applied,

$$\sum_{0}^{N-1} |x_k|^2 = \frac{1}{N} \sum_{-N/2}^{N/2} |a_j|^2 , \tag{C.7}$$

and we arrive to

$$\mathrm{frms}^2 = \frac{1}{a_0^2} \left(\sum_{j=0}^{N-1} |a_j|^2 - a_0^2 \right) . \tag{C.8}$$

The last formula is identical with the equation (C.3) so that the integral over frequencies of the normalised Fourier power spectrum gives the square of the fractional rms amplitude of the original time series variability. The physical unit of Q_j is [(rms/mean)^2/Hz], where 'rms/mean' is just frms.

Appendix D

Frequency-frequency correlations from RXTE data

For the purpose of the linear fits analysis presented in Section 1.6, a set of frequency pairs has been used, which was extracted from *RXTE* data archives. All science event files were retrieved from the archives up to the end of 2004 for six atoll sources: 4U 1636−536, 4U 1608−522, 4U 1820−303, 4U 1735−44, 4U 0614+09 and 4U 1728−34. The analysis was done by D. Barret, who kindly imparted the data to me, and its description follows:

Files are considered as they can be obtained from the archives. They are identified with their Obs-IDs following the RXTE convention. An Obs-ID identifies a temporally contiguous collection of data from a single pointing. Only files with time resolution better than or equal to 250 microseconds and exposure times larger than 600 seconds are considered. No filtering on the raw data is performed, which means that all photons are used in the analysis, only type I X-ray bursts and data gaps are removed from the files.

For each Obs-ID, Leahy normalised Fourier power density spectra (PDS) is computed between 1 and 2048 Hz over 8 s intervals (with a 1 Hz resolution). A Fourier Power spectrum averaged over the file is first computed. The file averaged PDS is then searched for a QPO using a scanning technique which looks for peak excesses above the Poisson counting noise level (see Boirin *et al.* 2000). No fit is performed at this stage as the scanning procedures returns the QPO peak frequency and an approximation of its full width zero maximum. In case of the presence of two peaks, the one with the highest significance is considered. Then a window is defined of 25 Hz width around the QPO profile, and a recursive search algorithm is applied a to define the shortest time interval over which the QPO is detected over $4\,\sigma$ (still above the Poisson counting noise level). Specifically, starting from an interval of duration T with a QPO at frequency ν_0, the interval is divided in two parts of equal durations $T/2$ and search for a QPO between $\nu_0 - 25$ and $\nu_0 + 25$. The procedure is repeated updating continuously the window for the search, using the information obtained at the lower time resolution. All 8 second PDS within the time interval T are attributed the same QPO frequency. It has been checked

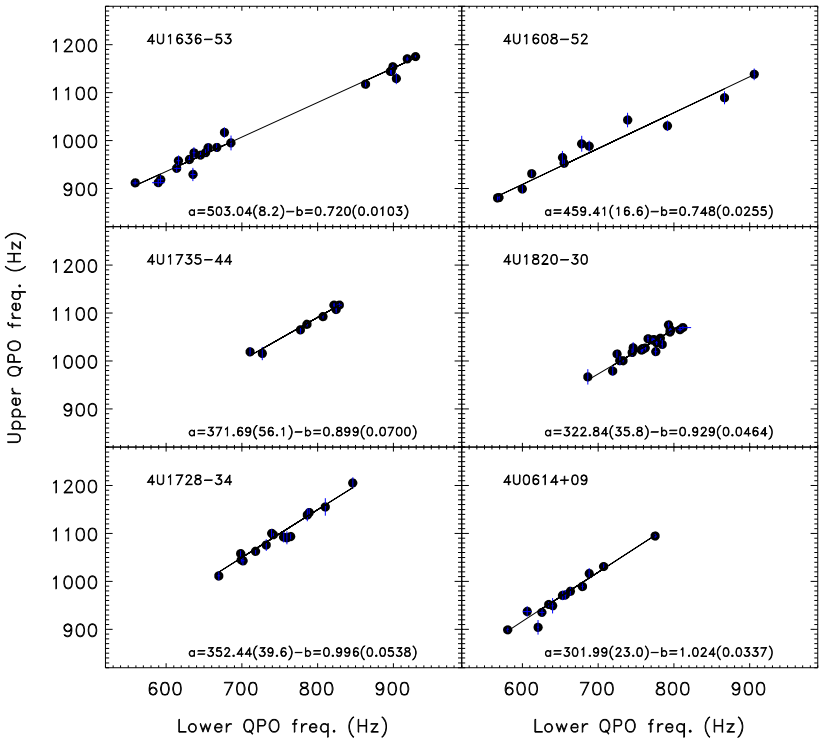

FIGURE D.1: The frequency−frequency correlations and their linear fits for the six analysed sources. (Adopted from Abramowicz *et al.* 2006.)

through simulations of a QPO signal of varying frequency and similar amplitude as in the real data, that this procedure follows with great accuracy the changes in frequency. The individual file can then be summarised as a list of QPO frequencies, estimated every 8 seconds.

At this stage, it is not known whether the QPO, which is followed, is the upper or the lower QPO. Within a file, the individual 8 second PDS is shifted-and-added to the mean QPO frequency over the file. The power spectrum so obtained is then searched for a second QPO peak using the same scanning as above. The PDS are then converted in a format readable by the XSPEC 11.3.2 spectral package. The procedure takes advantage of the robustness of the XSPEC fitting procedures (including the error computations), and the ease of the Tcl interface to access the fitted parameters. The QPOs are then fitted each with a Lorentzian of three parameters (frequency, full width at half maximum, and normalisation) to which a constant is added to account for the counting noise level (close to 2.0 in a Leahy normalised PDS).

Next, only those QPOs are kept, which are detected above $2.5\,\sigma$ (the significance being then defined as the integral of the Lorentzian divided by its error), above 500 Hz, with a quality factor larger than 3. The results of this selection is shown in Figure D.1 for all six sources together with their linear fits. The results of the fits are given in Table 1.3.

References

Abramowicz, M. A. (2005b). Proceedings of the Nordita Workdays on QPOs, editor M. Abramowicz, Astronomische Nachrichten 326 (Cited on page 44.)

Abramowicz, M. A., Barret, D., Bursa, M., Horák, J., Kluźniak, W., Rebusco, P., Török, G. (2005a). *The correlations and anticorrelations in QPO data*, Astronomische Nachrichten 326, 864–866 (ADS) (Cited on pages 12 and 15.)

Abramowicz, M. A., Barret, D., Bursa, M., Horák, J., Kluźniak, W., Rebusco, P., Török, G. (2005b). *A Note on the slope–shift anticorrelation in the neutron star kHz QPOs data*, Proc. of RAGtime 6/7: Workshops on black holes and neutron stars, eds. S. Hledík, Z. Stuchlík, Silesian University in Opava, in press (Cited on pages 12 and 15.)

Abramowicz, M. A., Barret, D., Bursa, M., Horák, J., Kluźniak, W., Rebusco, P., Török, G. (2006). *The slope–shift anti correlation in linear frequency–frequency fits of neutron stars twin peak kHz QPOs*, in preparation (Cited on pages 12, 38 and 106.)

Abramowicz, M. A., Blaes, O. M., Horák, J., Kluźniak, W., & Rebusco, P. (2005c). *Epicyclic oscillations of fluid bodies Paper II. Strong gravity*, Classical and Quantum Gravity, in press arXiv:astro–ph/0511375 (ADS) (Cited on pages 54, 61 and 71.)

Abramowicz, M. A., Bulik, T., Bursa, M., & Kluźniak, W. (2003). *Evidence for a 2:3 resonance in Sco X-1 kHz QPOs*, A&A 404, L21–L24 (ADS) (Cited on pages 12, 15, 23 and 37.)

Abramowicz, M. A., Chen, X.-M., Granath, M., & Lasota, J.-P. (1996). *Advection-dominated Accretion Flows around Kerr Black Holes*, ApJ 471, 762–773 (ADS) (Cited on page 64.)

Abramowicz, M., Jaroszynski, M., & Sikora, M. (1978). *Relativistic, accreting disks*, A&A 63, 221–224 (ADS) (Cited on page 55.)

Abramowicz, M. A. & Kluźniak, W. (2004a). *Epicyclic frequencies derived from the effective potential: simple and practical formulae.*, Lecture at the conference "From X-ray Binaries to Quasars: Black Hole Accretion on All Mass Scales", 13–15 July 2004, Amsterdam arXiv:astro–ph/0411709 (Cited on pages 57, 60 and 95.)

Abramowicz, M. A., & Kluźniak, W. (2004b). *Interpreting black hole QPOs*, AIP Conf. Proc. 714: X-ray Timing 2003: Rossi and Beyond 714, 21–28 (ADS) (Cited on page 44.)

Abramowicz, M. A., Kluźniak, W., Stuchlík, Z., & Török, G. (2004). *Twin peak QPOs frequencies in microquasars and Sgr A*. The resonance and other orbital models*, Proc. of RAGtime 4/5: Workshops on black holes and neutron stars, eds. S. Hledík, Z. Stuchlík, Silesian University in Opava (ADS) (Cited on pages 44 and 45.)

Aschenbach, B. (2004). *Measuring mass and angular momentum of black holes with high-frequency quasi-periodic oscillations*, A&A 425, 1075–1082 (ADS) (Cited on page 21.)

Aschenbach, B., Grosso, N., Porquet, D., & Predehl, P. (2004). *X-ray flares reveal mass and angular momentum of the Galactic Center black hole*, A&A 417, 71–78 (ADS) (Cited on page 21.)

Alpar, M. A., Cheng, A. F., Ruderman, M. A., & Shaham, J. (1982). *A new class of radio pulsars*, Nature 300, 728–730 (ADS) (Cited on page 15.)

Alpar, M. A., & Shaham, J. (1985). *Is GX5 - 1 a millisecond pulsar?*, Nature 316, 239–241 (ADS) (Cited on page 41.)

Bardeen, J. M. (1973). Black Holes, Gordon and Breach, New York (Cited on page 56.)

Belloni, T., Méndez, M., & Homan, J. (2005). *The distribution of kHz QPO frequencies in bright low mass X-ray binaries*, A&A 437, 209–216 (ADS) (Cited on pages 16, 23, 25 and 37.)

Blaes, O. M. (1985). *Oscillations of slender tori*, MNRAS 216, 553–563 (ADS) (Cited on pages 54, 60 and 61.)

Blaes, O. M., Abramowicz, M. A., Kluźniak, W. & Šrámková, E. (2006). in preparation (Cited on pages 49, 54, 61 and 88.)

Boirin, L., Barret, D., Olive, J. F., Bloser, P. F., & Grindlay, J. E. (2000). *Low and high frequency quasi-periodic oscillations in 4U1915-05*, A&A 361, 121–138 (ADS) (Cited on page 105.)

Bursa, M. (2004). *Variability of accreting sources at very high time resolution*, Proc. of RAGtime 4/5: Workshops on black holes and neutron stars, eds. S. Hledík, Z. Stuchlík, Silesian University in Opava (ADS) (Cited on pages 12 and 54.)

Bursa, M. (2005). *Global oscillations of a fluid torus as a modulation mechanism for black-hole high-frequency QPOs*, Astronomische Nachrichten 326, 849–855 (ADS) (Cited on pages 12 and 70.)

Bursa, M. (2006). *High-frequency QPOs in GRO J1655–40: Constraints on resonance models by spectral fits*, submitted to ApJ (Cited on pages 12 and 43.)

Bursa, M., Abramowicz, M. A., Karas, V., & Kluźniak, W. (2004). *The Upper Kilohertz Quasi-periodic Oscillation: A Gravitationally Lensed Vertical Oscillation*, ApJ 617, L45–L48 (ADS) (Cited on pages 12 and 70.)

Casares, J., Zurita, C., Shahbaz, T., Charles, P. A., & Fender, R. P. (2004). *Evidence of a Black Hole in the X-Ray Transient GS 1354-64 (=BW Circini)*, ApJ 613, L133–L136 (ADS) (Cited on page 43.)

Chandrasekhar, S. (1960). Radiative Transfer, Dover, New York (Cited on page 60.)

Chandrasekhar, S. (1983). The mathematical theory of black holes, Oxford Univ. Press, New York (Cited on page 101.)

Chandrasekhar, S. (1995). Newton's Principia for the common reader, Oxford Univ. Press, Oxford (Cited on page 96.)

Crary, D. J., Finger, M. H., Kouveliotou, C., van der Hooft, F., van der Klis, M., Lewin, W. H. G., & van Paradijs, J. (1998). *Hard X-Ray Lags in Cygnus X-1*, ApJ 493, L71–L74 (ADS) (Cited on page 17.)

Cunningham, C. T. (1975). *The effects of redshifts and focusing on the spectrum of an accretion disk around a Kerr black hole*, ApJ 202, 788–802 (ADS) (Cited on pages 65 and 98.)

Cunningham, C. (1976). *Returning radiation in accretion disks around black holes.*, ApJ 208, 534–549 (ADS) (Cited on pages 65 and 98.)

Davis, S. W., Blaes, O. M., Hubeny, I., & Turner, N. J. (2005). *Relativistic Accretion Disk Models of High-State Black Hole X-Ray Binary Spectra*, ApJ 621, 372–387 (ADS) (Cited on pages 43 and 47.)

De Villiers, J.-P., Hawley, J. F., & Krolik, J. H. (2003). *Magnetically Driven Accretion Flows in the Kerr Metric. I. Models and Overall Structure*, ApJ 599, 1238–1253 (ADS) (Cited on page 85.)

Di Salvo, T., Méndez, M., van der Klis, M., Ford, E., & Robba, N. R. (2001). *Study of the Temporal Behavior of 4U 1728-34 as a Function of Its Position in the Color-Color Diagram*, ApJ 546, 1107–1120 (ADS) (Cited on pages 27 and 38.)

Dovčiak, M. (2004). *Radiation of Accretion Discs in Strong Gravity*, PhD thesis arXiv:astro–ph/0411605 (Cited on page 66.)

Esin, A. A., McClintock, J. E., & Narayan, R. (1997). *Advection-dominated Accretion and the Spectral States of Black Hole X-Ray Binaries: Application to Nova MUSCAE 1991*, ApJ 489, 865–889 (ADS) (Cited on page 92.)

Esin, A. A., Narayan, R., Cui, W., Grove, J. E., & Zhang, S.-N. (1998). *Spectral Transitions in Cygnus X-1 and Other Black Hole X-Ray Binaries*, ApJ 505, 854–868 (ADS) (Cited on page 53.)

Fishbone, L. G., & Moncrief, V. (1976). *Relativistic fluid disks in orbit around Kerr black holes*, ApJ 207, 962–976 (ADS) (Cited on page 55.)

Ford, E. C., van der Klis, M., van Paradijs, J., Méndez, M., Wijnands, R., & Kaaret, P. (1998). *Discovery of a Second Kilohertz QPO in the X-Ray Binary 4U 1735-44*, ApJ 508, L155–L158 (ADS) (Cited on page 38.)

Ftaclas, C., Kearney, M. W., & Pechenick, K. (1986). *Hot spots on neutron stars. II - The observer's sky*, ApJ 300, 203–208 (ADS) (Cited on pages 65 and 98.)

Genzel, R., Schödel, R., Ott, T., Eckart, A., Alexander, T., Lacombe, F., Rouan, D., & Aschenbach, B. (2003). *Near-infrared flares from accreting gas around the supermassive black hole at the Galactic Centre*, Nature 425, 934–937 (ADS) (Cited on page 21.)

Ghez, A. M., Salim, S., Hornstein, S. D., Tanner, A., Lu, J. R., Morris, M., Becklin, E. E., & Duchêne, G. (2005). *Stellar Orbits around the Galactic Center Black Hole*, ApJ 620, 744–757 (ADS) (Cited on page 21.)

Gilfanov, M., & Revnivtsev, M. (2005). *Boundary layer emission in luminous LMXBs*, Astronomische Nachrichten 326, 812–819 (ADS) (Cited on page 53.)

Gilfanov, M., Revnivtsev, M., & Molkov, S. (2003). *Boundary layer, accretion disk and X-ray variability in the luminous LMXBs*, A&A 410, 217–230 (ADS) (Cited on pages 17 and 53.)

Greene, J., Bailyn, C. D., & Orosz, J. A. (2001). *Optical and Infrared Photometry of the Microquasar GRO J1655-40 in Quiescence*, ApJ 554, 1290–1297 (ADS) (Cited on page 51.)

Greiner, J., Cuby, J. G., & McCaughrean, M. J. (2001). *An unusually massive stellar black hole in the Galaxy*, Nature 414, 522–525 (ADS) (Cited on page 51.)

Grove, J. E., Johnson, W. N., Kroeger, R. A., McNaron-Brown, K., Skibo, J. G., & Phlips, B. F. (1998). *Gamma-Ray Spectral States of Galactic Black Hole Candidates*, ApJ 500, 899–909 (ADS) (Cited on page 18.)

Hasinger, G., & van der Klis, M. (1989). *Two patterns of correlated X-ray timing and spectral behaviour in low-mass X-ray binaries*, A&A 225, 79–96 (ADS) (Cited on pages 17 and 27.)

Homan, J., van der Klis, M., Jonker, P. G., Wijnands, R., Kuulkers, E., Méndez, M., & Lewin, W. H. G. (2002). *RXTE Observations of the Neutron Star Low-Mass X-Ray Binary GX 17+2: Correlated X-Ray Spectral and Timing Behavior*, ApJ 568, 878–900 (ADS) (Cited on pages 27 and 38.)

in't Zand, J. J. M., et al. (2001). *The first outburst of SAX J1808.4-3658 revisited*, A&A 372, 916–921 (ADS) (Cited on page 17.)

Jaroszyński, M., Abramowicz, M. A., & Paczyński, B. (1980). *Supercritical accretion disks around black holes*, Acta Astronomica 30, 1–34 (ADS) (Cited on page 59.)

Jonker, P. G., et al. (2000a). *The Power Spectral Properties of the Z Source GX 340+0*, ApJ 537, 374–386 (ADS) (Cited on pages 27 and 38.)

Jonker, P. G., Méndez, M., & van der Klis, M. (2000b). *Discovery of a New, Third Kilohertz Quasi-periodic Oscillation in 4U 1608-52, 4U 1728-34, and 4U 1636-53: Sidebands to the Lower Kilohertz Quasi-periodic Oscillation?*, ApJ 540, L29–L32 (ADS) (Cited on pages 27 and 38.)

Jonker, P. G., Méndez, M., & van der Klis, M. (2002a). *Kilohertz quasi-periodic oscillations difference frequency exceeds inferred spin frequency in 4U 1636-53*, MNRAS 336, L1–L5 (ADS) (Cited on pages 27 and 38.)

Jonker, P. G., van der Klis, M., Homan, J., Méndez, M., Lewin, W. H. G., Wijnands, R., & Zhang, W. (2002b). *Low- and high-frequency variability as a function of spectral properties in the bright X-ray binary GX 5-1*, MNRAS 333, 665–678 (ADS) (Cited on pages 27 and 38.)

Karas, V. (1999). *Quasi-Periodic Features Due to Clumps Orbiting around a Black Hole*, PASJ 51, 317–320 (ADS)

Kato, S. (2004). *Resonant Excitation of Disk Oscillations by Warps: A Model of kHz QPOs*, PASJ 56, 905–922 (ADS) (Cited on page 69.)

Kepler, J. (1609). Astronomia Nova. Physica coelestis, tradita commentariis De motibus stellae Martis, ex observationibus G. V. Tychonis Brahe. Pragæ (Cited on page 96.)

King, A. R., Davies, M. B., Ward, M. J., Fabbiano, G., & Elvis, M. (2001). *Ultraluminous X-Ray Sources in External Galaxies*, ApJ 552, L109–L112 (ADS) (Cited on page 21.)

Kluźniak, W., & Abramowicz, M. A. (2000). *The physics of kHz QPOs—strong gravity's coupled anharmonic oscillators*, arXiv:astro–ph/0105057 (Cited on pages 44 and 69.)

Kluźniak, W., & Abramowicz, M. A. (2003). *Millisecond oscillators in accreting neutron stars and black holes*, arXiv:astro–ph/0304345 (ADS) (Cited on page 47.)

Kozlowski, M., Jaroszynski, M., & Abramowicz, M. A. (1978). *The analytic theory of fluid disks orbiting the Kerr black hole*, A&A 63, 209–220 (ADS) (Cited on pages 55 and 56.)

Kuwahara, F. (1988). *Relativistic Accretion Tori around Schwarzschild Black Holes*, Progress of Theoretical Physics 80, 449–467 (ADS) (Cited on page 55.)

Leighly, K. M. (2005). *X-RAY Periodicity in AGN*, Ap&SS 300, 137–142 (ADS) (Cited on page 97.)

Lee, H. C., Misra, R., & Taam, R. E. (2001). *A Compton Upscattering Model for Soft Lags in the Lower Kilohertz Quasi-periodic Oscillation in 4U 1608-52*, ApJ 549, L229–L232 (ADS) (Cited on page 17.)

Lewin, W. H. G., van Paradijs, J., & Taam, R. E. (1993). *X-Ray Bursts*, Space Science Reviews 62, 223 (ADS) (Cited on page 41.)

Li, L.-X., Zimmerman, E. R., Narayan, R., & McClintock, J. E. (2005). *Multi-temperature Blackbody Spectrum of a Thin Accretion Disk around a Kerr Black Hole: Model Computations and Comparison with Observations*, ApJS 157, 335–370 (ADS) (Cited on page 47.)

Linares, M., van der Klis, M., Altamirano, D., & Markwardt, C. B. (2005). *Discovery of Kilohertz Quasi-periodic Oscillations and Shifted Frequency Correlations in the Accreting Millisecond Pulsar XTE J1807-294*, ApJ 634, 1250–1260 (ADS) (Cited on page 17.)

Maccarone, T. J. (2002). *On the misalignment of jets in microquasars*, MNRAS 336, 1371–1376 (ADS) (Cited on page 49.)

Machida, M., Nakamura, K., & Matsumoto, R. (2004). *Global Structures of Optically Thin Black Hole Accretion Flows Obtained from Direct Magnetohydrodynamic Simulations*, PASJ 56, 671–679 (ADS) (Cited on page 85.)

Machida, M., Nakamura, K., & Matsumoto, R. (2005). *Formation of Magnetically Supported Disks During Hard-to-Soft Transition in Black Hole Accretion Flows*, PASJ in press, arXiv:astro–ph/0105057 (ADS) (Cited on page 85.)

Madej, J., & Paczyński, B. (1977). *Disk Structure in U Geminorum*, IAU Colloq. 42: The Interaction of Variable Stars with their Environment, 313 (ADS) (Cited on page 54.)

McClintock, J. E., & Remillard, R. A. (2005). *Black Hole Binaries*, Compact Stellar X-ray Sources, eds. W.H.G. Lewin and M. van der Klis, Cambridge University Press arXiv:astro–ph/0306213 (Cited on pages 18, 20, 21, 23 and 43.)

Méndez, M., et al. (1998). *Discovery of a Second KHZ QPO Peak in 4U 1608-52*, ApJ 494, L65–L69 (ADS) (Cited on page 24.)

Méndez, M., van der Klis, M., & Ford, E. C. (2001). *The Amplitude of the Kilohertz Quasi-periodic Oscillations in 4U 1728-34, 4U 1608-52, and Aquila X-1, as a Function of X-Ray Intensity*, ApJ 561, 1016–1026 (ADS) (Cited on page 16.)

Méndez, M., van der Klis, M., Ford, E. C., Wijnands, R., & van Paradijs, J. (1999). *Dependence of the Frequency of the Kilohertz Quasi-periodic Oscillationson X-Ray Count Rate and Colors in 4U 1608-52*, ApJ 511, L49–L52 (ADS) (Cited on page 16.)

Méndez, M., van der Klis, M., van Paradijs, J., Lewin, W. H. G., Lamb, F. K., Vaughan, B. A., Kuulkers, E., & Psaltis, D. (1997). *Kilohertz Quasi-periodic Oscillation and Atoll Source States in 4U 0614+09*, ApJ 485, L37 (ADS) (Cited on page 24.)

Merloni, A., Vietri, M., Stella, L., & Bini, D. (1999). *On gravitomagnetic precession around black holes*, MNRAS 304, 155–159 (ADS) (Cited on pages 44 and 95.)

Miller, J. M., et al. (2001). *High-Frequency Quasi-Periodic Oscillations in the 2000 Outburst of the Galactic Microquasar XTE J1550-564*, ApJ 563, 928–933 (ADS) (Cited on page 19.)

Miller, J. M., et al. (2002). *Resolving the Composite Fe Kα Emission Line in the Galactic Black Hole Cygnus X-1 with Chandra*, ApJ 578, 348–356 (ADS) (Cited on page 97.)

Miller, M. C., Lamb, F. K., & Psaltis, D. (1998). *Sonic-Point Model of Kilohertz Quasi-periodic Brightness Oscillations in Low-Mass X-Ray Binaries*, ApJ 508, 791–830 (ADS) (Cited on page 24.)

Miniutti, G., Fabian, A. C., & Miller, J. M. (2004). *The relativistic Fe emission line in XTE J1650-500 with BeppoSAX: evidence for black hole spin and light-bending effects?*, MNRAS 351, 466–472 (ADS) (Cited on page 43.)

Mirabel, I. F., & Rodriguez, L. F. (1998). *Microquasars in our Galaxy.*, Nature 392, 673–676 (ADS) (Cited on page 21.)

Misner, C. W. , Thorne, K. S., Wheeler, J. A. (1973). Gravitation, W. H. Freeman, New York (Cited on page 55.)

Mucciarelli P., Casella P., Belloni T., Zampieri L., Ranalli P. (2005). *A variable Quasi-Periodic Ocillation in M82 X-1. Timing and spectral analysis of XMM-Newton and RossiXTE observations*, submitted to MNRAS arXiv:astro–ph/0509796 (Cited on page 21.)

Muno, M. P., Remillard, R. A., & Chakrabarty, D. (2002). *How Do Z and Atoll X-Ray Binaries Differ?*, ApJ 568, L35–L39 (ADS) (Cited on page 17.)

Narayan, R., Mahadevan, R., & Quataert, E. (1998). *Advection-dominated accretion around black holess*, Theory of Black Hole Accretion Disks 148 (ADS) (Cited on page 53.)

Narayan, R., & Yi, I. (1995b). *Advection-dominated Accretion: Underfed Black Holes and Neutron Stars*, ApJ 452, 710–735 (ADS) (Cited on pages 63 and 64.)

Nowak, M., & Lehr, D. (1998). *Stable oscillations of black hole accretion discs*, Theory of Black Hole Accretion Disks 233 (ADS) (Cited on pages 44 and 95.)

Nowak, M. A., Vaughan, B. A., Wilms, J., Dove, J. B., & Begelman, M. C. (1999). *Rossi X-Ray Timing Explorer Observation of Cygnus X-1. II. Timing Analysis*, ApJ 510, 874–891 (ADS) (Cited on page 17.)

Okada, R., Fukue, J., & Matsumoto, R. (1989). *A model of astrophysical tori with magnetic fields*, PASJ 41, 133–140 (ADS) (Cited on page 84.)

Okazaki, A. T., Kato, S., & Fukue, J. (1987). *Global trapped oscillations of relativistic accretion disks*, PASJ 39, 457–473 (ADS) (Cited on page 95.)

Orosz, J. A., et al. (2002). *Dynamical Evidence for a Black Hole in the Microquasar XTE J1550-564*, ApJ 568, 845–861 (ADS) (Cited on page 51.)

Orosz, J. A., McClintock, J. E., Remillard, R. A., & Corbel, S. (2004). *Orbital Parameters for the Black Hole Binary XTE J1650-500*, ApJ 616, 376–382 (ADS) (Cited on page 43.)

Paczyński, B. (1987). *Possible relation between the X-ray QPO phenomenon and general relativity*, Nature 327, 303 (ADS) (Cited on page 58.)

Paczyński, B., & Wiita, P. J. (1980). *Thick accretion disks and supercritical luminosities*, A&A 88, 23–31 (ADS) (Cited on pages 84, 85 and 88.)

Papaloizou, J. C. B., & Pringle, J. E. (1984). *The dynamical stability of differentially rotating discs with constant specific angular momentum*, MNRAS 208, 721–750 (ADS) (Cited on pages 54 and 61.)

Papaloizou, J. C. B., & Pringle, J. E. (1985). *The dynamical stability of differentially rotating discs. II*, MNRAS 213, 799–820 (ADS) (Cited on page 54.)

Pecháček, T., Dovčiak, M., Karas, V., Matt, G. (2005). *The relativistic shift of narrow spectral features from black-hole accretion discs.*, accepted for publication in A&A arXiv:astro–ph/0507196 (Cited on page 72.)

Press, W.H., Flannery, B.P., Teukolsky, S.A., Vetterling, W.T. (1989). *Numerical Recipes in C: The Art of Scientific Computing*, 2nd edition, 1992, Cambridge Univ. Press (Cited on page 66.)

Psaltis, D., et al. (1998). *The Beat-Frequency Interpretation of Kilohertz Quasi-periodic Oscillations in Neutron Star Low-Mass X-Ray Binaries*, ApJ 501, L95–L99 (ADS) (Cited on pages 24 and 25.)

Rauch, K. P., & Blandford, R. D. (1994). *Optical caustics in a kerr spacetime and the origin of rapid X-ray variability in active galactic nuclei*, ApJ 421, 46–68 (ADS) (Cited on page 98.)

Remillard, R. A. (2005). *X-ray States of Black Hole Binaries in Outburst*, AIP Conf. Proc. 797: Interacting Binaries: Accretion, Evolution, and Outcomes 797, 231–240 (ADS) (Cited on page 18.)

Remillard, R. A., Muno, M. P., McClintock, J. E., & Orosz, J. A. (2002). *Evidence for Harmonic Relationships in the High-Frequency Quasi-periodic Oscillations of XTE J1550-564 and GRO J1655-40*, ApJ 580, 1030–1042 (ADS) (Cited on page 20.)

Rezzolla, L., Yoshida, S., Maccarone, T. J., & Zanotti, O. (2003). *A new simple model for high-frequency quasi-periodic oscillations in black hole candidates*, MNRAS 344, L37–L41 (ADS) (Cited on page 69.)

Schnittman, J. D., & Bertschinger, E. (2004). *The Harmonic Structure of High-Frequency Quasi-periodic Oscillations in Accreting Black Holes*, ApJ 606, 1098–1111 (ADS) (Cited on page 69.)

Seguin, F. H. (1975). *The stability of nonuniform rotation in relativistic stars*, ApJ 197, 745–765 (ADS) (Cited on page 59.)

Shafee, R., McClintock, J. E., Narayan, R., Davis, S. W., Li, L.-X., & Remillard, R. A. (2005). *Estimating the Spin of Stellar-Mass Black Holes via Spectral Fitting of the X-ray Continuum*, accepted by ApJ, arXiv:astro–ph/0508302 (ADS) (Cited on page 47.)

Shibazaki, N., & Lamb, F. K. (1987). *Power spectra of quasi-periodic oscillations in luminous X-ray stars*, ApJ 318, 767–785 (ADS) (Cited on page 41.)

Stella, L., & Vietri, M. (1998). *Lense-Thirring Precession and Quasi-periodic Oscillations in Low-Mass X-Ray Binaries*, ApJ 492, L59–L62 (ADS) (Cited on page 24.)

Stella, L., & Vietri, M. (1999). *kHz Quasiperiodic Oscillations in Low-Mass X-Ray Binaries as Probes of General Relativity in the Strong-Field Regime*, Physical Review Letters 82, 17–20 (ADS) (Cited on pages 24 and 69.)

Stella, L., Vietri, M., & Morsink, S. M. (1999). *Correlations in the Quasi-periodic Oscillation Frequencies of Low-Mass X-Ray Binaries and the Relativistic Precession Model*, ApJ 524, L63–L66 (ADS) (Cited on page 24.)

Stepney, S., & Guilbert, P. W. (1983). *Numerical FITS to important rates in high temperature astrophysical plasmas*, MNRAS 204, 1269–1277 (ADS) (Cited on page 63.)

Strohmayer, T. E. (2001). *Discovery of a 450 HZ Quasi-periodic Oscillation from the Microquasar GRO J1655-40 with the Rossi X-Ray Timing Explorer*, ApJ 552, L49–L53 (ADS) (Cited on page 97.)

Strohmayer, T., Zhang, W., Smale, A., Day, C., Swank, J., Titarchuk, L., & Lee, U. (1996a). *U 1728-34*, IAU Circ. 6387, 2 (ADS) (Cited on page 24.)

Strohmayer, T. E., Zhang, W., & Swank, J. H. (1997). *363 HZ Oscillations during the Rising Phase of Bursts from 4U 1728-34: Evidence for Rotational Modulation*, ApJ 487, L77 (ADS) (Cited on pages 17 and 24.)

Strohmayer, T., Zhang, W., & Swank, J. (1996b). *U 1728-34*, IAU Circ. 6320, 1 (ADS) (Cited on page 24.)

Strohmayer, T. E., Zhang, W., Swank, J. H., Smale, A., Titarchuk, L., Day, C., & Lee, U. (1996c). *Millisecond X-Ray Variability from an Accreting Neutron Star System*, ApJ 469, L9 (ADS) (Cited on page 21.)

Swank, J. (2004). *Quasi-Periodic Oscillations from Low-mass X-Ray Binaries with Neutron Stars*, AIP Conf. Proc. 714: X-ray Timing 2003: Rossi and Beyond 714, 357–364 (ADS) (Cited on page 16.)

Tondl, A., Ruijgrok, T., Verhulst, F., & Nabergoj, R. (2000). *Autoparametric Resonance in Mechanical Systems*, pp. 206. ISBN 0521650798. Cambridge University Press (ADS) (Cited on page 44.)

Tooper, R. F. (1965). *Adiabatic Fluid Spheres in General Relativity.*, ApJ 142, 1541–1562 (ADS) (Cited on page 59.)

Török, G. (2005a). *A possible 3:2 orbital epicyclic resonance in QPO frequencies of Sgr A**, A&A 440, 1–4 (ADS) (Cited on page 20.)

Török, G. (2005b). *QPOs in microquasars and Sgr A* measuring the black hole spin*, Astronomische Nachrichten 326, 856–860 (ADS) (Cited on page 46.)

Török, G., Abramowicz, M. A., Kluźniak, W., & Stuchlík, Z. (2005). *The orbital resonance model for twin peak kHz quasi periodic oscillations in microquasars*, A&A 436, 1–8 (ADS) (Cited on pages 46 and 47.)

Ulrich, M.-H., Maraschi, L., & Urry, C. M. (1997). *Variability of Active Galactic Nuclei*, ARA&A 35, 445–502 (ADS) (Cited on page 97.)

van der Klis, M. (1997a). *Kilohertz Quasi-Periodic Oscillations in Low-Mass X-Ray Binaries*, ASSL Vol. 218: Astronomical Time Series 121 (ADS) (Cited on pages 16 and 97.)

van der Klis, M. (1997b). *Quantifying Rapid Variability in Accreting Compact Objects*, Statistical Challenges in Modern Astronomy II 321, arXiv:astro–ph/9704273 (ADS) (Cited on page 103.)

van der Klis, M. (2000). *Millisecond Oscillations in X-Ray Binaries*, Annual Reviews of Astronomy and Astrophysics 38, 717–760 arXiv:astro–ph/0001167 (Cited on pages 16, 27, 38 and 97.)

van der Klis, M. (2001). *A Possible Explanation for the "Parallel Tracks" Phenomenon in Low-Mass X-Ray Binaries*, ApJ 561, 943–949 (ADS) (Cited on page 16.)

van der Klis, M. (2005). *A review of rapid X-ray variability in X-ray binaries*, Compact Stellar X-ray Sources, eds. W.H.G. Lewin and M. van der Klis, Cambridge University Press arXiv:astro–ph/0410551 (Cited on pages 15, 16 and 17.)

van der Klis, M., & Jansen, F. A. (1985). *Transient quasi-periodic oscillations in the X-ray flux of Cygnus X-3*, Nature 313, 768–771 (ADS) (Cited on page 15.)

van der Klis, M., Jansen, F., van Paradijs, J., Lewin, W. H. G., van den Heuvel, E. P. J., Trumper, J. E., & Szatjno, M. (1985). *Intensity-dependent quasi-periodic oscillations in the X-ray flux of GX5 - 1*, Nature 316, 225–230 (ADS) (Cited on page 15.)

van der Klis, M., Swank, J., Zhang, W., Jahoda, K., Morgan, E., Lewin, W., Vaughan, B., & van Paradijs, J. (1996). *Scorpius X-1*, IAU Circ. 6319, 1 (ADS) (Cited on page 21.)

van der Klis, M., Wijnands, R. A. D., Horne, K., & Chen, W. (1997). *Kilohertz Quasi-Periodic Oscillation Peak Separation Is Not Constant in Scorpius X-1*, ApJ 481, L97 (ADS) (Cited on pages 24, 27 and 38.)

van Straaten, S., Ford, E. C., van der Klis, M., Méndez, M., & Kaaret, P. (2000). *Relations between Timing Features and Colors in the X-Ray Binary 4U 0614+09*, ApJ 540, 1049–1061 (ADS) (Cited on pages 27 and 38.)

van Straaten, S., van der Klis, M., di Salvo, T., & Belloni, T. (2002). *A Multi-Lorentzian Timing Study of the Atoll Sources 4U 0614+09 and 4U 1728-34*, ApJ 568, 912–930 (ADS) (Cited on pages 27 and 38.)

van Straaten, S., van der Klis, M., & Méndez, M. (2003). *The Atoll Source States of 4U 1608-52*, ApJ 596, 1155–1176 (ADS) (Cited on pages 27 and 38.)

Vaughan, B. A., et al. (1997). *Discovery of Microsecond Time Lags in Kilohertz QPOs*, ApJ 483, L115–L118 (ADS) (Cited on page 17.)

Wagoner, R. V., Silbergleit, A. S., & Ortega-Rodríguez, M. (2001). *"Stable" Quasi-periodic Oscillations and Black Hole Properties from Diskoseismology*, ApJ 559, L25–L28 (ADS) (Cited on page 69.)

Wang, D.-X., Ye, Y.-C., Ma, R.-Y., & Gong, X.-L. (2005). *A Toy Model for 3:2 Ratio of kHz QPO Frequency in Black Hole X-ray Binaries*, Chinese Journal of Astronony and Astrophysics 5, 7–12 (ADS) (Cited on page 69.)

Wijnands, R., & van der Klis, M. (1998). *A millisecond pulsar in an X-ray binary system.*, Nature 394, 344–346 (ADS) (Cited on page 41.)

Woudt, P. A., & Warner, B. (2002). *Dwarf nova oscillations and quasi-periodic oscillations in cataclysmic variables - I. Observations of VW Hyi*, MNRAS 333, 411–422 (ADS) (Cited on page 97.)

Yu, W., van der Klis, M., & Jonker, P. G. (2001). *Dependence of Kilohertz Quasi-periodic Oscillation Properties on the Normal-Branch Oscillation Phase in Scorpius X-1*, ApJ 559, L29–L32 (ADS) (Cited on page 17.)

Zhang, W., Jahoda, K., Kelley, R. L., Strohmayer, T. E., Swank, J. H., & Zhang, S. N. (1998). *Millisecond Oscillations in the Persistent and Bursting Flux of Aquila X-1 during an Outburst*, ApJ 495, L9–L12 (ADS) (Cited on pages 16 and 17.)

Zhang, X., Zhang, S. N., Feng, Y., & Yao, Y. (2003). *Relativistic effects on the appearance of a clothed black hole*, ASSL Vol. 298: Stellar Astrophysics - A Tribute to Helmut A. Abt 275–280 (ADS) (Cited on page 73.)